NEW MIXING-LENGTH MODEL FOR NUMERICAL SOLUTION OF TURBULENT SUPERSONIC FLOWS

by

Ming Situ

Dissertation submitted to the Faculty of the
Virginia Polytechnic Institute and State University
in partial fulfillment of the requirements for the degree of
DOCTOR OF PHILOSOPHY
in
Aerospace Engineering

APPROVED:

Dr. Joseph A. Schetz, Chairman

Dr. James F. Marchman

Dr. Bernard Grossman

Dr. Antoni K. Jakubowski

Dr. Dana A. Walker

January, 1989

Blacksburg, Virginia

NEW MIXING-LENGTH MODEL FOR NUMERICAL SOLUTION OF TURBULENT SUPERSONIC FLOWS

by

Ming Situ

Dr. Joseph A. Schetz, Chairman

Aerospace Engineering

(ABSTRACT)

An attempt has been made to find a new mixing-length model which will account for the effects of compressibility on the turbulence. Through an analysis of the Reynolds-stress formula and following the ideas of Prandtl's original mixing-length hypothesis, the effort has essentially been directed to classes of compressible flow problems where there exist large changes of density and Mach number. The new mixing-length model which has been found here is a generalization to include gradients of Mach number, pressure and density; and the local parameters values, such as speed of sound, density, Mach number, ratio of specific heats and a new parameter S which is introduced in the new turbulent transport formula. The new parameter S acts like an effective turbulent Schmidt Number for mixtures of gases or a turbulent Prandtl Number for a homogeneous gas.

The new turbulent model and Prandtl's original model are both applied to six test cases including: tangential slot injection problems, the very complex cases of shock-wave/turbulent shear-layer and boundary-layer interactions, and high Mach number turbulent boundary layer flows over a flat plate. The effective numerical method of flux-splitting with Roe's scheme has been adopted in the present work. The results are all compared with experimental data. The predictions with the new mixing-length model are generally in good agreement with the measured data. The predictions with Prandtl's original model have some discrepancies, especially for heated injection and higher Mach number turbulent boundary layers. The inability of Prandtl's model to predict the spreading rate of the free shear layer in slot injection into supersonic flows and higher Mach number turbulent boundary layer flows is due to the occurrence of large density changes which are not accounted for in the original Prandtl model. The new mixing-length model obtained here is the first to explicitly include these effects, and the results obtained show that these effects are important.

Acknowledgements

The author would like to thank Dr. J.A. Schetz for his guidance, advice and encouragement during this study. Without his support, it would have been difficult to complete the current work.

The author wishes to very specially thank Dr. J.F. Marchman, Dr. B. Grossman, Dr. A.K. Jakubowski and Dr. D.A. Walker for serving on the Advisory Committee.

He also wishes to thank Dr. H.E. Gilreath of APL for supplying his experimental results, to thank Dr. R.W. Walters for supplying his computer code, and to thank Mr. R.L. Campbell and Mr. B.R. Smith for supplying the experimental data of their slot injection experiments.

Very special thanks go to Dr. R.A. Teekell, Dean of the Graduate School, for encouraging me to complete this study. Finally, he wishes to thank his many friends at Virginia Tech.

List of Contents

I. INTRODUCTION 1

1.1 General 1

1.2 Present Status of Research 2

1.3 Objectives of the Present Work 10

II. DERIVATION OF NEW TURBULENCE MODELING 12

2.1 Background 12

2.2 Derivation of the New Turbulent Model 19

2.3 The New Number **S** 25

2.4 Mixing Length 27

2.5 Observations 28

III. COMPUTATIONAL FORMULATION 30

3.1 Overview 30

3.2 Governing Equations 32

3.3 Nondimensionalization and Transformation 34
3.3.1 Nondimensionalization 34
3.3.2 Vector Form of the Equations 37
3.3.3 Generalized Transformation 39
3.4 Numerical Method 42
3.4.1 Flux Difference Splitting 42
3.4.2 Algorithm 47
3.5 Numerical Domain and Boundary Conditions 49
3.5.1 Domain and Mesh Grid 49
3.5.2 Boundary Conditions 50

IV. TEST PROBLEMS, RESULTS AND DISCUSSION 52
4.1 Test Problems 52
4.2 Results and Discussion 55
4.2.1 Supersonic Injection into Supersonic Flow at $M_1 = 2.85$ 55
4.2.2 Sonic Injection into Supersonic Flow at $M_1 = 2.85$ 57
4.2.3 Supersonic Injection into Supersonic Flow at $M_1 = 3.0$ 58
4.2.4 Heated Supersonic Injection into Flow of $M_1 = 3.0$ 61
4.2.5 Shock-Wave/Turbulent Shear-Layer and Boundary-Layer Interaction 63
4.2.6 Hypersonic Turbulent Boundary Layer Flow over a Flat Plate 65

V. CONCLUDING REMARKS 68

REFERENCES 71

FIGURES 78

VITA 139

List of Illustrations

Figure 1. Schematic of slot injection in primary supersonic flow..... 79

Figure 2. (a) Typical computational grids used for slot injection flows and (b) typical computational grids used for turbulent boundary layer flows over a flat plate with a leading edge..... 80

Figure 3. Density profile at x/a = 4.00, for the case of $M_1 = 2.85$, $M_2 = 2.0$ (measured data from Ref. [77]). 81

Figure 4. Density profile at x/a = 6.00, for the case of $M_1 = 2.85$, $M_2 = 2.0$ (measured data from Ref. [77]). 82

Figure 5. Density profile at x/a = 9.25, for the case of $M_1 = 2.85$, $M_2 = 2.0$ (measured data from Ref. [77]). 83

Figure 6. Mach number profile at x/a = 4.00, for $M_1 = 2.85$, $M_2 = 2.0$. 84

Figure 7. Mach number profile at x/a = 6.00, for $M_1 = 2.85$, $M_2 = 2.0$. 85

Figure 8. Mach number profile at x/a = 9.25, for $M_1 = 2.85$, $M_2 = 2.0$. 86

Figure 9. Velocity profile at x/a = 4.00, for $M_1 = 2.85$, $M_2 = 2.0$. 87

Figure 10. Velocity profile at x/a = 6.00, for $M_1 = 2.85$, $M_2 = 2.0$..... 88

Figure 11. Velocity profile at x/a = 9.25, for $M_1 = 2.85$, $M_2 = 2.0$..... 89

Figure 12. (a) Experimental Spark-Schlieren from Ref. [77], (b) numerical density contour of Prandtl's model, and (c) numerical density contour of the new model for $M_1 = 2.85$, $M_2 = 2.0$..... 90

Figure 13. Wall presure distribution for slot injection, $M_1 = 2.85$, $M_2 = 2.0$ (measured data from Ref. [77]). 91

Figure 14. Density profile at x/a = 3.30, for the case of $M_1 = 2.85$, $M_2 = 1.0$ (measured data from Ref. [77]). 92

Figure 15. Density profile at x/a = 5.00, for the case of $M_1 = 2.85$, $M_2 = 1.0$ (measured data from Ref. [77]). 93

Figure 16. Density profile at x/a = 6.70, for the case of $M_1 = 2.85$, $M_2 = 1.0$ (measured data from Ref. [77]). 94

Figure 17. Mach number profile at x/a = 3.30, for $M_1 = 2.85$, $M_2 = 1.0$..... 95

Figure 18. Mach number profile at x/a = 5.00, for $M_1 = 2.85$, $M_2 = 1.0$..... 96

Figure 19. Mach number profile at x/a = 6.70, for $M_1 = 2.85$, $M_2 = 1.0$..... 97

Figure 20. Velocity profile at x/a = 3.30, for $M_1 = 2.85$, $M_2 = 1.0$..... 98

Figure 21. Velocity profile at x/a = 5.00, for $M_1 = 2.85$, $M_2 = 1.0$..... 99

Figure 22. Velocity profile at x/a = 6.70, for $M_1 = 2.85$, $M_2 = 1.0$..... 100

Figure 23. Mach number profile at x/a = 0.25, for $M_1 = 3.0$, $M_2 = 1.7$ (measured data from Ref. [10]). 101

Figure 24. Velocity profile at x/a = 0.25, for the case of $M_1 = 3.0$, $M_2 = 1.7$ (measured data from Ref. [10]). 102

Figure 25. Density profile at x/a = 0.25, for the case of $M_1 = 3.0$, $M_2 = 1.7$ (measured data from Ref. [10]). 103

Figure 26. Mach number profile at x/a = 4.00, for $M_1 = 3.0$, $M_2 = 1.7$ (measured data from Ref. [10]). 104

Figure 27. Velocity profile at x/a = 4.00, for the case of $M_1 = 3.0$, $M_2 = 1.7$ (measured data from Ref. [10]). 105

Figure 28. Density profile at x/a = 4.00, for the case of $M_1 = 3.0$, $M_2 = 1.7$ (measured data from Ref. [10]). 106

Figure 29. Mach number profile at x/a = 10.0, for $M_1 = 3.0$, $M_2 = 1.7$ (measured data from Ref. [10]). 107

Figure 30. Velocity profile at x/a = 10.0, for the case of $M_1 = 3.0$, $M_2 = 1.7$ (measured data from Ref. [10]). 108

Figure 31. Density profile at x/a = 10.0, for the case of $M_1 = 3.0$, $M_2 = 1.7$ (measured data from Ref. [10]). 109

Figure 32. Mach number profile at x/a = 20.0, for $M_1 = 3.0$, $M_2 = 1.7$ (measured data from Ref. [10]). 110

Figure 33. Velocity profile at x/a = 20.0, for the case of $M_1 = 3.0$, $M_2 = 1.7$ (measured data from Ref. [10]). 111

Figure 34. Density profile at x/a = 20.0, for the case of $M_1 = 3.0$, $M_2 = 1.7$ (measured data from Ref. [10]). 112

Figure 35. (a)Experimental Spark-Schlieren from Ref.[10] and (b)numerical density contour of the new model for $M_1 = 3.0$, $M_2 = 1.7$ 113

Figure 36. Mach number profile at x/a = 0.25, for heated injection flow (measured data from Ref. [78]). 114

Figure 37. Velocity profile at x/a = 0.25, for heated injection flow (measured data from Ref. [78]). 115

Figure 38. Density profile at x/a = 0.25, for heated injection flow (measured data from Ref. [78]). 116

Figure 39. Mach number profile at x/a = 4.0, for heated injection flow (measured data from Ref. [78]). 117

Figure 40. Velocity profile at x/a = 4.0, for heated injection flow (measured data from Ref. [78]). 118

Figure 41. Density profile at x/a = 4.0, for heated injection flow (measured data from Ref. [78]). 119

Figure 42. Mach number profile at x/a = 10, for heated injection flow (measured data from Ref. [78]). 120

Figure 43. Velocity profile at x/a = 10, for heated injection flow (measured data from Ref. [78]). 121

Figure 44. Density profile at x/a = 10, for heated injection flow (measured data from Ref. [78]). 122

Figure 45. Mach number profile at x/a = 20, for heated injection flow (measured data from Ref. [78]). 123

Figure 46. Velocity profile at x/a = 20, for heated injection flow (measured data from Ref. [78]). 124

Figure 47. Density profile at x/a = 20, for heated injection flow (measured data from Ref. [78]). 125

Figure 48. (a)Experimental Spark-Schlieren from Ref.[10] and (b)numerical density contour for shock-wave/turbulent shear layer and boundary layer interaction of the new model..... 126

Figure 49. Wall pressure distribution for shock-wave/turbulent shear layer and boundary layer interaction (measured data from Ref. [10])..... 127

Figure 50. Mach number profile at x/a = 20 for shock-wave/turbulent shear layer and boundary layer interaction (measured data from Ref. [10])..... 128

Figure 51. Velocity profile at x/a = 20 for shock-wave/turbulent shear layer and boundary layer interaction (measured data from Ref. [10])..... 129

Figure 52. Density profile at x/a = 20 for shock-wave/turbulent shear layer and boundary layer interaction (measured data from Ref. [10])..... 130

Figure 53. Mach number profile at x/a = 20 for shock-wave/heated turbulent shear layer and boundary layer interaction (measured data from Ref. [78])..... 131

Figure 54. Velocity profile at x/a = 20 for shock-wave/heated turbulent shear layer and boundary layer interaction (measured data from Ref. [78])..... 132

Figure 55. Density profile at x/a = 20 for shock-wave/heated turbulent shear layer and boundary layer interaction (measured data from Ref. [78]) 133

Figure 56. Mach number profile in the turbulent boundary layer flow over a flat plate at x = 69.25 inches from the throat, M = 4.67 (measured data from Ref. [79]) 134

Figure 57. Velocity profile in the turbulent boundary layer flow over a flat plate at x = 69.25 inches from the throat, M = 4.67 (measured data from Ref. [79]) 135

Figure 58. Density profile in the turbulent boundary layer flow over a flat plate at x = 69.25 inches from the throat, M = 4.67 (measured data from Ref. [79]) 136

Figure 59. Velocity profile in the turbulent boundary layer flow over a flat plate at x = 26 inches from the leading edge, $M_\infty = 6.55$ (measured data from Ref. [80,81]) 137

Figure 60. Velocity profile in the turbulent boundary layer flow over a flat plate at x = 35 inches from the leading edge, $M_\infty = 6.55$ (measured data from Ref. [80,81]) 138

List of Symbols

a .....speed of sound or slot height

A .....Jacobian matrix, ($\partial f/\partial Q$)

A^+.....damping coefficient $\simeq$ 26.0

$\overline{A}, \overline{B}$ .....coefficients in Gauss Seidel equation

$\overline{C}, \overline{D}$ .....coefficients in Gauss Seidel equation

b .....shear layer width

B.....Jacobian matrix, ($\partial g/\partial Q$)

c.....constant

c_1.....constant

c_2.....Sutherland's constant $\simeq$110.4°K

c_p.....specific heat at constant pressure

const......constant

D .....diffusivity

e.....internal energy per unit mass

$\overline{E}, \overline{F}$.....coefficients in Gauss Seidel equation

G.....matrix in viscous term

$\overline{H}, \overline{I}$.....coefficients in Gauss Seidel equation

f.....vector of conserved variables

f_v.....vector of conserved variables, viscous terms

g.....vector of conserved variables

h.....enthalpy per unit mass

I.....unit matrix

J.....index or Jacobian of a transformation matrix

K.....index or thermal conductivity

k.....Von Karman constant or turbulent energy

l.....length

l_m.....Prandtl mixing length

l_u.....velocity length scale

l_ρ.....density length scale

l_ω.....vorticity length scale

Le.....Lewis Number

L_{ref}.....reference length

M.....Mach number or matrix

M_c.....convective Mach number

p.....static pressure

Pr.....Prandtl number

q.....speed, ($=\sqrt{u^2+v^2}$ or $=\sqrt{u^2+w^2}$)

Q .....vector of conservative variables

R.....constant in state equation or correlation factor

Re_L.....Reynolds number at free stream

$R(Q)$ .....steady state residual

S.....New parameter

$\bar{S}$.....New parameter relative to vorticity

Sc .....Schmidt number

t.....time

T.....static temperature or matrix of eigenvectors

u, v, w .....velocity components in Cartesian coordinates

$\bar{u}\overline{\rho' v'}$ .....Reynolds stress component

$\bar{v}\overline{\rho' u'}$ .....Reynolds stress component

x.....streamwise coordinate in physical plane

y ..... transverse coordinate in physical plane

$y_{.95}, y_{.05}$.....value of y where $(u - u_2)/(u_1 - u_2) = 0.95, 0.05$, respectively

$\bar{\rho}\overline{u' v'}$ .....Reynolds stress component

$\overline{\rho' u' v'}$ .....Reynolds stress component

Greek symbols

α .....coefficient in turbulent model equation

γ .....ratio of specific heat for a perfect gas

δ .....boundary layer thickness or difference operator

δ_{ij} .....Kronecker delta function

Δ,∇ .....difference operators

ΔQ.....incremental change in Q between t^n and t^{n+1} time

Δf.....incremental change in Q between t^n and t^{n+1} time

Δg.....incremental change in Q between t^n and t^{n+1} time

ε.....turbulent energy dissipation or kinematic eddy viscosity

ε_m.....turbulent diffusivity for momentum

ε_M.....turbulent diffusivity for mass

ζ, η.....generalized coordinate

Λ .....diagonal matrix of eigenvalues

μ .....dynamic viscosity

ρ .....density

σ .....spreading parameter

σ_o.....spreading parameter, when $u_2/u_1 = 0$ condition

τ .....viscous stresses or laminar viscous stresses

τ' .....turbulent viscous stresses

ω .....vorticity

Subscripts

a .....denotes matrix A

b .....denotes matrix B

c.....characteristic

B.....bottom

eff.....effective value

f.....first region along shear layer

i.....spatial indice

j.....spatial indice or jet

k.....spatial indice

L.....laminar quantity or left of a cell interface

o.....stagnation value

R.....right of a cell interface

s.....second region along shear layer

t.....turbulent

T.....top

v.....viscous term

w.....wall

ζ, η.....coordinates indices

∞.....free stream condition

1.....primary flow

2.....tangential slot injection flow

Superscripts

n.....time level index

$-$.....time averaged mean value

Λ.....indicates a quantity in generalized coordinates

$'$.....fluctuation

$''$.....mass weighted fluctuation

$\sim$.....denotes a Roe-averaged or a mass-weighted variable

-1.....inverse

$*$.....dimensionless quantity

I. INTRODUCTION

1.1 General

There are at least two motivations for investigation of the tangential injection of a secondary stream into a primary flow by means of a wall slot. First is the large number of possible applications, which is biased toward the aerospace area. For example, injection of a low kinetic and/or thermal energy stream would serve as a means of reducing skin friction and heat transfer. On the other hand, the tangential injection of a high kinetic energy stream can be expected to prevent separation by supplying the boundary layer with sufficient energy to overcome unfavorable pressure gradients such as those on inlets of jet engines or on the "external blown flap." Recently, a proposal has been made to combine the advantages of this unique flow field with a fuel injection system for supersonic combustion in the hypersonic engine of an aerospace plane. The second general

reason for interest in this flowfield is more basic. Such flows are complex from a turbulence modeling point of view. The complexities arise from considering merging viscous layers and also the frequent occurrence of large transverse density variations, especially with foreign gas injection.

The slot injection flow is shown schematically in Fig. 1. It is usually a two-dimensional flow. The primary flow is supersonic in many applications; the injectant stream can be supersonic or subsonic. For purposes of analysis, the slot injection profile has been divided into two kinds of layers. One is the inner wall boundary layer; the other is the outer layer which has characteristics more like a free shear layer. When the flow develops along the streamwise direction, both the free shear layer and the wall boundary layer will merge together, which results in a complicated flow region from a turbulence modeling point of view. If an incident shock wave occurs on this region where the turbulent shear layer has touched on the turbulent boundary layer, very complicated turbulent flows due to shock-wave/turbulent shear-layer and/or boundary-layer interaction occur.

1.2 Present Status of Research

For a long time, there has been a lot of research work on free shear layer flows and on boundary layer flows. Relatively few of the investigations on slot injection are with supersonic free shear layer cases. To date, much of the research

conducted in this area has been experimental in Refs. [1-10]. On the other hand, the first enduring analysis of a wall jet flow was that by Glauert [11] in 1956.

Spalding and his associates have developed two methods for calculating wall jet development. The second of these, chronologically, is an extension of the work of Patankar and Spalding [12] on a boundary layer calculation method using a mixing length hypothesis and early finite difference techniques. It cannot treat pressure mismatch.

In Refs. [13,14], Bushnell and his group developed a method to calculate compressible turbulent boundary layers with tangential slot injection of homogeneous gas species. The boundary layer equations were adopted as the governing equations. The turbulent flux terms are modeled by means of eddy-diffusivity and mixing-length concepts. The magnitude and distribution of the mixing length across the boundary layer are determined from the computed characteristics of the free-mixing region between the injected jet and the initial boundary layer. Since the normal-momentum equation was neglected, the results may not apply when the static pressure at the slot exit differs from the static pressure of primary flow. Recently, Yoon and Schetz [15] applied the thin-layer Navier-Stokes equations to predict the flow field of slot injection in supersonic flows with laminar flow conditions.

As stated previously, if the lower wall in the slot injection case is far removed from the splitter plate, the upper layer is, typically, a free shear layer in

supersonic flow. Of course, the lower layer is the wall boundary layer. Past works on free shear layers are relevant to some features of the slot injection case, so we should mention them here.

To date, there are a lot of research works on free shear layers. First of all, one should talk about experiments, because most of the investigations of free shear layers have concentrated on the experiments. One can understand that it is real thing, since this is a formidable set of conditions with which to confront a calculation method. The aspects of experiments are included in the well-known types of classical free turbulent shear flows, such as, plane (or round) jet and plane (or round) wake.

Birch and Eggers [16] have compiled surveys of the literature in the first Symposia on Turbulent Shear Flow. They selected test cases for use in that conference to review the relevant data and to present the results in a convenient form. After that, the three Conferences on Turbulent Shear Flows in 1977,1979 and 1981 contain many articles on shear layers. Most of the papers Refs. [17-22] recognized that the spreading rate or spreading width of the layers increases as the velocity ratio u_2/u_1 decreases. If one uses the spreading parameter σ, which is inversely proportional to the spreading angle, σ_o/σ will drop when u_2/u_1 increases. The experimental values of σ for zero-velocity-ratio shear layers show that σ increases with increasing Mach Number from M = 1 to 2, and after M = 2, σ keeps constant [23,24]. A discrepancy in Ref. [25] is that it shows σ increases

until M = 5 ; but some data from NASA Langley present the same results as from Ref. [25].

The effect of the initial boundary layer on the downstream growth of the turbulent mixing layer between two streams has been studied experimentally [26]. It is pointed that if the initial boundary layer is turbulent, the mixing layer at first grows more slowly, then relaxes toward the growth rate of the untripped layer, the so-called second region. Reference [27] has reported that the first region is virtually independent of Reynolds Number; it is only dependent on the initial bounday layer thickness. That means it is a strong function of the initial disturbance level. The second region is much less sensitive to initial conditions.

Another important thing is the effect of density ratio on the spreading parameter σ. Most papers [28-30] assume that the density ratio will influence σ in homogeneous or heterogeneous shear flows. Reference [31] indicates that the effects of density ratio on the spreading rate may be due to buoyancy effects. But, Roshko [20,32] claimed that density differences in subsonic flows had a relatively small effect on the turbulent mixing rate and found that it is very much smaller than what is observed in the supersonic case. Thus, they [32] suggested that the spreading rates could be correlated with a compressibility effect parameter called the convective Mach number. The convective Mach number, M_c, is a parameter that decouples the effects of compressibility from those of density ratio and velocity ratio in the study of high speed free shear layers. For a given density and velocity ratio, the convective Mach number has been found to correlate the ratio

of compressible to incompressible shear layer growth rate. The development of the convective Mach number is based upon a frame of reference moving with the convected, large scale structure in a free shear layer. In a compressible vortex sheet stability analysis, M_c is a measure of the difference between the mean velocity and the convective velocity. So, it illustrates the effect of M_c on the stability of a vortex sheet.

A number of well-known approximate analytic solutions were developed for low-speed free shear layer flows. Prandtl [33] studied the smoothing of a velocity discontinuity and assumed similar velocity profiles. Schlichting [33] first examined the two-dimensional wake. Görtler [34] in 1942 derived the similarity analysis of free shear layer flows using the boundary layer equations and kinematic viscosity $\varepsilon = cb(u_1 - u_2)$. But, the original assumption of a constant mixing length across the mixing region has led to inaccurate predictions of the fluctuating components, according to Liepmann and Laufer [35], despite generally good agreement of the mean velocity profiles with experimental data.

In Ref. [36], the compressible free shear layer in a backstep region has been investigated numerically, and it was concluded that the constant in the mixing-length must have different values in the similar and nonsimilar regions. Reference [37] used the mixing-length model with the second derivative term to predict the development of the hypersonic turbulent wake produced by a wedge. The first attempt to systematically apply the mixing-length model to a significant range of free turbulent flows was Harsha's [38] and Schetz's [39] studies of eddy

viscosity models. At the same time, successful research works [13,14,40] at NASA Langley in the use of Prandtl's model were completed. On the basis of high-speed boundary layer experience, they indicated that the model should be given further consideration in free shear flows, and a so-called "rational" approach was suggested.

Because of the advent of high-speed computers, some complicated methods, such as turbulent kinetic energy and its variants, have been introduced to turbulent shear layer flows. Thus, one-equation turbulent models, two-equation turbulent models and so on, appear in the predictions of turbulent shear layer flows. Spalding's group at Imperial College [12,41-43] has used the TKE model and its variants, except mixing-length model to predict the turbulent flows. At the TKE level, the Prandtl energy method was used; Harsha [44] extended the Bradshaw TKE method approach to free shear flows. Reference [45] applied a two-equation turbulent model to calculate round diffusion jets with combustion. Schetz [9,46,47] has systematically recommended a number of different turbulent models for different cases.

As stated previously, there are many inconsistencies and unexplained differences among the various experimental investigations and calculations of the supersonic free shear layer. One of the main problems is that the turbulent mixing mechanism is not clear in supersonic free shear layer flows. So, there do arise in engineering applications problems with eddy viscosity approaches, in which the eddy viscosity methods are inadquate for the prediction of mean properties. If

one uses a TKE model or a K-ε model without corrections, the problems still exist.

The application of low-speed, turbulence model approaches with simple extensions to the calculation of high-speed turbulent boundary layers sometimes has proven quite successful, even up to high Mach numbers. However, for the shock-wave/turbulent boundary-layer interactions, computational results which are based on essentially low-speed turbulence models are generally unsatisfactory when applied to separated flow cases. Recently, Horstman [48], who has worked on the Reynolds-averaged Navier-Stokes equations with algebraic stress, two-equation, and eddy-viscosity models and their variants, indicated that no single model or modification correctly predicted the shock-wave/turbulent boundary-layer interactions, although the modifications improve the agreement with the experimental data. So, on this problem, there is still a lot of room for improvement.

Generally, a shock wave could be considered as a very steep pressure gradient. As pointed in Ref. [49], the low-speed information for such pressure gradients indicated that rapid distortion concepts hold, and in the limit of extremely sharp gradients, the Reynolds stress and turbulence intensities are "frozen," since there is insufficient residence time in the gradient for the turbulence to alter at all, let alone equilibrate. However, experimental information for shock-wave/boundary-layer interaction indicates significant amplifications of turbulence intensity across the shocked regions of shear layers, and for hypersonic

flows, the shock wave, which is very close to the body, is not thin. In fact, experiments indicate large amplifications of Reynolds stress and turbulence intensity across the shocked region of high-speed turbulent boundary layers. But, several mechanisms which exist to amplify turbulence intensity and Reynolds stress across a shock may be reasonably predicted by linearized perturbation of the Rankine-Hugoniot jump conditions. That basic idea needs to be modified for hypersonic flow conditions. Thus, it requires re-identifying some of the more important mechanisms that appear to influence the evolution of turbulence across shocked regions of shear layers and the respective degrees of the influences of such mechanisms. We hope that by focusing on a few of the more important turbulence amplifier-generator mechanisms, such as a sharp pressure gradient, a steep density gradient and a Mach number gradient across the shocked region in hypersonic flows, the effects can be clarified.

In the early 1900's, Ludwig Prandtl developed a new concept called the boundary layer. The fluid velocity within the boundary layer increases from zero at the wall to the freestream velocity at the edge of the boundary layer. Prandtl's concept was extremely important. Accordingly, a large amount of effort has been invested in experimental and analystical investigations of the behavior of such flows. The bulk of this research, however, has been concerned with the behavior of low-speed turbulent boundary layers, with relatively few of the investigations on the high-speed turbulent boundary layers. The first sound analysis of compressible turbulent boundary layer was that by Van Driest (1951) [50]. One of the interesting things shown by Maise and McDonald [51] from experimental

data on compressible boundary layers, that up to a Mach number of 5, the effect of compressibility on the mixing length is negligible. However, on the basis of high-speed boundary layer experience [40, 52] at NASA Langley, workers there have indicated that more rational models are needed.

1.3 Objectives of the Present Work

Because of the status of knowledge described above, the main thrust of current research will be concerned with the further analysis of Prandtl mixing-length theories. After introducing complete Reynolds stresses in Reynolds form of the time-averaged Navier-Stokes equations, we will show explicitly that the classical eddy viscosity using the mixing length concept is correct only for lower speed flows with constant density. It is not correct for high speed flows with strong variations of density, because the effect of a local gradient of density on the turbulence is not included.

Through our analysis, we will obtain a new mixing-length model of the eddy viscosity, which includes the effects of transverse gradients of Mach number, pressure and density on turbulent flows. Thus, it may help to explain some of the critical problems which have existed in turbulent free shear layer flows for a long time. Finally, we test the adequacy of the new model by calculating slot injection problems , shock-wave/turbulent shear-layer and boundary-layer interactions and

high Mach number turbulent boundary layers, using Reynolds forms of the thin-layer Navier-Stokes equations with flux-splitting by Roe's scheme, and comparing the predications with data.

The final aim of the current work is to provide a new modeling of the eddy viscosity described above for engineering applications of high-speed flows which involve more of the physics of turbulence than is contained in Prandtl's original mixing-length model.

II. DERIVATION OF NEW TURBULENCE MODEL

2.1 Backgroud

One of the main things in any high Reynolds Number, viscous flow calculation is turbulence modeling, especially in high-speed, compressible flows. Thus, discussion of turbulent modeling is addressed in detail first.

Turbulent flows contain a large range of length scales. Most of the prior fundamental work on turbulence modeling has been on the incompressible, Navier-Stokes equations. For many years, models developed on an *ad hoc* basis from the incompressible equations have been applied to compressible flows, frequently with success. At higher Mach numbers, existing turbulent models become increasingly inadequate.

The most common approach to the prediction of turbulent flows is based on Reynolds averaging. There are two types of averaging presently used, the classical Reynolds averaging and the mass-weighted averaging developed by Favre [53]. When the density fluctuations can be neglected, the two formulations become identical. For the classical Reynolds averaging, the time averaging of fluctuating quantities is zero, and the time averaging of the product of two fluctuating quantities is not equal to zero. For the mass-weighted averaging, the time averages of the fluctuating quantities are not equal to zero, unless the fluctuating density equals to zero, and the time averaging of the fluctuation multiplied by density is equal to zero. To complete the time-averaged procedure and neglect the viscosity fluctuations, the Reynolds viscous stresses for classical Reynolds averaging can be written in tensor form

$$\tau'_{ij} = -\overline{\rho u'_i u'_j} - \overline{u}_i\overline{\rho' u'_j} - \overline{u}_j\overline{\rho' u'_i} - \overline{\rho' u'_i u'_j}$$

with

$$\tau_{ij} = \mu_L\left[\left(\frac{\partial \overline{u}_i}{\partial x_j} + \frac{\partial \overline{u}_j}{\partial x_i}\right) - \frac{2}{3}\delta_{ij}\frac{\partial \overline{u}_k}{\partial x_k}\right]$$

where τ'_{ij} can be also called the turbulent viscous stress tensor, and τ_{ij} represents the laminar viscous stress tensor. For incompressible flow, the apparent turbulent viscous stress can be reduced to

$$\tau'_{ij} = -\overline{\rho u'_i u'_j}$$

The Reynolds viscous stresses for mass-weighted averaging can be written as

$$\tau'_{ij} = -\overline{\rho u''_i u''_j} + \mu_L[(\frac{\partial \overline{u''_i}}{\partial x_j} + \frac{\partial \overline{u''_j}}{\partial x_i}) - \frac{2}{3}\delta_{ij}\frac{\partial \overline{u''_k}}{\partial x_k}]$$

with

$$\tau_{ij} = \mu_L[(\frac{\partial \tilde{u}_i}{\partial x_j} + \frac{\partial \tilde{u}_j}{\partial x_i}) - \frac{2}{3}\delta_{ij}\frac{\partial \tilde{u}_k}{\partial x_k}]$$

where $u_i = \bar{u}_i + u'_i$ or $u_i = \tilde{u}_i + u''_i$

It can be seen from the above equations that, if the second term in the expression for τ'_{ij} involving the molecular viscosity is expected to be much smaller than the first term, the Reynolds stress formula in the mass-weighted Navier-Stokes equations is more compact,

$$\tau'_{ij} = -\overline{\rho u''_i u''_j}$$

It resembles the turbulent stresses of classical Reynolds averaging for incompressible flow.

Because the mean equations are not closed, the Reynolds stresses need to be modeled. The simplest models for the turbulent Reynolds stresses assume a Newtonian-like constitutive equation-the Boussineq eddy viscosity concept. The model represents turbulent transport in terms of gradients of the velocity field.

In higher-level models, partial differential equations for the turbulent kinetic energy, dissipation and/or turbulent Reynolds stresses are solved.

The eddy viscosity can be traced back to the 1877 paper of Boussinesq [54,55]. In that treatment, the turbulent shearing stresses might be related to the rate of mean strain. For the general Reynolds stress tensor, the Boussinesq assumption gives

$$\tau'_{ij} = \mu_t \left(\frac{\partial \bar{u}_i}{\partial x_j} + \frac{\partial \bar{u}_j}{\partial x_i} \right) - \frac{2}{3} \delta_{ij} \left(\mu_t \frac{\partial \bar{u}_k}{\partial x_k} + \rho \bar{k} \right)$$

where μ_t is the turbulent viscosity and $\bar{k}$ is the kinetic energy of turbulence. On the other hand, from analogy with kinetic theory one might expect that the turbulent viscosity can be modeled as

$$\mu_t = \rho v_c l_c$$

where v_c and l_c are characteristic velocity and length scales of the turbulence, respectively. So, attention is focused on viscosity μ_t. To define is one thing, but to evaluate is another.

The first model proposed for determining the value of μ_t was that of Prandtl [56], who supposed, guided no doubt by the kinetic theory of gases, that μ_t was proportional to the local density, to a length l_m, typical of the local turbulence structure, and to a typical velocity of the fluctuating motion. For the latter,

Prandtl took the product of l_m and $\left| \frac{\partial \bar{u}}{\partial y} \right|$. The product $l_m \left| \frac{\partial \bar{u}}{\partial y} \right|$ can be interpreted as characteristic velocity of turbulence, v_c . Then,

$$\mu_t = \rho \, l_m^2 \left| \frac{\partial u}{\partial y} \right| \tag{2.1}$$

The quantity l_m is the so-called mixing-length. The l_m is crudely similar to the mean free path between molecules, in that it is taken as some *effective interaction distance* , except that it is between eddies rather than molecules. Prandtl regarded it as determined primarily by the dimensions of the flow system; such as, it might be proportional to the distance from a near-by wall for a wall-bounded boundary layer or the width of a free shear layer.

For three-dimensional thin shear layers, Prandtl's formula is usually expressed as

$$\mu_t = \rho \, l_m^2 \left[\left(\frac{\partial u}{\partial y} \right)^2 + \left(\frac{\partial w}{\partial y} \right)^2 \right]^{1/2}$$

It is obvious that the concept of a mixing length has proved to be very important for engineers, because it describes more or less correctly the mechanisms underlying turbulent transport processes as well as because it has resulted in useful and practical semiempirical relations, at least for low-speed cases.

In the classical Prandtl's mixing length theory, l_m is usually proportional to the thickness of the free shear layer. The constant of proportionality is of the order

of $\frac{1}{10}$, as pointed out by Taylor [57]; but it can be different for different types of free turbulent flow [28]. In the early days, much use was made of the various mixing-length theories, such as Prandtl's model and the Prandtl-Taylor vorticity model. For the inner region of the wall boundary layer, Van Driest [50] tried to represent the physics of the damping of the turbulent eddies by the rigid wall, and pointed out that the mixing length l_m should be multiplied by a factor $[\,1 - \exp(-y^+/A^+)\,]$ which represents the decreasing of l_m near the wall. Patankar and Spalding [12], and Cebeci [58] simply used the Van Driest model with the density and viscosity evaluated at the local conditions as a function of y in the inner region for variable density flows. For the outer region, Maise and McDonald [51] have analyzed the available data to conclude that the low speed mixing-length model, $l_m = 0.09\delta$, can be carried over directly to variable-density cases for $M_\infty < 5$. Further, Cebeci and Smith [59] and Baldwin and Lomax [60] used different extensions of the Clauser formulation of the turbulent model for the outer region.

From the studies of compressible jet mixing [61], it has been shown that Prandtl's relationship is not valid when the fluid density varies through the mixing layer. As a result of those findings, several new formulations of the kinematic eddy viscosity or equivalent mixing parameters have been recommended [50,62]. In Ref. [63] it was pointed that the density in a viscosity formulation can be taken as a local value, then shear stresses can be used to eliminate the gradient of velocity. But those modifications are not rigorously based on the physics of the flow. Schetz [9,39,46] used the kinematic eddy viscosity model with a "mass flow

difference" to consider the effect of density on the turbulence for the turbulent jets and wakes. For wall boundary layers, he extended the Clauser model to variable-density flows using the *true* displacement thickness for variable-density flows. The predictions are in agreement with the measured data.

In many important turbulent flows, the density varies in space and time due to variations (a) in temperature and/or (b) in pressure and/or (c) in composition, or all of them. To describe those flows, the various predictive methods for turbulent flows with constant density must be extended or reformulated to take into account satisfactorily the effects of variable mean and fluctuating density. This is one of the central current problems in applied turbulence research. However, the physics of such flows must be better understood before their analytic description can make substantive progress. But, no matter which approach is used for describing equations and/or method of solution, the means for incorporating the effects of variable density are generally unclear. So, that problem was a so-called "critical" specific problem at the first Conference of Free Turbulent Shear Flows in 1972. Until recent years that problem has still not been overcome.

2.2 *Derivation of the New Turbulent Model*

One of the most important Reynolds stresses for thin viscous layers in a Cartesian coordinate system [33] is

$$\tau'_{xy} = -\overline{\rho}\overline{u'v'} - \overline{u}\overline{\rho'v'} - \overline{v}\overline{\rho'u'} - \overline{\rho'u'v'} \tag{2.2}$$

Let us introduce

$$\begin{aligned} R_{uv} &= \frac{\overline{u'v'}}{\sqrt{\overline{u'^2}}\sqrt{\overline{v'^2}}} \\ R_{\rho u} &= \frac{\overline{\rho'u'}}{\sqrt{\overline{\rho'^2}}\sqrt{\overline{u'^2}}} \\ R_{\rho v} &= \frac{\overline{\rho'v'}}{\sqrt{\overline{\rho'^2}}\sqrt{\overline{v'^2}}} \\ R_{\rho uv} &= \frac{\overline{\rho'u'v'}}{\sqrt{\overline{\rho'^2}}\sqrt{\overline{u'^2}}\sqrt{\overline{v'^2}}} \end{aligned} \tag{2.3}$$

where $R_{\rho u}$, $R_{\rho v}$, R_{uv} and $R_{\rho uv}$ are the correlation coefficients. Generally, one can write

$$\overline{u'v'} = -c_{uv}\sqrt{\overline{u'^2}}\sqrt{\overline{v'^2}}$$

where the numerical factor c_{uv} is unknown, but it is identical with the correlation coefficient R_{uv}. Assuming $u' \sim \partial\overline{u}/\partial y$, we can obtain following Prandtl

$$\sqrt{\overline{u'^2}} = l_u \frac{\partial \bar{u}}{\partial y}$$
$$\sqrt{\overline{v'^2}} = Const \bullet \sqrt{\overline{u'^2}} = Const \bullet l_u \frac{\partial \bar{u}}{\partial y} \tag{2.4}$$

From the above relations,

$$-\bar{\rho}\overline{u'v'} = \bar{\rho}\,(c_{uv} \bullet Const \bullet l_u^2)\, \frac{\partial \bar{u}}{\partial y}\, \frac{\partial \bar{u}}{\partial y}$$
$$= \bar{\rho}\, l_m^2\, \frac{\partial \bar{u}}{\partial y}\, \frac{\partial \bar{u}}{\partial y} \tag{2.5}$$

where the constant can now be included in the still unknown mixing length, l_m. This is Prandtl's mixing-length hypothesis.

We know $\sqrt{\overline{v'^2}} \simeq \sqrt{\overline{u'^2}}$, and due to the fact that in thin shear layers $\bar{u} >> \bar{v}$, from Eq. (2.2) one can say that $\bar{u}\overline{\rho'v'} >> \bar{v}\overline{\rho'u'}$. Thus, the term $\bar{v}\overline{\rho'u'}$ can be neglected in Eq. (2.2). Next, one can write

$$\overline{\rho'v'} = - c_{\rho v} \sqrt{\overline{\rho'^2}}\, \sqrt{\overline{v'^2}} \tag{2.6}$$

Assuming $\sqrt{\overline{v'^2}} = Const \bullet \sqrt{\overline{u'^2}} = Const \bullet l_u \frac{\partial \bar{u}}{\partial y}$ and $\sqrt{\overline{\rho'^2}} = l_\rho \frac{\partial \bar{\rho}}{\partial y}$, one obtains

$$\overline{\rho'v'} = - c_{\rho v} \sqrt{\overline{\rho'^2}}\, \sqrt{\overline{v'^2}}$$
$$= - c_{\rho v}\, l_\rho\, Const \bullet l_u \frac{\partial \bar{\rho}}{\partial y}\, \frac{\partial \bar{u}}{\partial y}$$
$$= - \frac{l_m^2}{S}\, \frac{\partial \bar{\rho}}{\partial y}\, \frac{\partial \bar{u}}{\partial y}$$

where $S = \frac{c_{uv} l_u}{c_{\rho v} l_\rho}$ and $1 > c_{uv}, c_{\rho u}, c_{\rho v}, c_{\rho uv} > 0$. Finally, we obtain

$$- \bar{u}\,\overline{\rho' v'} = \bar{u}\,\frac{l_m^2}{S}\,\frac{\partial \bar{\rho}}{\partial y}\,\frac{\partial \bar{u}}{\partial y} \tag{2.7}$$

It can be seen that the new number S is proportional to the ratio of the velocity-length scale l_u to the density-length scale l_ρ. Of course, l_u is different from Prandtl's mixing length l_m. Proceeding as before, one can write

$$- \overline{\rho' u' v'} = c_{\rho uv} \sqrt{\overline{\rho'^2}}\,\sqrt{\overline{u'^2}}\,\sqrt{\overline{v'^2}}$$

or

$$- \overline{\rho' u' v'} = c_{\rho uv}\, l_\rho\, l_u\, Const \bullet\, l_u\,\frac{\partial \bar{\rho}}{\partial y}\,\frac{\partial \bar{u}}{\partial y}\,\frac{\partial \bar{u}}{\partial y}$$

So,

$$- \overline{\rho' u' v'} = c_{\rho uv}\, l_u\,\frac{l_m^2}{S}\,\frac{\partial \bar{\rho}}{\partial y}\,\frac{\partial \bar{u}}{\partial y}\,\frac{\partial \bar{u}}{\partial y} \tag{2.8}$$

Comparing Eq. (2.8) with Eq. (2.7), we can assume that for higher speed flow

$$\bar{u} >> c_{\rho uv}\, l_u\,\frac{\partial \bar{u}}{\partial y}$$

because $c_{\rho uv}\, l_u$ is of smaller value. Thus, the term $-\overline{\rho' u' v'}$ in Eq. (2.2) can be neglected, since $-\bar{u}\overline{\rho' v'} >> -\overline{\rho' u' v'}$.

According to the above analysis, only two terms need be retained in Eq. (2.2), which was, tentatively, pointed by Schlichting [33] a long time ago, that is

$$\tau'_{xy} \simeq -\overline{\rho u'v'} - \overline{u\rho'v'} \tag{2.9}$$

Putting Eqs. (2.5) and (2.7) into Eq. (2.9), we obtain

$$\tau'_{xy} = l_m^2 \left(\overline{\rho}\,\frac{\partial \overline{u}}{\partial y} + \frac{\overline{u}}{S}\,\frac{\partial \overline{\rho}}{\partial y}\right)\frac{\partial \overline{u}}{\partial y} \tag{2.10}$$

For physical reasons, one should put the absolute value sign on the outside of both terms. So, finally, Eq. (2.10) can be written as

$$\tau'_{xy} = l_m^2 \left|\overline{\rho}\,\frac{\partial \overline{u}}{\partial y} + \frac{\overline{u}}{S}\,\frac{\partial \overline{\rho}}{\partial y}\right| \frac{\partial \overline{u}}{\partial y} \tag{2.11}$$

As pointed by Boussinesq [50], for thin layers, neglecting the terms involving $\overline{k}$ and $(\partial \overline{v}/\partial x)$, the turbulent viscosity μ_t can be defined by $\mu_t = \tau'_{xy}/(\partial \overline{u}/\partial y)$. So, μ_t is defined here as

$$\mu_t = l_m^2 \left|\overline{\rho}\,\frac{\partial \overline{u}}{\partial y} + \frac{\overline{u}}{S}\,\frac{\partial \overline{\rho}}{\partial y}\right| \tag{2.12}$$

From the point of view of the kinetic theory, now, the product $l_m\left|\frac{\partial \overline{u}}{\partial y} + \frac{\overline{u}}{\rho S}\frac{\partial \overline{\rho}}{\partial y}\right|$ in which the effect of the compressibility has been considered can be explained as the appropriate characteristic velocity of turbulence, v_c , instead of $l_m\left|\frac{\partial \overline{u}}{\partial y}\right|$ in the Prandtl's model.

For a perfect gas, the speed of sound is

$$\bar{a}^2 = \gamma \frac{\bar{p}}{\bar{\rho}}$$

Because of $\bar{u} >> \bar{v}$, the Mach number can be written as

$$M \simeq \frac{\bar{u}}{\bar{a}}$$

Using the above two equations, Eq. (2.12) can also be expressed in an alternative form:

$$\mu_t = l_m^2 \left| \bar{\rho}\bar{a} \frac{\partial M}{\partial y} + \frac{\gamma M}{2\bar{a}} \frac{\partial \bar{p}}{\partial y} + \alpha \bar{u} \frac{\partial \bar{\rho}}{\partial y} \right| \tag{2.13}$$

or

$$\mu_t = l_m^2 \left| \bar{\rho} \frac{\partial \bar{u}}{\partial y} - \bar{\rho} M \frac{\partial \bar{a}}{\partial y} + \frac{\gamma M}{2\bar{a}} \frac{\partial \bar{p}}{\partial y} + \alpha \bar{u} \frac{\partial \bar{\rho}}{\partial y} \right| \tag{2.14}$$

where $\alpha = (2 - S)/2S$. Taylor (1915) [55] made an important generalization for low speed cases, using vorticity, $\omega = (\frac{\partial \bar{u}}{\partial y} - \frac{\partial \bar{v}}{\partial x})$, instead of $\frac{\partial \bar{u}}{\partial y}$. So, one can obtain another form of the turbulent viscosity as follows:

$$\mu_t = l_\omega^2 \left| \bar{\rho}\omega + \frac{\bar{u}}{\bar{S}} \frac{\partial \bar{\rho}}{\partial y} \right| \tag{2.15}$$

or further

$$\mu_t = l_\omega^2 \left| \bar{\rho}\omega - \bar{\rho}M \frac{\partial \bar{a}}{\partial y} + \frac{\gamma M}{2\bar{a}} \frac{\partial \bar{p}}{\partial y} + \bar{\alpha}\bar{u} \frac{\partial \bar{\rho}}{\partial y} \right| \qquad (2.16)$$

where l_ω is vorticity mixing length, $\bar{\alpha}$ is a function of $\bar{S}$ and $\bar{S} = \bar{c}_1 (l_\omega / l_\rho)$, i.e., $\bar{S}$ is proportional to the ratio of the vorticity length scale to the density length scale. As stated in Ref. [57], l_ω may be equal to $l_m\sqrt{2}$ for low speed cases.

The present models, Eqs. (2.12) and (2.15) or alternative forms Eqs. (2.13) and (2.16), consider the effects of compressibity on turbulence. For low speed and constant density flows, Eqs. (2.12) and (2.15) reduce to the classical Prandtl formula. So, the present models are extensions of the Prandtl and Prandtl-Taylor models to compressible flows with a large difference of density.

One objection to all these models, new and old, should be pointed out. Using Eq. (2.1), the turbulent viscosity μ_t will vanish at a region of zero velocity gradient. Prandtl himself has already recognized that deviation and proposed a more extended expression which includes the second order partial derivative of u with respect to y, $\frac{\partial^2 \bar{u}}{\partial^2 y}$. It is more complicated, so that it has seldom been used. For the new model proposed here, if the velocity gradient can be zero, one of gradients of Mach number or pressure or density in supersonic or hypersonic flow will not usually be simultaneously zero. For such flows, the turbulent viscosity still will not vanish.

Furthermore, using $\bar{q}$ instead of $\bar{u}$ in Eq. (2.12), we suggest that the new model for three-dimensional thin layers can be written as

$$\mu_t = l_m^2 \left| \bar{\rho} \frac{\bar{u}}{\bar{q}} \frac{\partial \bar{u}}{\partial y} + \bar{\rho} \frac{\bar{w}}{\bar{q}} \frac{\partial \bar{w}}{\partial y} + \frac{\bar{q}}{S} \frac{\partial \bar{\rho}}{\partial y} \right|$$

or

$$\mu_t = l_m^2 \left| \overline{\rho a} \frac{\partial M}{\partial y} + \frac{\gamma M}{2\bar{a}} \frac{\partial \bar{p}}{\partial y} + \alpha \bar{q} \frac{\partial \bar{\rho}}{\partial y} \right|$$

where $\bar{q} = \sqrt{\bar{u}^2 + \bar{w}^2}$ and $M \simeq \frac{\bar{q}}{\bar{a}}$.

2.3 *The New Number S*

From the above statements, it is obvious that the physical meaning of the new number S is that it is proportional to the ratio of the velocity length scale to the density length scale. But, it is difficult to know what kind of value to assign to this S number.

According to gradient transport theory [64], we can write

$$\overline{\rho' v'} = - D_t \frac{\partial \bar{\rho}}{\partial y} \tag{2.17}$$

for a gas mixture. Introducing the turbulent Schmidt number Sc_t,

$$\overline{\rho} D_t = \frac{\mu_t}{Sc_t} \simeq l_m^2 \frac{\overline{\rho}}{Sc_t} \frac{\partial \overline{u}}{\partial y}$$

where we use, approximately, the classical Prandtl turbulent model formula. Thus, we can write

$$- \overline{u} \overline{\rho' v'} = \overline{u} D_t \frac{\partial \overline{\rho}}{\partial y} \simeq l_m^2 \frac{\overline{u}}{Sc_t} \frac{\partial \overline{\rho}}{\partial y} \frac{\partial \overline{u}}{\partial y} \tag{2.18}$$

Now, comparing equation (2.7) with equation (2.18), it can be seen that the number S is, approximately, close to the value of turbulent Schmidt number, but only for a gas mixture. The turbulent Schmidt number [64] is defined as the ratio of the turbulent diffusivity for momentum to the turbulent diffusivity describing the mass transfer process.

For a single species gas, we can not use the concept of a Schmidt number. But, we can make an assumption, via a "thought experiment." If the turbulent Lewis number is one, the formula of the energy equation for a multi-species gas will, approximately, reduce to the formula of the energy equation for a single species gas. So, one can consider that the single species case is, imaginatively, Lewis number equals to one. From this point of view, it can be said that the value of S is close to Pr_t for single species gas, since $L_{et} = Pr_t/Sc_t$. Of course, it is also possible to use experimental results to correct the value of S. But, it is important to keep in mind that S is proportional to the ratio of the velocity-length scale to the density-length scale.

2.4 *Mixing Length*

For wall-bounded turbulent boundary layers, the mixing length in the inner region is usually adopted as

$$l_m = k\,y\,[1 - \exp(y^+/A^+)] \tag{2.19}$$

where $y^+ = \rho\, u_\tau\, y / \mu$ and u_τ is the *friction velocity*. For the outer region of a wall boundary layer, the formula of $l_m = 0.09\delta$ can be used.

For turbulent free-shear layers, Taylor and Prandtl have suggested that the mixing length l_m is proportional to the thickness of the layer, i.e.,

$$l_m = c\,b \tag{2.20}$$

where c is constant, near to 0.1 [55]. For two dimensional free shear layer, we suggest that $c \simeq 0.115$.

The free shear layer width, b, represents the growth and spread of the free shear layer. Due to initial flow conditions, the definition of width for the analysis of free shear layers is given in Ref. [42]. For a monotonically increasing/decreasing velocity profile, the characteristic mixing layer, b, is defined as the distance between the points at which u equals $u_2 + 0.1(u_1 - u_2)$ and $u_2 + 0.9(u_1 - u_2)$. There are actually boundary layers on both sides of the splitter plate, so the velocity profile has a minimal value in the mixing layer. The characteristic width of the

shear layer is then defined as the distance between the points at which $u = u_2 + 0.1(u_{min.} - u_2)$ and $u = u_2 + 0.9(u_1 - u_2)$. Rudy and Bushnell [40] define $b = (scaling\ factor)\ (y_{0.95} - y_{0.05})$.

In most conditions, the width, b, of the Mach number profile of a shear layer is very close to the width, b, of the velocity profile of a shear layer. For incompressible flows, the width of the Mach number profile reduces to the width of velocity profile. If the velocities of the two flows are very close, such as heated injection flows in supersonic and hypersonic flows; using the width of the Mach number profile instead of the velocity profile is better.

2.5 Observations

a. The proposed new turbulent model should be more accurate than the classical Prandtl model, because we retain two terms from the Reynolds stress equation. However, Prandtl only retains one term from the Reynolds stress equation.

b. The Prandtl's model is based on the mixing-length hypothesis. The new turbulent model, completely satisfies the procedures of mixing-length theory.

c. For low speed and constant density flows, the new model, obviously, reduces to Prandtl's mixing-length model. Prandtl's mixing-length model is recognized a good turbulence model for such cases.

d. The present model is able to include the effects of large density changes on turbulence and shows that the gradients of Mach number, pressure and density will influence the turbulent viscosity, but Prandtl's model can not.

e. Using the gradient of Mach number instead of the gradient of velocity in the mixing-length turbulent model is better for hypersonic flow problems, because Mach number represents the character of compressibility.

III. COMPUTATIONAL FORMULATION

3.1 Overview

As stated previously, Bushnell [13,40] applied the boundary layer equations to describe the motion of tangential slot injection and free shear layers for turbulent flows using an implicit finite-difference method. Patankar and Spalding [12] in 1967 used simple boundary layer equations with an eddy viscosity turbulent model to solve slot injection in subsonic flows. The equations were to be solved by a marching integration procedure with an explicit method. Then, Rodi and Spalding [41,42] developed one equation and two equation turbulent models, and the governing differential equations were solved using a parabolic version of the TEACH code with explicit form. The SIMPLE procedure for the subsonic PNS equations can also be applied to the incompressible Navier-Stokes equations.

Reference [65] applied the implicit MacCormack method to solve two dimensional Navier-Stokes equations for laminar free shear layer flows.

Favre [53] developed a mass-averaged form of the Navier-Stokes equations for compressible flows and mixtures of gases. Reference [66] applied mass weighted averaging suggested by Favre to solve the spreading rate of adiabatic, high Mach number free turbulent shear layers with a mean turbulent energy closure method. The basic governing equations for mean flow, turbulent kinetic energy and auxiliary equations were solved by an implicit (Crank-Nicholsion) finite difference method.

Recently, more accurate and efficient algorithms have been developed. The upwind method [67] is a variation of the MacCormack method which uses backward (upwind) differences. Steger and Warming [68] develop the flux-vector splitting algorithm for time dependent flows. There are two schemes for determining the interface fluxes, which are based on the characteristic theory for hyperbolic systems of equations. The flux difference splitting developed by Roe [69,70] constructs the cell interface fluxes by solving local Riemann problems. Roe constructs a solution to the approximate linearized Riemann problem using the so-called Roe-average values. Another scheme is flux vector splitting where portions of the flux vector are upwind differenced according to the sign of the corresponding eigenvalues. Van Leer developed a flux-vector splitting [71] based upon Mach number, following Steger and Warming [72]. Grossman and Walters [73] applied an analysis of flux-split algorithms to real gases flows. Thomas and

Walters [74,75] applied upwind relaxation algorithms for the compressible Navier-Stokes equations.

For supersonic turbulent injection problems and shock-wave/turbulent shear-layer and boundary-layer interactions, the wave patterns produced by the system are very complex, and turbulent viscous and inviscid flow interactions are strong and complicated. So, Yoon and Schetz [15] applied the thin-layer Navier-Stokes equations with flux-splitting by Roe's scheme and Van Leer's scheme to predict the flow field of slot injection in supersonic flows under laminar flow conditions. Considering the above results, the current work will address to use flux-splitting methods with Roe's scheme to solve compressible thin-layer Reynolds-averaged Navier Stokes equations. A general, two-dimensional finite volume, flux split computer code called ANSERS, developed at Virginia Tech by R.W. Walters, was modified extensively to predict the turbulent supersonic flows.

3.2 Governing Equations

The thin-layer, Reynolds-averaged, Navier Stokes equations [76] are adopted here as the governing equations for free shear layer mixing with wall bounded , shock-wave/turbulent shear-layer and boundary-layer interaction, and high-speed turbulent boundary layer flows over a flat plate. In the thin-layer approximation,

the viscous terms containing derivatives in the direction parallel to the body surface are neglected in the unsteady Navier-Stokes equations, but all other terms in the momentum equations are retained. The advantages of retaining the terms which are normally neglected in boundary-layer theory is that flows which contain a large normal pressure gradient can be readily computed.

After making some approximations, the time-averaged Reynolds form of the mean thin-layer Navier-Stokes equations in Cartesian coordinates can be written as:

Conservation of Mass:

$$\frac{\partial \bar{\rho}}{\partial t} + \frac{\partial}{\partial x}(\bar{\rho}\bar{u}) + \frac{\partial}{\partial y}(\bar{\rho}\bar{v}) = 0 \tag{3.1}$$

Conservation of Momentum in x direction:

$$\frac{\partial}{\partial t}(\bar{\rho}\bar{u}) + \frac{\partial}{\partial x}(\bar{\rho}\bar{u}\bar{u}) + \frac{\partial}{\partial y}(\bar{\rho}\bar{u}\bar{v}) = -\frac{\partial \bar{p}}{\partial x} + \frac{\partial}{\partial y}(\tau_{xy} + \tau'_{xy}) \tag{3.2}$$

Conservation of Momentum in y direction:

$$\frac{\partial}{\partial t}(\bar{\rho}\bar{v}) + \frac{\partial}{\partial x}(\bar{\rho}\bar{u}\bar{v}) + \frac{\partial}{\partial y}(\bar{\rho}\bar{v}\bar{v}) = -\frac{\partial \bar{p}}{\partial y} + \frac{\partial}{\partial y}(\tau_{yy} + \tau'_{yy}) \tag{3.3}$$

Conservation of Energy:

$$\frac{\partial}{\partial t}(\overline{\rho}\overline{e}_o) + \frac{\partial}{\partial x}[(\overline{\rho}\overline{e}_o + \overline{p})\overline{u}] + \frac{\partial}{\partial y}[(\overline{\rho}\overline{e}_o + \overline{p})\overline{v}]$$
$$= \frac{\partial}{\partial y}[\overline{u}(\tau_{xy} + \tau'_{xy}) + \overline{v}(\tau_{yy} + \tau'_{yy}) + K_{eff}\frac{\partial \overline{T}}{\partial y}] \tag{3.4}$$

where τ'_{xy} and τ'_{yy} have been written in Ref. [76], and $K_{eff} = K_L + K_t$. The mean form of the equation of state is

$$\overline{p} = \overline{\rho} R \overline{T} \tag{3.5}$$

In order to close the system of Eqs. (3.1) to (3.5), a turbulent model equation must be included. The Prandtl mixing-length formulation, Eq. (2.1) and the new mixing-length formulation, Eq. (2.13), are both applied here.

3.3 Nondimensionalization and Transformation

3.3.1 Nondimensionalization

The governing fluid dynamic equations are most often used in nondimensional form. The advantage in doing this is that the characteristic parameters, *i.e.*, M, *Re*, *Pr* , *etc.*, can be varied independently. Also, by nondimensionalizing the equations, the flow variables are "normalized" [76], so that their values fall between certain prescribed limits such as 0 and 1.

If this nondimensionalizing procedure is applied to the Eqs. (3.1) to (3.5), the nondimensional equations are obtained as follows,

$$\frac{\partial \bar{\rho}^*}{\partial t^*} + \frac{\partial}{\partial x^*}(\bar{\rho}^* \bar{u}^*) + \frac{\partial}{\partial y^*}(\bar{\rho}^* \bar{v}^*) = 0 \tag{3.7}$$

$$\begin{aligned} &\frac{\partial}{\partial t^*}(\bar{\rho}^* \bar{u}^*) + \frac{\partial}{\partial x^*}(\bar{\rho}^* \bar{u}^* \bar{u}^*) + \frac{\partial}{\partial y^*}(\bar{\rho}^* \bar{u}^* \bar{v}^*) \\ &\quad = -\frac{\partial \bar{p}^*}{\partial x^*} + \frac{\partial}{\partial y^*}(\tau^*_{xy} + \tau'^*_{xy}) \end{aligned} \tag{3.8}$$

$$\begin{aligned} &\frac{\partial}{\partial t^*}(\bar{\rho}^* \bar{v}^*) + \frac{\partial}{\partial x^*}(\bar{\rho}^* \bar{u}^* \bar{v}^*) + \frac{\partial}{\partial y^*}(\bar{\rho}^* \bar{v}^* \bar{v}^*) \\ &\quad = -\frac{\partial \bar{p}^*}{\partial y^*} + \frac{\partial}{\partial y^*}(\tau^*_{yy} + \tau'^*_{yy}) \end{aligned} \tag{3.9}$$

$$\begin{aligned} &\frac{\partial}{\partial t^*}(\bar{\rho}^* \bar{e}^*_o) + \frac{\partial}{\partial x^*}[(\bar{\rho}^* \bar{e}^*_o + \bar{p}^*)\bar{u}^*] + \frac{\partial}{\partial y^*}[(\bar{\rho}^* \bar{e}^*_o + \bar{p}^*)\bar{v}^*] \\ &= \frac{\partial}{\partial y^*}\left[\bar{u}^*(\tau^*_{xy} + \tau'^*_{xy}) + \bar{v}^*(\tau^*_{yy} + \tau'^*_{yy}) + \left(\frac{\mu^*_{eff}}{(\gamma - 1)M^2_\infty Pr_t Re_L}\right)\frac{\partial \bar{T}^*}{\partial y^*}\right] \end{aligned} \tag{3.10}$$

$$\bar{p}^* = \frac{1}{\gamma M^2_\infty}\bar{\rho}^* \bar{T}^* \tag{3.11}$$

where

$$\tau^*_{xy} = \frac{\mu^*_L}{Re_L}\left(\frac{\partial \bar{u}^*}{\partial y^*} + \frac{\partial \bar{v}^*}{\partial x^*}\right)$$

$$\tau^*_{yy} = \frac{2}{3}\frac{\mu^*_L}{Re_L}\left(2\frac{\partial \bar{v}^*}{\partial y^*} - \frac{\partial \bar{u}^*}{\partial x^*}\right)$$

$$\tau'^*_{xy} = \frac{\mu^*_t}{Re_L}\left(\frac{\partial \bar{u}^*}{\partial y^*} + \frac{\partial \bar{v}^*}{\partial x^*}\right)$$

$$\tau'^*_{yy} = \frac{2}{3}\frac{\mu^*_t}{Re_L}\left(2\frac{\partial \bar{v}^*}{\partial y^*} - \frac{\partial \bar{u}^*}{\partial x^*}\right)$$

$$\mu^*_{eff} = \mu^*_L + \mu^*_t$$

The reference length L_{ref} in our solution is set as the maximum length in the streamwise direction for the computational domain. If the gas is assumed as a perfect gas, then

$$\bar{p}^* = \frac{\bar{p}}{\bar{\rho}_\infty \bar{u}^2_\infty} = (\gamma - 1)\bar{\rho}^* \bar{e}^*$$

$$\bar{T}^* = \frac{\gamma M^2_\infty \bar{p}^*}{\bar{\rho}^*}$$

The coefficient of laminar viscosity has been related to the thermodynamic variables. The Sutherland formula for nondimensional laminar viscosity is given by

$$\mu^*_L = \left(\frac{\bar{T}}{\bar{T}_\infty}\right)^{3/2}\left(\frac{\bar{T}_\infty + c_2}{\bar{T} + c_2}\right)$$

For turbulent viscosity, the nondimensional form of the new turbulent model is

$$\mu_t^* = l_m^{*2} \left| \bar{\rho}^* \bar{a}^* \frac{\partial M}{\partial y^*} + \frac{\gamma M}{2\bar{a}^*} \frac{\partial \bar{p}^*}{\partial y^*} + \alpha \bar{u}^* \frac{\partial \bar{\rho}^*}{\partial y^*} \right| Re_L \qquad (3.12)$$

The coefficient of the effective thermal conductivity , K_{eff} , is related to the effective viscosity, μ_{eff} , by using the effective Prandtl number, Pr_{eff} . For gases, the effective Prandtl number is, approximately, close to the turbulent Prandtl number Pr_t , because for the fully-turbulent conditions the laminar viscosity, μ_L , is much less than the turbulent viscosity, μ_t .

For convenience, after here, the asterisks (*) and bar (-) will be dropped from the nondimensional mean equations.

3.3.2 Vector Form of the Equations

Before applying a finite difference scheme to the governing fluid dynamic equations, it is often convenient to combine the equations into a compact vector form in Cartesian coordinates:

$$\frac{\partial Q}{\partial t} + \frac{\partial f}{\partial x} + \frac{\partial g}{\partial y} = \frac{\partial g_v}{\partial y} \qquad (3.13)$$

where Q, f, g and g_v are given by

$$Q = \begin{bmatrix} \rho \\ \rho u \\ \rho v \\ \rho e_o \end{bmatrix} \qquad f = \begin{bmatrix} \rho u \\ (\rho u^2 + p) \\ \rho uv \\ (\rho e_o + p)u \end{bmatrix} \qquad g = \begin{bmatrix} \rho v \\ \rho uv \\ (\rho v^2 + p) \\ (\rho e_o + p)v \end{bmatrix}$$

$$g_v = \begin{bmatrix} 0 \\ \tau_{xy} \\ \tau_{yy} \\ u\tau_{xy} + v\tau_{yy} + \dfrac{\mu_{eff}}{(\gamma - 1)M_\infty^2 Pr_t Re_L} \dfrac{\partial T}{\partial y} \end{bmatrix}$$

where

$$\tau_{xy} = \frac{\mu_{eff}}{Re_L} \left(\frac{\partial u}{\partial y} + \frac{\partial v}{\partial x} \right)$$

$$\tau_{yy} = \frac{2}{3} \frac{\mu_{eff}}{Re_L} \left(2 \frac{\partial v}{\partial y} - \frac{\partial u}{\partial x} \right)$$

$$\tau_{xx} = \frac{2}{3} \frac{\mu_{eff}}{Re_L} \left(2 \frac{\partial u}{\partial x} - \frac{\partial v}{\partial y} \right)$$

In fact, for the thin-layer approximation, the terms of partial derivatives with respect to x in τ_{xy} and τ_{yy} are again neglected.

3.3.3 Generalized Transformation

It is convenient and common practice to transform the thin layer Naviers-Stokes equations from physical coordinate (x, y) space to computational coordinate (ζ, η) space in which $\Delta\zeta = \Delta\eta = 1$. By applying the general transformation to the complete two-dimensional Navier-Stokes equations and dropping all viscous terms containing partial derivatives with respect to ζ, the resulting thin-layer equations in generalized coordinates and conservation form [75] may be written as

$$\frac{1}{J}\frac{\partial Q}{\partial t} + \frac{\partial \hat{f}}{\partial \zeta} + \frac{\partial \hat{g}}{\partial \eta} = \frac{\partial \hat{g}_v}{\partial \eta} \tag{3.14}$$

where

$$\hat{f} = \frac{1}{J}(\zeta_x f + \zeta_y g) \qquad \hat{g} = \frac{1}{J}(\eta_x f + \eta_y g)$$

$$\hat{g}_v = \frac{1}{J}(\eta_x f_v + \eta_y g_v) \qquad J = \frac{\partial(\zeta,\eta)}{\partial(x,y)}$$

$$f_v = \begin{bmatrix} 0 \\ \tau_{xx} \\ \tau_{xy} \\ u\tau_{xx} + v\tau_{xy} + \dfrac{\mu_{eff}}{(\gamma-1)M_\infty^2 Pr_t Re_L}\dfrac{\partial T}{\partial x} \end{bmatrix}$$

Also,

$$\hat{f} = \frac{1}{J}\begin{bmatrix} \rho U \\ \rho uU + \zeta_x p \\ \rho vU + \zeta_y p \\ (\rho e_o + p)U \end{bmatrix} = \frac{|\nabla\zeta|}{J}\begin{bmatrix} \rho\bar{u} \\ \rho u\bar{u} + \hat{\zeta}_x p \\ \rho v\bar{u} + \hat{\zeta}_y p \\ (\rho e_o + p)\bar{u} \end{bmatrix}$$

$$\hat{g} = \frac{1}{J}\begin{bmatrix} \rho V \\ \rho uV + \eta_x p \\ \rho vV + \eta_y p \\ (\rho e_o + p)V \end{bmatrix} = \frac{|\nabla\eta|}{J}\begin{bmatrix} \rho\bar{v} \\ \rho u\bar{v} + \hat{\eta}_x p \\ \rho v\bar{v} + \hat{\eta}_y p \\ (\rho e_o + p)\bar{v} \end{bmatrix}$$

$$\hat{g}_v = \frac{|\nabla\eta|^2}{J}\left(\frac{\mu_{eff}}{Re_L}\right)\begin{bmatrix} 0 \\ (\hat{t}_x)u_\eta + \frac{1}{3}\hat{\eta}_x\hat{\eta}_y v_\eta \\ (\hat{t}_y)v_\eta + \frac{1}{3}\hat{\eta}_x\hat{\eta}_y u_\eta \\ (\hat{t}_x)\frac{(u^2)_\eta}{2} + (\hat{t}_y)\frac{(v^2)_\eta}{2} + \frac{1}{3}\hat{\eta}_x\hat{\eta}_y(uv)_\eta + \frac{1}{(\gamma-1)M_\infty^2 Pr_t}\frac{\partial T}{\partial\eta} \end{bmatrix}$$

where

$$\hat{\zeta}_x = \frac{\zeta_x}{|\nabla\zeta|} \quad \hat{\zeta}_y = \frac{\zeta_y}{|\nabla\zeta|} \quad \hat{\eta}_x = \frac{\eta_x}{|\nabla\eta|} \quad \hat{\eta}_y = \frac{\eta_y}{|\nabla\eta|}$$

$$|\nabla\zeta| = \sqrt{(\zeta_x^2 + \zeta_y^2)} \qquad |\nabla\eta| = \sqrt{(\eta_x^2 + \eta_y^2)}$$

$$U = \zeta_x u + \zeta_y v \qquad V = \eta_x u + \eta_y v$$

$$\bar{u} = \hat{\zeta}_x u + \hat{\zeta}_y v \qquad \bar{v} = \hat{\eta}_x u + \hat{\eta}_y v$$

$$\hat{t}_x = 1 + \frac{1}{3}\hat{\eta}_x^2 \qquad \hat{t}_y = 1 + \frac{1}{3}\hat{\eta}_y^2$$

In the above, the terms of $\hat{\zeta}_x$ and $\hat{\zeta}_y$ are the direction cosines of the cell face normal to the ζ -direction and $\frac{|\nabla\zeta|}{J}$ is the directed length of the cell face. The viscous term $\hat{g}_v$ can be rewritten as

$$\hat{g}_v = \frac{|\nabla\eta|^2}{J}\left(\frac{\mu_{eff}}{Re_L}\right)\hat{G}$$

Viscous terms are approximated by central differencing as

$$\left(\frac{\partial\hat{g}_v}{\partial\eta}\right)_j = (\hat{g}_v)_{j+\frac{1}{2}} - (\hat{g}_v)_{j-\frac{1}{2}}$$

or

$$\left(\frac{\partial\hat{g}_v}{\partial\eta}\right)_j = \left[\frac{|\nabla\eta|^2}{J}\left(\frac{\mu_{eff}}{Re_L}\right)\right]_{j+\frac{1}{2}}(\hat{G}_{j+1} - \hat{G}_j) - \left[\frac{|\nabla\eta|^2}{J}\left(\frac{\mu_{eff}}{Re_L}\right)\right]_{j-\frac{1}{2}}(\hat{G}_j - \hat{G}_{j-1})$$

Here it should be pointed out that the μ_t of the new model or Prandtl's model in μ_{eff} has been adopted in the general Boussinesq shear stress forms. Of course, it is approximate. However, that approximation is permitted for the thin-layer equations, because the viscous terms of $\hat{g}_v$ in the thin-layer equations have only a component in the direction of η , and the gradient of v is assumed to be very much smaller than the gradient of u.

3.4 Numerical Methods

3.4.1 Flux Difference Splitting

Flux-split difference schemes are efficient numerical schemes for solving the Euler equations, the thin-layer and full Navier-Stokes equations. These methods identify the characteristic directions of signal propagation and utilize these directions in differencing the flux terms. In order to explain the basic idea of flux-split methods, it can be useful to consider the one-dimensional, compressible, inviscid flow in Cartesian coordinates:

$$\frac{\partial Q}{\partial t} + \frac{\partial f}{\partial x} = 0 \tag{3.15}$$

The semi-discrete, finite volume representation of the above equation is

$$(\frac{\partial Q}{\partial t})_i + \frac{f_{i+\frac{1}{2}} - f_{i-\frac{1}{2}}}{\Delta x} = 0 \tag{3.16}$$

If the interface flux can be determined, the solution can be advanced in time by explicit or implicit time integration algorithms. There are two schemes for determining the interface fluxes, *i.e.*, flux vector splitting and flux difference splitting. As stated before, Roe's flux difference splitting scheme was adopted here.

The basic idea of flux difference splitting is to construct the cell interface fluxes by solving an underlying set of local Riemann problems. Roe's scheme is based on an approximate Riemann problem. For the equation (3.15), the f is a linear function of Q, and that equation can be written as

$$\frac{\partial Q}{\partial t} + \tilde{A} \frac{\partial Q}{\partial x} = 0 \tag{3.17}$$

where $\tilde{A}$ is the so-called Roe-averaged matrix. Roe proposed the following criteria to select a local mean values of $\tilde{A}$, *i.e.*,

(a) $\tilde{A}(Q,Q) = \tilde{A}(Q)$

(b) $\tilde{A}(Q_L, Q_R)$ has a complete set of real eigenvalues and eigenvectors.

(c) $\tilde{A}(Q_L, Q_R)(Q_R - Q_L) = f(Q_R) - f(Q_L)$

and the main property is

$$\begin{aligned} \Delta f &= \tilde{A}\,\Delta Q \\ f_R - f_L &= \tilde{A}\,(Q_R - Q_L) \end{aligned} \tag{3.18}$$

Writing $\tilde{A}$ in the form

$$\tilde{A} = \tilde{T}\,\tilde{\Lambda}\,\tilde{T}^{-1}$$

thus,

$$f_R - f_L = \Delta f = \tilde{T}\,\tilde{\Lambda}\,\tilde{T}^{-1}\,\Delta Q$$

where $\tilde{T}$ are eigenvectors matrix of $\tilde{A}$, and $\tilde{\Lambda}$ is a diagonal matrix of eigenvalues of $\tilde{A}$. The term $\tilde{T}^{-1}\Delta Q$ represents the strengths of the wave interactions separating the two states.

The numerical flux at the cell interface is expressed as

$$f_{i+\frac{1}{2}} = \frac{1}{2}\left(f_R + f_L - |\tilde{A}|\,\Delta Q\right) \tag{3.19}$$

By application of Roe's scheme to a 2-D flow problem, the flux at a cell face oriented normal to the ζ-direction of generalized coordinates is given as

$$\hat{f}_{i+\frac{1}{2}} = \frac{1}{2}\left(\hat{f}_R + \hat{f}_L - \tilde{T}|\tilde{\Lambda}|\tilde{T}^{-1}\Delta Q\right) \tag{3.20}$$

where

$$\tilde{T} = \begin{bmatrix} 1 & 0 & 1 & 1 \\ \tilde{u} & \hat{\eta}_x & \tilde{u}+\tilde{a}\hat{\zeta}_x & \tilde{u}-\tilde{a}\hat{\zeta}_x \\ \tilde{v} & \hat{\eta}_y & \tilde{v}+\tilde{a}\hat{\zeta}_y & \tilde{v}-\tilde{a}\hat{\zeta}_y \\ \frac{1}{2}\tilde{q}^2 & \tilde{\bar{v}} & \tilde{h}_o+\tilde{a}\tilde{\bar{u}} & \tilde{h}_o-\tilde{a}\tilde{\bar{u}} \end{bmatrix}$$

$$\tilde{\Lambda} = \begin{bmatrix} \tilde{\Lambda}_1 & 0 & 0 & 0 \\ 0 & \tilde{\Lambda}_2 & 0 & 0 \\ 0 & 0 & \tilde{\Lambda}_3 & 0 \\ 0 & 0 & 0 & \tilde{\Lambda}_4 \end{bmatrix}$$

$$\tilde{\Lambda}_1 = \frac{|\nabla\zeta|}{J}\tilde{\bar{u}} = \tilde{\Lambda}_2 \qquad \tilde{\Lambda}_3 = \frac{|\nabla\zeta|}{J}(\tilde{\bar{u}} + \tilde{a}) \qquad \tilde{\Lambda}_4 = \frac{|\nabla\zeta|}{J}(\tilde{\bar{u}} - \tilde{a})$$

$$\tilde{\bar{u}} = \hat{\zeta}_x\tilde{u} + \hat{\zeta}_y\tilde{v}$$
$$\tilde{\bar{v}} = \hat{\eta}_x\tilde{u} + \hat{\eta}_y\tilde{v}$$

The $\tilde{T}^{-1}\Delta Q$ can be written as

$$\tilde{T}^{-1}\Delta Q = \begin{bmatrix} \Delta\rho - \dfrac{\Delta p}{\tilde{a}^2} \\ \tilde{\rho}\,\Delta\bar{v} \\ \dfrac{(\Delta p + \tilde{\rho}\tilde{a}\Delta\bar{u})}{2\tilde{a}^2} \\ \dfrac{(\Delta p - \tilde{\rho}\tilde{a}\Delta\bar{u})}{2\tilde{a}^2} \end{bmatrix}$$

where Roe's averaging values read as

$$\tilde{\rho} = \sqrt{\rho_L\rho_R}$$
$$\tilde{u} = \frac{u_L\sqrt{\rho_L} + u_R\sqrt{\rho_R}}{\sqrt{\rho_L}\sqrt{\rho_R}}$$
$$\tilde{v} = \frac{v_L\sqrt{\rho_L} + v_R\sqrt{\rho_R}}{\sqrt{\rho_L}\sqrt{\rho_R}}$$
$$\tilde{h}_o = \frac{h_{oL}\sqrt{\rho_L} + h_{oR}\sqrt{\rho_R}}{\sqrt{\rho_L}\sqrt{\rho_R}}$$
$$\tilde{a}^2 = (\gamma - 1)\left[\tilde{h}_o - \frac{1}{2}(\tilde{u}^2 + \tilde{v}^2)\right]$$

$\Delta\hat{f}$ can be rewritten as a computational useful form which are relative to eigenvalues.

$$\Delta\hat{f} = |\tilde{A}|\Delta Q = |\Delta\hat{f}_1| + |\Delta\hat{f}_2| + |\Delta\hat{f}_3| + |\Delta\hat{f}_4| \tag{3.21}$$

where

$$|\Delta\hat{f}_1| = |\tilde{\Lambda}_1|(\Delta\rho - \frac{\Delta p}{\tilde{a}^2})\begin{bmatrix} 1 \\ \tilde{u} \\ \tilde{v} \\ \frac{\tilde{q}^2}{2} \end{bmatrix}$$

$$|\Delta\hat{f}_2| = |\tilde{\Lambda}_2|\tilde{\rho}\begin{bmatrix} 0 \\ \hat{\eta}_x\Delta\bar{v} \\ \hat{\eta}_y\Delta\bar{v} \\ \tilde{\bar{v}}\Delta\bar{v} \end{bmatrix} = |\tilde{\Lambda}_1|\tilde{\rho}\begin{bmatrix} 0 \\ \Delta u - \hat{\zeta}_x\Delta\bar{u} \\ \Delta v - \hat{\zeta}_y\Delta\bar{u} \\ \Delta(\frac{q^2}{2}) - \tilde{\bar{u}}\Delta\bar{u} \end{bmatrix}$$

$$|\Delta\hat{f}_{3,4}| = |\tilde{\Lambda}_{3,4}|\frac{(\Delta p \pm \tilde{\rho}\tilde{a}\Delta\bar{u})}{\tilde{a}^2}\begin{bmatrix} 1 \\ \tilde{u} \pm \tilde{a}\hat{\zeta}_x \\ \tilde{v} \pm \tilde{a}\hat{\zeta}_y \\ \tilde{h}_o \pm \tilde{a}\tilde{\bar{u}} \end{bmatrix}$$

The flux-difference splitting in the η-direction is given by a similar method.

3.4.2 Algorithm

The unsteady, Reynolds-averaged compressible Navier-Stokes equations are a mixed set of hyperbolic-parabolic equations in time. So, it is better to use a time-dependent approach. The steady state solution is obtained by marching the solution in time until convergence is achieved. The algorithms are constructed, so that the steady-state solution is independent of the time step and as such, time accuracy is not of importance. Eq. (3.14) can be written in terms of the steady-state residual,

$$\frac{1}{J}\frac{\partial Q}{\partial t} - R(Q) = 0 \tag{3.22}$$

Using the Euler implicit time integration scheme, we have

$$\begin{aligned} \frac{1}{J}\frac{\partial Q}{\partial t} - R(Q^{n+1}) &= 0 \\ \frac{1}{J}\frac{\partial Q}{\partial t} - \Delta R &= R(Q^n) \end{aligned} \tag{3.23}$$

where $\Delta R = R(Q^{n+1}) - R(Q^n) = (\frac{\partial R}{\partial Q})^n \Delta Q$. Thus, the results in a linear system with operator notation is

$$(\frac{I}{J\Delta t} - \frac{\partial R}{\partial Q})\Delta Q = R(Q^n) \tag{3.24}$$

Replacing $\frac{\partial R}{\partial Q}$ on the left-hand side, Eq. (3.24) can be rewritten as

$$\{\frac{I}{J\Delta t} + \delta_\zeta(\frac{\partial \hat{f}}{\partial Q}) + \delta_\eta[\frac{\partial(\hat{g}-\hat{g}_v)}{\partial Q}]\}\Delta Q = R(Q^n) \qquad (3.25)$$

where

$$R(Q^n) = -[\delta_\zeta \hat{f} + \delta_\eta(\hat{g}-\hat{g}_v)]$$

Eq. (3.25) represents a large, banded, block (4x4) matrix equation for spatial discretization.

The spatially split approximate factorization (AF) technique and relaxation methods are applied. For the AF technique, Eq. (3.25) can be factored to yield

$$[\frac{I}{J\Delta t} + \delta_\zeta(\frac{\partial \hat{f}}{\partial Q})](\frac{I}{J\Delta t})^{-1}[\frac{I}{J\Delta t} + \delta_\eta \frac{\partial(\hat{g}-\hat{g}_v)}{\partial Q}]\Delta Q = R(Q^n)$$

In this form, the solution is easily obtained by solving the two, one-dimensional problems. For the relaxation scheme, the Eq. (3.25) is used to yield the difference equation as

$$\overline{D}\,\Delta Q_{j-2} + \overline{A}\,\Delta Q_{j-1} + \overline{B}\,\Delta Q + \overline{C}\,\Delta Q_{j+1} + \overline{E}\,\Delta Q_{j+2} + \overline{H}\,\Delta Q_{i-2} + \overline{F}\,\Delta Q_{i-1} + \overline{G}\,\Delta Q_{i+1} + \overline{I}\,\Delta Q_{i+2} = R$$

If Gauss-Seidel schemes are applied; the vertical line Gauss-Seidel (VLGS) can be implemented with left-to-right sweeping ($\overline{G} = \overline{I} = 0$) or with right-to-left sweeping ($\overline{H} = \overline{F} = 0$) , the horizontal line Gauss-Seidel (HLGS) with

bottom-to-top sweeping ($\overline{C} = \overline{E} = 0$) or with top-to-bottom sweeping ($\overline{D} = \overline{A} = 0$) .

In order to raise the accuracy in space, the level of accuracy in approximating $(\frac{\partial u}{\partial x})_i$ can be written as

$$(u_L)_{i+\frac{1}{2}} = u_i + \frac{1}{4}[(1 + K)\Delta + (1 - K)\nabla] u_i \qquad (3.26)$$

where $\nabla u_i = u_i - u_{i-1}$ and $\Delta u_i = u_{i+1} - u_i$. The third-order accuracy (K = 1/3) with no limit is applied.

3.5 Numerical Domain and Boundary Conditions

3.5.1 Domain and Mesh Grid

Since the flows of interest are two-dimensional, the plane of 2-D flowfield was considered for the present cases. The origin of the reference coordinates was taken at the point of exit of the injection on the wall for slot cases, or at a leading edge of the flat plate for one of the turbulent boundary layer cases.

Mesh grids with clustering near the wall were adopted. Along the streamwise direction, a uniform mesh is applied. Typical (41x101) mesh grids for slot cases are show in Fig. 2(a), and a half of the mesh grid is located near the region of the

splitter and the wall. Grids with (33x77) points for the shock-wave/turbulent shear-layer interaction cases, and (91x101) mesh grids for the turbulent boundary layer cases were chosen. For the turbulent boundary layer flow over a flat plate, which is one wall of the wind tunnel nozzle, mesh grids only clustered near the wall were used. For the other turbulent boundary layer flow over a flat plate with the leading edge, the mech grids with both clustering near the wall and the leading edge are illustrated in Fig. 2(b).

3.5.2 Boundary Conditions

Specification of the boundary conditions is closely related to the domain and mesh. After careful examination, the values of boundary conditions are put on the first cell face on the boundary. The same types of boundary conditions were used in all test cases.

In order to generate the numerical boundary conditions at the inflow boundary for the slot injection flows, the boundary layer thickness at the slot exit was measured from the experimental Schlieren pictures. The light intensity in a Schlieren picture is proportional to the gradient of density, but we consider, approximately, this thickness from the Schlieren picture as density or thermal boundary layer thickness. Assuming the total temperature is constant, the relation between temperature and velocity can be written as follows:

$$\frac{T}{T_\infty} = \frac{T_o}{T_\infty} - \frac{\gamma - 1}{2} M_\infty^2 \left(\frac{u}{u_\infty}\right)^2 \qquad (3.27)$$

or

$$\frac{T}{T_\infty} = 1 + \sqrt[3]{Pr}\,\frac{\gamma-1}{2} M_\infty^2 [1 - (\frac{u}{u_\infty})^2] \qquad (3.28)$$

we assumed a linear relation velocity profile in the laminar boundary layer; $\frac{u}{u_\infty} = (\frac{y}{\delta})^{1/7}$ was used in the turbulent boundary layer flows. For the inflow boundaries of the shock-wave/turbulent shear-layer and boundary-layer interactions and calculating the last station for slot injection problems, the experimental and numerical data at the upstream station were applied. For the inflow boundaries of the turbulent boundary layer problems, the freestream data and experimental data were used for the flat plate with a leading edge and the flat plate which is one wall of the nozzle, respectively. For wall boundary conditions, the no-slip, adiabatic, solid wall boundary condition was adopted for the slot cases and the shock-wave interaction cases. The adiabatic temperature of the wall is calculated by $T_{aw} = T_\infty + \sqrt[3]{Pr}\,(T_o - T_\infty)$. For the wall boundary conditions of the turbulent boundary layer problems, the no-slip, heat-transfer solid wall boundary condition was applied. Extrapolation with second order accuracy was applied to both the outflow boundary and top boundary.

IV. TEST PROBLEMS, RESULTS AND DISCUSSIONS

4.1 Test Problems

In order to test the new turbulent model, six test cases consisting of slot injection problems, shock-wave/turbulent shear-layer and boundary-layer interactions, and high-speed, turbulent boundary layer problems were chosen, and solutions with both the current model and Prandtl's model were obtained and compared with experimental results.

The first slot test case is supersonic injection ($M_2 = 2.0$) into a primary flow at $M_1 = 2.85$; the second test case is sonic injection ($M_2 = 1.0$) and the Mach number of the primary flow is still 2.85. For those two problems, the experimental data were taken from experiments done by Gilreath and Schetz [77] in an

atmospheric intake wind tunnel. From the Schlieren photographs of the experiments, it was found that the shear layer flows are turbulent and the wall boundary layer flows are laminar.

The third test case was designed to predict more complicated slot injection flows, where both the shear layer and the wall boundary layer are turbulent. In this test case, the Mach numbers of the slot injection flow and primary flow are 1.7 and 3.0, respectively. The new turbulent model was used in the wall boundary layer. For this problem, experimental data from Ref. [10], which were refined by Smith, in the supersonic blow-down type wind tunnel were available.

For the above three test cases, the experiments were air to air injection at the same total temperature of 535° R. The slot height was 0.5 inch and the free stream Reynolds numbers per foot were 1.4 and 7.5 million, respectively. The static pressures of three cases at the slot exit were slightly lower than the static pressures of the freestream primary flow.

The fourth test case is a heated, supersonic slot injection problem. The total temperature of the slot injection air for this test case was heated to 755°R. The Mach numbers and total pressures of the slot injection flow and primary flow are the same as those of the third test case. The axial velocity of the slot injection flow is increased to approach the velocity of freestream flow: the ratio of velocity $\frac{u_2}{u_1} = 0.86$, which is more than that of the third test case ($\frac{u_2}{u_1} = 0.75$). The density of the heated injection flow is decreased. For this problem, the

experimental data were taken from Ref. [78]. The main purpose of the investigation for this case is to prove that the new turbulent model can properly predict the effect of variation of density or temperature on the turbulence.

The fifth test case is the complicated flow of shock-wave/turbulent shear-layer and boundary-layer interactions. For these problems, the experimental data were from Ref. [10,78].

The final test cases are high-speed ($M_1 >> 1$) turbulent boundary layers over a flat plate with heat transfer. One case is a turbulent boundary layer over a flat plate which is one wall of the nozzle in a wind tunnel. The freestream Mach number, the ratio of the wall temperature to the freestream temperature (T_w/T_∞), and Reynolds number per foot were 4.67, 3.96, and 6.02 million, respectively. The experimental data were from Ref. [79]. The other case is flow over a flat plate with a sharp leading edge. The freestream Mach number , the ratio of the wall temperature to the freestream temperature (T_w/T_∞), and Reynolds number per foot were 6.55, 3.64, and 3.2 million, respectively. The experimental data were from Ref. [80,81].

The size of the computational domain in physical coordinates for the slot injection problems was 3.46 inches (y - direction) by 7.95 inches (x - direction). The computational domain was 2.1 inches by 6.36 inches for the shock-wave/turbulent shear-layer and boundary-layer interaction problem, and the origin of the reference coordinates was taken at the point of station 3 from

Refs.[10,78] on the wall. The computational domain was 3.46 inches by 38 inches for the turbulent boundary layer problems.

4.2 Results and Discusions

The computing times for the slot injection problems on the IBM 3039 to obtain 5×10^{-3} residual were less than 7 minutes for the new model and less than 5 minutes for Prandtl's model. For the shock-wave/turbulent shear-layer and boundary-layer interaction problems, the CPU times were decreased about 30 percent. For the high-speed turbulent boundary layer problems, the CPU times were about 16 minutes.

4.2.1 Supersonic Injection into Supersonic Flow at $M_1 = 2.85$

The predictions of nondimensional density profiles with both the new model and Prandtl model are shown in Figs. 3 to 5, compared with measured data of Ref. [77]. Figures 3 and 4 show the results at stations of 1 and 2 (x/a = 4 and 6). It is observed that the numerical results for the new model are in good agreement with the experimental data, except at the outer edge of the shear layer, and the predictions of Prandtl's model show a slower spreading of the shear layer. Figure 5 presents the results at station 3 (x/a = 9.25). A good agreement of predictions for the new model compared with experimental data is achieved, but the predicted spreading rate at the inner edge of the shear layer is a little too fast.

The density profile curvature from the new model is very similar to that of the profile from the experimental results. But, the predictions of Prandtl's model have some deficiencies.

The predicted profiles of Mach number near the shear layer of the slot injection for three the stations are displayed in Figs. 6 to 8. The trends are the same as stated previously. Figures 9 to 11 show the nondimensional velocity profiles near the shear layer region for three stations. Since the experimental data of Mach number and velocity are not available, it is not possible to compare with the numerical values.

Figure 12 shows the numerical contours of nondimensional density and the experimental Spark-Schlieren. The photo displays the small wave in the exit region of slot injection better, and one can clearly see the spreading of the shear layer. Figure 12(b) illustrates the numerical contour from Prandtl's model. Comparing Fig. 12(b) with the Spark-Schlieren, it appears to be spreading more slowly. However, using the new model, the spreading rate of the shear layer presented in Fig. 12(c) is similar to the experimental results.

Figure 13 shows a plot of the calculated nondimensional wall pressure distribution along the streamwise direction compared to experimental data. Here, the new model was used in the shear layer, and the laminar condition was applied in the wall boundary layer, which was mentioned before. It is clear that the predictions are in good agreement with the data.

4.2.2 Sonic Injection into Supersonic Flow at $M_1 = 2.85$

A comparison between the numerical results and experimental results for nondimensional density distributions from Ref. [77] are shown in Figs. 14 to 16. The three stations along the streamwise direction are represented. Figures 14 and 15 show the results at stations 1 and 2 (x/a = 3.3 and 5.0). It can be seen that the numerical predictions using the new model are close to the experimental predictions except at the inner edge of the shear layer. They are better than the numerical predictions using Prandtl's model. Figure 16 presents the results at station 3 (x/a = 6.7). The predicted density distribution with the new model is in satisfactory agreement with the experimental distribution and better than that of Prandtl's model.

The predicted profiles of Mach number near the shear layer region of the slot injection for the three stations are shown in Figs. 17 to 19. It is obvious that the spreading rate of Mach number predicted from Prandtl's model is slower than the spreading rate of Mach number predicted from the new model. The main reason is that the density gradient in the new model contributed to influence the turbulence. So, the predictions with the new model show a slightly faster spreading rate of the shear layer in the initial shear layer region. It is also faster than that of Prandtl's model in the developed shear layer region.

Figures 20 to 22 represent the profiles of nondimensional streamwise velocity at the three stations, and these illustrate the comparisons of predicted results

between the new model and Prandtl's model. As stated above, the spreading rate of velocity using the new model should be faster than that using Prandtl's model. It can be observed that the profiles of velocity are, basically, similar to Mach number profiles, only a little different at station 3. This is due to the no heat transfer boundary conditions.

4.2.3 Supersonic Injection into Supersonic Flow at $M_1 = 3.0$

The predicted profiles of the Mach number, nondimensional mean axial velocity and nondimensional density at station 1 ($\frac{x}{a} = 0.25$) are shown in Figs. 23 to 25, compared with the experimental data. The predictions of the profiles of the Mach number and the velocity are close to the experimental results, but the prediction of the density in the outer region has some discrepancy. The reason for that discrepancy between the numerical prediction and experimental data may be due to the assumed initial pressure distribution. In the numerical calculation, a sharp stepped initial transverse pressure profile from the slot static pressure to the freestream value was assumed. Of course, it can not exactly match with the experimental conditions. Another reason may be due to the measured data of temperature near the shock wave. The predictions of the new model and Prandtl's model are the same. The experimental results show a peak in the center of the slot exit region. The probable cause of that apparent peak is shock waves impinging on the static pressure taps on the cone-static probe in that region. The prediction of a nearly uniform inflow in the center of the slot exit may be more correct. The lowest value of predicted Mach number or velocity or

density is near $y = 0.46$ inch, while the slot lip is at y = 0.5 inch. However, the lowest value of measured Mach number or velocity or density is near $y = 0.43$ inch. That is due to the fact that the static pressure of the slot injection is a little lower than that of the primary flow, so the slot flow is compressed downward. The prediction of the new model has a very small wake in the inner edge region of the shear layer at station 2. The wake of the splitter plate has completely disappeared at station 3. (see subsequent figures)

The predicted profiles of the Mach number, velocity and the density at station 2 ($\frac{x}{a} = 4$) are displayed in Figs. 26 to 28, compared with the measured data. The predictions of the Mach number profile and the density profile in the outer edge region of the shear layer show that the spreading rates are faster than the spreading rates in the experiments. The predictive data of velocity for the new model are almost the same as the measured data. However, the prediction of Prandtl's model has a little slower spreading rate. Thus, the predicted data of Prandtl's model in the inner edge region of the shear layer show some differences from the experimental data.

In Figs. 29 to 31 are shown the profiles of the Mach number, velocity and density at station 3 ($\frac{x}{a} = 10$). The predictions of Prandtl's model show a little slower spreading rate; the predicted spreading rate of the new model appears rapid. Thus, the predictions of Prandtl's model are a little better than the predictions of the new model. Considering the complexity of turbulent mixing shear layer

of the supersonic slot injection problems, the overall agreement of the predictions are judged satisfactory.

As mentioned before, a (33x77) grid points and (6.36x2.1) inches computational domain was taken to calculate the distributions of the Mach number, velocity and density at station 4 ($\frac{x}{a} = 20$). For the inflow boundary, the experimental and numerical data at station 3 ($\frac{x}{a} = 10$) were applied. The profiles of the Mach number, velocity and density are shown in Figs. 32 to 34. It can be seen that the predictions of Prandtl's model indicate a smaller spreading width. The predicted velocities are lower than those of the experiments. However, the prediction of the new model is a little better. The predictions of the Mach number have some discrepancies. The experimental data have a peak in the outer region of the shear layer. The predictions may be correct, because here no waves cause the Mach number peak. The predicted data for the Mach number and velocity in the outer region of the shear layer are lower than those of the measured data, because the accelerations of the velocity and Mach number are a little slower. However, the differences between the numerical data and the measured data are in the region of acceptable error.

Figure 35 shows the contours of constant nondimensional density for the new model and the Spark-Schlieren. It is obvious that the predicted spreading width is a little faster than the experimental spreading width.

4.2.4 Heated Supersonic Injection into Flow of $M_1 = 3.0$

Generally, the total temperature of injection flow and primary flow in many experiments are the " room " temperature. If the injection air is heated, the density of the injection air can be decreased, and it will behave more like a light injection gas. Because the Mach numbers of the primary flow and the injection flow are still kept as in test case 3, *i.e.*, 3.0 and 1.7 respectively, the velocity of the injection flow is increased here to approach the velocity of primary flow.

Figures 36 to 38 show the distributions of the Mach number, velocity and density at station 1 ($\frac{x}{a} = 0.25$). The predictions of the profiles of the Mach number and the velocity are in agreement with the measured data, but the prediction of the density profile still shows a discrepancy. The measured data are less than the predicted data in the outer region of slot injection. The reason has been discussed previously. The predictions of the new model and Prandtl's model are the same, because the spreading width of the shear-layer is smaller. The experimental results have a pronounced peak in the center of the slot exit region. The reason has been discussed before.

The profiles of the Mach number, velocity and density for station 2 ($\frac{x}{a} = 4$) are displayed in Figures 39 to 41. The predicted data for both the new turbulent model and Prandtl's model are compared with measured data. It can be seen that the predictions are in good agreement with the experimental results, especially for the new model. Figure 39 presents the profiles of the Mach number. Figure 40

shows the distribution of the nondimensional mean axial velocity. The prediction of the new model is almost the same as that of the experimental results, and the prediction of Prandtl's model shows a little difference due to a slower spreading rate. Figures 41 presents the profiles of nondimensional density. It is obvious that the predicted spreading rate of Prandtl's model are slower than the experimental spreading rate, but the predicted spreading rate of the new model is a little too rapid. As compared with test case 3, the predicted spreading width from Prandtl's model for the heated injection test case should be a little narrower due to the decrease of the gradient of velocity, as u_2 is approaching to u_1.

The profiles of the Mach number, velocity and density at station 3 ($\frac{x}{a} = 10$) are shown in Figs. 42 to 44. The predicted profiles are basically in agreement with the measured data, but the spreading widths of the predictions of the new model are wider than those of experiments. So, the predictions of the Mach number and density of Prandtl's model are a little better than those of the new model, but the predicted velocity data from the new model are closer to the measured data.

The profiles of the Mach number, velocity and density at station 4 ($\frac{x}{a} = 20$) are displayed in Figs. 45 to 47. It has been noted previously that the prediction with Prandtl's model shows a narrow spreading width, but the predicted width of the new model is wider than that of the experiments. The predicted Mach number profile of Prandtl's model looks good due to a narrow spreading width. The experimental data show a peak in the outer region of the shear layer, which has been discussed previously. However, overall for this case, the predictions of

the profiles of the velocity and the density of the new model are better than those of Prandtl's model.

As stated previously, the experimental results show that the spreading rate of shear layer of heated slot injection flow is a little more rapid than that of the unheated slot injection flow (test case 3). This trend is identical to that commented on in Ref. [82] for the experiments of light jet gas injection. Since, for heated injection flow, the velocity gradient between the primary flow and the injection flow is decreased, according to Prandtl's model, the eddy viscosity should be decreased. In fact, it is not. This is due to the effect of the density on the turbulence. So, it is reasonable that the Prandtl's model approach is inadequate for prediction of the current test case, especially for more heated injection flow conditions, in which the velocities of slot injection flows are close to the velocity of the primary flows. Hence, the new model which considers the influence of density may better predict that phenomena.

4.2.5 Shock-Wave/Turbulent Shear-Layer and Boundary-Layer Interaction

The spark-Schlieren from the experiments is shown in Fig. 48(a). The incident shock wave was generated from the top of the wind tunnel using a compression ramp, and it reflects essentially from the top of the turbulent shear layer which has been merged with the turbulent wall boundary layer. Figure 48(b) shows the computational results of the density contours for this problem using the new model. Compared with spark-Schlieren of the experiments, it looks basically the

same, and it can be seen that the incident shock wave is not strong enough to separate the boundary-layer. The incident shock-wave penetrates into the region between the shear-layer and boundary-layer. That layer thickness is increased, and the wave reflection is spread out over several layer heights due to the interaction with the mixing-layer.

The wall static pressure along the streamwise direction is shown in Fig. 49. The incident shock wave causes the wall static pressure rise. The predictions of numerical results are basically in agreement with the experimental data. However the prediction of the new turbulent model is better than that of Prandtl's model.

The measured profiles of the Mach number, velocity and density are located at station 4, $\frac{x}{a} = 20$. The profiles of the Mach number, velocity and density are displayed in the Figs. 50 to 52. The Mach number profiles in Fig. 50 show that the prediction data of the new model is close to the measured data and slightly better than those of Prandtl's model. The velocity distribution is in Fig. 51. It can be seen that the prediction of the new model is again somewhat better than that of Prandtl's model. Figure 52 shows the density profiles. The prediction of the new model is in good agreement with the experiments; the predicted data with Prandtl's model are lower than the measured data. It can be seen that there are small bumps in the profiles for Prandtl's model. The reason may be due to the intensity of turbulence. At that station, the predictions of Prandtl's model indicate that both the shear layer and the wall boundary layer do not merge togather. Thus, it may predict small bumps because of a shock wave/turbulent

shear layer interaction. For the new model, no bumps appear in the profiles, because both the shear layer and the wall boundary layer are predicted to have been merged togather, Which are the same as experimental results.

The next test case was shock wave interaction with the heated injection shear layer. Figures 53 to 55 show the predictions of the profiles of the Mach number, velocity and density with heated mixing-layer. It is obvious that the predictions of the new model are close to the experimental results. However, the predictions of Prandtl's model show some discrepancies, especially for the bumps in the profiles. The reason has been explained previously, because the predicted spreading width of Prandtl's model is smaller than that of the new model for heated injection flow.

4.2.6 Hypersonic Turbulent Boundary Layer Flow over a Flat Plate

For the first case from Ref. [79], the measured data of the Mach number, velocity and density are located at x = 57.25 and 69.25 inches from the nozzle throat. To start the numerical calculations, the measured data at the location, x = 57.25 inches, were used as initial inflow boundary data. Then we sought to predict the profiles of Mach number, velocity and density at the location of 69.25 inches. Figures 56 to 58 show the predictions and the data of the profiles of the Mach number, velocity and density at that location. It is obvious that the agreement between the experimental and computational profiles can be considered good, except for the density profiles. The predictions of the new model and Prandtl's

model are basically the same. Ref. [79] reported the skin friction coefficient, $C_f = 0.00073$ at this station, and the calculation with the new model predicted $C_f = 0.00064$. This result basically agrees with experiment. It can be seen that the predicted profiles of Mach number, velocity and density appear a little "noisy". The reason may be due to the initial inflow boundary data, which were taken from the measured data and were not smooth. In the inner region of the turbulent boundary layer, the predictions of the new model are perhaps a little better than the predictions of the Prandtl model. These results are in good agreement with the conclusions pointed out by Maise and McDonald [51]. They observed the experimental data on compressible boundary layers up to a Mach number of 5, and concluded that the effect of compressibility on the mixing length could be neglected.

For the other turbulent boundary layer case, a 4-foot flat plate with a sharp leading edge was put in the freestream flows of $M_\infty = 6.55$. The measured data of the velocity are located at x=26 and 35 inches from the leading edge. It is obvious that the uniform freestream values were used as the initial inflow boundary values. Figures 59 and 60 show the predictions of the velocity profiles at the locations, x=26 and 35 inches. It can be seen that there are small depressions in the velocity profiles for the new model. The probable cause is the density gradient variation, because the temperature profile on a flat plate for high Mach number boundary layer flows with heat transfer (T_w/T_∞ = constant) has a peak within the layer. On the other hand, the density variations are only produced by temperature variations in the boundary layer for single-species gas

flows. Thus, the mean density profile has a minimum, it must have a point where $\frac{\partial \overline{\rho}}{\partial y} = 0$. The velocity profiles for a turbulent boundary layer at x = 26 inches are shown in Fig. 59. The agreement between the measured data and the data predicted by the new model is considered good. However, the prediction of Prandtl's model becomes increasing inadequate in higher Mach number flows. Figure 60 shows the comparison between the experiment and the prediction at the downstream station. The agreement has some discrepancy. But, the prediction of the new model is better than that of Prandtl's model. For this case, it was difficult to precisely determine the laminar region, the transition region and turbulent region along the flat plate, especially the transition region in the experiments. No results were reported. We roughly assumed two regions, *i.e.*, laminar and turbulent regions. Instantaneous transition was assumed to take place at a streamwise distance, x = 4 inches, from the leading edge, as determined by a crude critical, length Reynolds number, $Re_{x,crit} \simeq 10^6$. Maybe, the major reason for the dicrepancy of numerical and experimental data might be explained by this transition to the turbulent region.

V. CONCLUDING REMARKS

In this study, we have found and demonstrated a new mixing-length model to predict the mean flowfields of turbulent, supersonic flows with large density and Mach number variations such as slot injection cases, shock-wave/turbulent shear-layer and boundary-layer interactions, and high Mach number turbulent boundary layer flows. The new model and the original Prandtl model were used in an effective numerical technique, based on Roe's flux difference splitting method. Some important results drawn from the derivation of the new modeling and computational results of six test cases can be summarized as follows:

The new mixing-length turbulence model considers the effects of the compressibility on the turbulence. For incompressible flow, the new mixing-length model collapses back to Prandtl's original mixing-length model. Due to the inclusion of the effects of compressibility on the turbulence, the new mixing-length model has demonstrated the ability to provide better predictions of variable density and Mach number cases than Prandtl's original mixing-length

model, so that the new model can be applied to explain some new phenomena which can not be explained by Prandtl's model.

For sonic and supersonic slot injection into supersonic flows, comparisons show that the predictions of the new mixing-length model are better than those of Prandtl's model, in comparison with the measured data. Moreover, for heated or light gas injection problems, Prandtl's model will become increasingly inadequate, especially for more heated injection flow in which the slot injection velocity almost approachs the velocity of the primary flow.

For the shock-wave/turbulent shear-layer and boundary-layer problems, the agreement of predictions with measured data is satisfactory, and the predictions with the new model are better than the predictions with Prandtl's model.

For the turbulent boundary layer flows at high supersonic Mach numbers ($M_1 \leq 5$), the agreements between the experiments and the predictions of both the new model and Prandtl's model are considered good. For higher Mach number turbulent boundary layer flows ($M_1 > 5$), the predictions of the new model are better than the predictions of Prandtl's model, because the new model considers the effect of the compressibility on the turbulence.

The current work represents a first step of a new stage in the search for a new turbulent model in considering the effects of compressiblity on turbulence, especially in hypersonic flow with heat and mass transfer. Of course, the tasks for

the future are many. Predictions of the new model have not been compared with the predictions of TKE and K-ε turbulent models. However, we believe that the new model is better for engineering applications, because it is simpler and has demonstrated faithful representation of physical phenomena.

REFERENCES

1. Visich, Jr., M. and Libby, P. A., "Experimental Investigation of Mixing of Mach Number 3.95 Stream in Presence of Wall," NASA TN D-247, Feb., 1960.

2. McRee, D. I., Peterson, J. B. and Braslow, A. L., "Effect of Air Injection Through a Porous Surface and Through Slots on Turbulent Skin Friction Mach 3," NASA TN D-2427, Aug. 1964.

3. Goldstein, R. J., Eckert, E. R. G., Tsou, R. K. and Haji-Skeikh, A., "Film Cooling with Air and Helium Injection Through a Rearward-Facing Slot into a Supersonic Air Flow," AIAA Journal, Vol.4, No.6, 1966, pp.981-985.

4. Gilreath, H. E. and Schetz, J. A., "A Study of Tangential Slot Injection in Supersonic Flow," AIAA Journal, Vol.5, No.12, 1967, pp.2149-2154.

5. Schetz, J. A., Gilreath, H. E. and Lubard, S. C., "Fuel Injection and Mixing in a Supersonic Stream," Twelfth Symposium on Combustion, 1969.

6. Parthasarathy, K. and Zakkay, V., "An Experimental Investigation of Turbulent Slot Injection at Mach 6," AIAA Journal, Vol.8, No.7, July 1970, pp.1302-1307.

7. Cary, A. M. and Hefner, J. N., "An Investigation of Film Cooling Effectiveness and Skin Friction in Hypersonic Turbulent Flow," AIAA-71-70, June, 1971.

8. Kenworthy, M. and Schetz, J. A., "An Experimental Study of Slot Injection into a Supersonic Stream," NASA CR-2128, Jan. 1973.

9. Schetz, J. A., *Injection and Mixing in Turbulent Flow*, Progress in Astronautics and Aeronautics Vol.68, AIAA, New York, 1980.

10. Walker, D. A., Campbell, R. L. and Schetz, J. A., "Turbulence Measurements for Slot Injection in Supersonic Flow," AIAA-88-0123, Jan. 1988.

11. Glauert, M. B., "The Wall Jet," Journal of Fluid Mechanics, Jan. 1956, pp.625.

12. Patankar, S. V. and Spalding, D. B., *Heat and Mass Transfer in Bounday Layer*; Morgan-Crampion, London (1967)

13. Beckwith, I. E. and Bushnell, D. M., "Calculation by a Finite-Difference Method of Supersonic Turbulent Boundary Layers with Tangential Slot Injection," NASA TN D-6221, 1971.

14. Bushnell, D. M., "Calculation of Relaxing Turbulent Boundary Layers Downstream of Tangential Slot Injection," J. Spacecraft & Rockets, Vol.8, No.5, May 1971, pp.550-551.

15. Yoon, S. J. and Schetz, J. A., "Numerical Navier-Stokes Solutions of Supersonic Slot Injection Problems," AIAA-88-3710 , July 25-28, Cincinnati, Ohio, 1988.

16. Birch, S. F. and Eggers, J. M., "A Critical Review of the Experimental Data for Developed Free Turbulent Shear Layers," NASA SP-321, 1973, pp.11-37.

17. Seban, R. A. and Back, L. H., "Velocity and Temperature Profiles in Turbulent Boudary Layers with Tangential Injection," Trans. ASME, Ser. C: J. Heat Transfer, Vol.84, No.1, Feb. 1962, pp.45-54.

18. Baker, R. L. and Weinstein, H., "Experimental Investigation of the Mixing of Two Parallel Streams of Dissimilar Fluids," NASA CR-957, 1968.

19. Yule, A. J., "Spreading of Turbulent Mixing Layers," AIAA J., Vol.10, No.5, May 1972, pp.686-687.

20. Brown, G. L. and Roshko, A., "On Density Effects and Large Structure in Turbulent Mixing Layers," Journal of Fluid Mechanics, Vol.64, Pt.4, 1974, pp.775-816.

21. Chinzei, N., Masuya, G., Komuro, A., Murakami and Kudou, K., "Spreading of Two-Stream Supersonic Turbulent Mixing Layers," Phys. Fluids 29(5), May 1986, pp.1345-1347.

22. Messersmith, N. L., Goebel, S. G., Frantz, W. H., Krammer, E. A., Renie, J. P., Dutton, J. C. and Krier, H., "Experimental and Analystical Investigations of Supersonic Mixing Layers," AIAA-88-0702.

23. Gooderum, P. B., Wood, G. P. and Brevoort, M. J.,"Investigation with an Interferometer of the Turbulent Mixing of a Free Supersonic Jet," NACA Rep.936, 1950.

24. Bershader, D. and Pai, S. I., "On Turbulent Jet Mixing in Two-Dimensional Supersonic Flow," J. Appl. Phys., Vol.21, No.6, June 1950, pp.616.

25. Sirieix, M. and Solignac, J. L., "Contribution a L'Etude Experimentale de la Couche de Melange Turbulent Isobare d'un Ecoulement Supersonique," Separated Flows, Pt.I, AGARD CP No.4, May 1966, pp.241-270.

26. Browand, F. K. and Latigo, B. O., "Growth of the Two-Dimensional Mixing Layer from a Turbulent and Nonturbulent Boundary Layer," Phys. of Fluids 22(6), June 1979, pp.1011-1019.

27. Bradshaw, P., "The Effect of Initial Conditions on the Development of a Free Shear Layer," J. Fluid Mech., Vol.26,Pt.2, Oct. 1966, pp.225-236.

28. Abramovich, G. N., *The Theory of Turbulent Jets*, M.I.T. Press, C. 1963.

29. Abramovich, G. N., Yakovlevsky, O. V., Smirnova, I. P., Secundov, A. N. and Krasheninnikov, S. Yu., "An Investigation of the Turbulent Jets of Different Gases in a General Stream," Astronaut. Acta, Vol.14, No.3, Mar. 1969, pp.229-240.

30. Johnson, D. A., "An Investgation of the Turbulent Mixing between Two Parallel Gas Streams of Different Composition and Density with a Laser Doppler Velocimeter," Ph.D. Diss., Univ. of Missouri, 1971.

31. Bogdanoff, D. W., "Interferometric Measurement of Heterogeneous Shear Layer Spreading Rates," J. AIAA, Vol.22, No.11, 1984, pp.1550-1555.

32. Papamoschou, D. and Roshko, A., "Observations of Supersonic Free Shear Layers," AIAA-86-0162.

33. Schlichting, H., *Boundary Layer Theory*, McGraw-Hill, New York, 1942; 7TH ed., 1979.

34. Görtler, H., "Berechnung Von Aufgaben Der Freien Turbulenz auf Grund Eines Neuen Näherungsansatzes," Z. Angew. Math. Mech., Bd.22, Nr.5, Oct. 1942, pp.244-254.

35. Liepmann, H. W. and Laufer, J., "Investigations of Free Turbulent Mixing," NACA TN 1257, 1947.

36. Elassar, R. J. and Pandolfini, P. P., "An Examination of Eddy Viscosity Models for Turbulent Free Shear Flows," Paper No.71-FE-17, ASME, May 9-12, 1971.

37. Wagner, R. D., "Measured and Calculated Mean-Flow Properties of a Two-Dimensional, Hypersonic, Turbulent Wake," NASA TN D-6927, 1972.

38. Harsha, P. T., "Free Turbulent Mixing: A Critical Evaluation of Theory and Experiment," Turbulent Shear Flows, AGARD CP-93 (1971).

39. Schetz, J. A., "Free Turbulent Mixing in a Coflowing Stream," NASA SP-321, 1972, pp.259-275.

40. Rudy, D. H. and Bushnell, D. M., "A Rational Aproach to the Use of Prandtl's Mixing Length Model in Free Turbulent Shear Flow Calculations," NASA SP-321, 1972, pp.67-137.

41. Rodi, W. and Spalding, D. B., "A Two-Parameter Model of Turbulence, and Its Application to Free Jets," Wärme-und Stoffübertragung, Vol.3,No.2, 1970, pp.85-95.

42. Launder, B., Morse, A., Rodi, W. and Spalding, D. B., "Prediction of Free Shear Flows- A Comparison of the Performance of Six Turbulence Models," NASA SP-321, 1972.

43. Spalding, D. B., "A Two-Equation Model of Turbulence," VDI-Forsch., Heft 549, 1972, pp.5-16.

44. Harsha, P. T., "Prediction of Free Turbulent Mixing Using a Turbulent Kinetic Energy Method," NASA SP-321, 1972.

45. Lockwood, F. C. and Stolakis, P., "Assessment of Two- Turbulence Models for Turbulent Round Diffusion Jets with Combustion," Turbulent Shear Flow.4 (1983), pp.328-344.

46. Schetz, J. A., *Foundations of Boundary Layer Theory for Momentum,Heat and Mass Transfer*, Prentice-Hall, INC. Englewood Cliffs, New Jersey, 1984.

47. Schetz, J. A., "Some Studies of the Turbulent Wake Problem," Astonautica Acta, 1971, Vol.16, pp.107-117.

48. Horstman, C. C., "Prediction of Hypersonic Shock-Wave/ Turbulent-Boundary-Layer Interaction Flows," AIAA-87-1367, June 8-10, 1987.

49. Zang, T. A., Hussain, H. Y. and Bushnell, D. M., "Numerical Computations of Turbulence Amplification in Shock-Wave Interactions," AIAA J., Vol. 22 (1984), pp.13-21.

50. Van Driest, E. R., "Turbulent Bounbary Layer in Compressible Fluid," J. Aeronaut. Sci., Vol.18, No.3, Mar., 1951, pp.145-160.

51. Maise, G. and McDonald, H., "Mixing Length and Kinematic Eddy Viscosity in a Compressible Boundary Layer," AIAA Journal, Vol.6, 1967, pp.73-80.

52. Bushnell, D. M. and Beckwith, I. E., "Calculation of Nonequilibrium Hypersonic Turbulent Boundary Layers and Comparisons with Experimental Data," AIAA Journal, Vol.8, No.8, Aug. 1970, pp.1462-1469.

53. Favre, A., "Statistical Equations of Turbulent Gases," Problems of Hydrodynamics and Continum Mechanics, Soc. Indust. & Appl. Math. 1969, pp.231-266.

54. Boussinesq, J.(1877), "Theorie de l'écoulement Tourbillant," Mém. Prés. Acad. Sci. XXIII, 46, Paris.

55. Hinze, J. O., *Turbulence*, McGraw-Hill, New York, 1959.

56. Prandtl, L.(1925), "Bericht über Untersuchungen zur Ausgebildeten Turbulenz," ZAMM,5,136.

57. Taylor, G. I., "Statistical Theory of Turbulence," (1935), Turbulence-Classic Papers on Statistical Theory, Edited by Friedlauder, S. K. and Topper, L..

58. Cebeci, T., "Calculation of Compressible Turbulent Boundary Layers with Heat and Mass Transfer," AIAA Journal, Vol.9, 1971, pp.1091-1097.

59. Cebeci, T. and Smith, A. M. O., "Analysis of Turbulent Boundary Layers," Academic Press, New York, 1974.

60. Baldwin, B. S. and Lomax, H., "Thin Layer Approximation and Algebraic Model for Seperated Turbulent Flows," AIAA-78-257, Huntsville, AL., 1978.

61. Ferri, A., Libby, P. A. and Zakkay, V., "Theoretical and Experimental Investigation of Supersonic Combustion," High Temperatures in Aeronautics, Carlo Ferrari, ed., Pergamon Press, 1964, pp.55-118.

62. Peters, C. E., "A Model for the Free Turbulent Eddy Viscosity," AEDC-TR-65-209, U.S. Air Force, Nov. 1965 (AD 473663).

63. Cohen, L. S., "A Kinematic Eddy Viscosity Model Including the Influence of Density Variations and Preturbulence," NASA SP-321, 1972.

64. Eckert, E. R. G., *Analysis of Heat and Mass Transfer*, McGraw-Hill, 1972.

65. Scott, J. N. and Hankey, W. L., "Numerical Simulation of Excited Jet Mixing Layers," AIAA-87-0016, Jan.12-15, Reno, Nevada, 1987.

66. Oh, Y. H., "Analysis of Two-Dimensional Free Turbulent Mixing," AIAA-74-594, Paloalto, CA, June 17-19, 1974.

67. Warming, R. F. and Beam, R. M.(1975), "Upwind Second-Order Difference Schemes and Applications in Unsteady Aerodynamic Flows," Proc. AIAA 2nd Computational Fluid Dynamics Cofference, Hartford, Connecticut, pp.17-18.

68. Steger, J. L. and Warming, R. F.(1979), "Flux Vector Splitting of the Inviscid Gasdynamic Equations with Application to Finite-Difference Methods," NASA TN D-78605.

69. Roe, P. L., "Characteristic-Based Schemes for the Euler Equation," Ann. Rev. Fluid Mech., Vol.18, 1986, pp.337-365.

70. Roe, P. L., "Approximate Riemann Solvers, Parameter Vectors and Difference Schemes," J. Computational Physics, Vol.43, 1981, pp.357-372.

71. Van Leer, B., "Flux-Vector Splitting for the Euler Equations," Lecture Notes in Physics, Vol.170, 1982.

72. Steger, J. L. and Warming, R. F., "Flux Vector Splitting of the Inviscid Gasdynamic Equations with Application to Finite-Difference Methods," Journal of Computational Physics, Vol.40, 1981, pp.263-293.

73. Grossman, B. and Walters, R. W., "An Analysis of Flux-Split Algorithms for Euler's Equations with Real Gases," AIAA-87-1117-CP, Honolulu, Hawaii, June 9-11, 1987.

74. Thomas, J. L. and Walters, R. W., "Upwind Relaxation Algorithms for the Navier-Stokes Equations," AIAA-85-1501-CP, July 15-17, Cincinnati, Ohio, 1985.

75. Newsome, R. W., Walters, R. W. and Thomas, J. L., "An Effecient Iteration Strategy for Upwind/Relaxation Solutions to the Thin-Layer Navier-Stokes Equations," AIAA-87-1113-CP,June 9-11, 1987.

76. Anderson, D. A., Tannehill, J. C. and Pletcher, R. H., *Computational Fluid Mechanics and Heat Transfer*, Hemisphere Pub. Co., New York, 1984.

77. Gilreath, H. E. and Schetz, J. A., "Transition and Mixing in the Shear Layer Produced by Tangential Injection in Supersonic Flow," Journal of Basic Engineering, Dec. 1971, pp.610-618.

78. Smith, B. R., "Mean Flow Measurements of Heated Supersonic Slot Injection into a High Reynolds Number Supersonic Stream," V.P.I.,Thesis,1989, Aerospace and Ocean Engineering.

79. Lee, R. E., Yanta, W. J. and Leonas, A. C., "Velocity Profile, Skin-Friction Balance and Heat-Transfer Measurements of the Turbulent Boundary Layer at Mach 5 and Zero-Pressure Gradient," NOLTR-69-106, 16 June, 1969.

80. Nielsen, J. N. and Kuhn, G. D., "Recent Applications of the Method of Integral Relations to Turbulent Boundary Layers with Heat Transfer and Pressure Gradients," NASA SP-216, 1968, pp.389-410.

81. Kutschenreuter, P. H., Jr., Brown, D. L., Hoelmer, W., *et al* ., "Investigation of Hypersonic Inlet Shock-Wave Boundary Layer Interaction," Part II-Continuous Flow Test and Analyses. AFFDL-TR-65-36, Apr. 1966, AD 636981.

82. Tombach, I. H., "Velocity Measurements with a New Probe in Inhomogeneous Turbulent Jets," CIT, Ph.D., 1969, Engineering, Aeronautical.

Figures

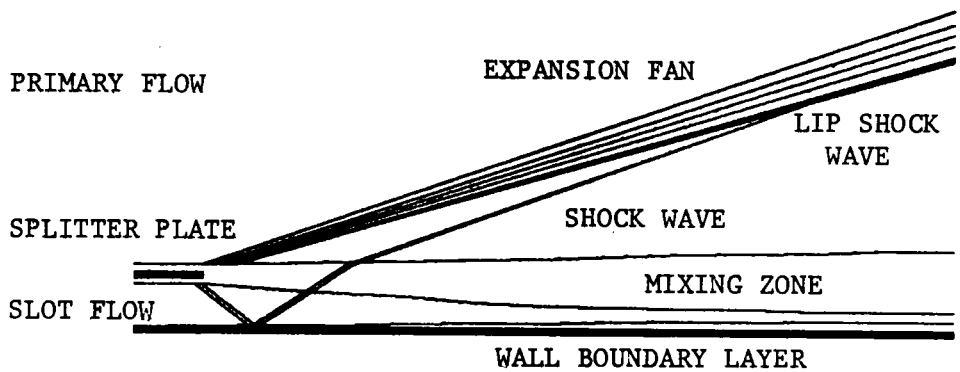

Figure 1. Schematic of slot injection in primary supersonic flow.

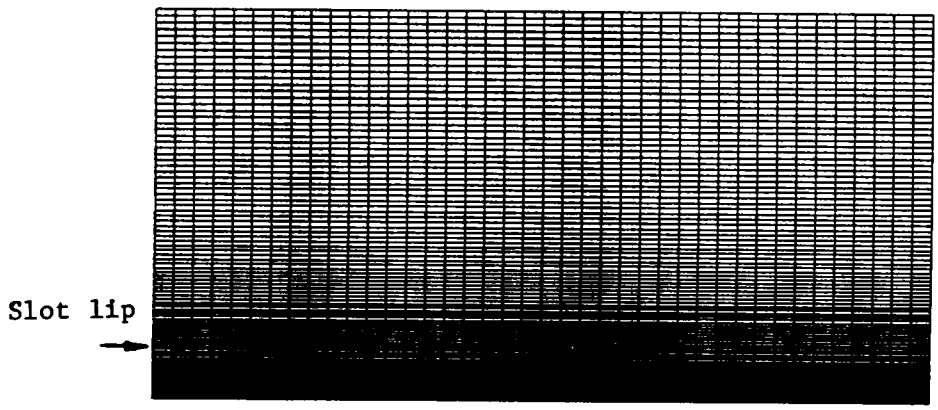

(a) (41x101)

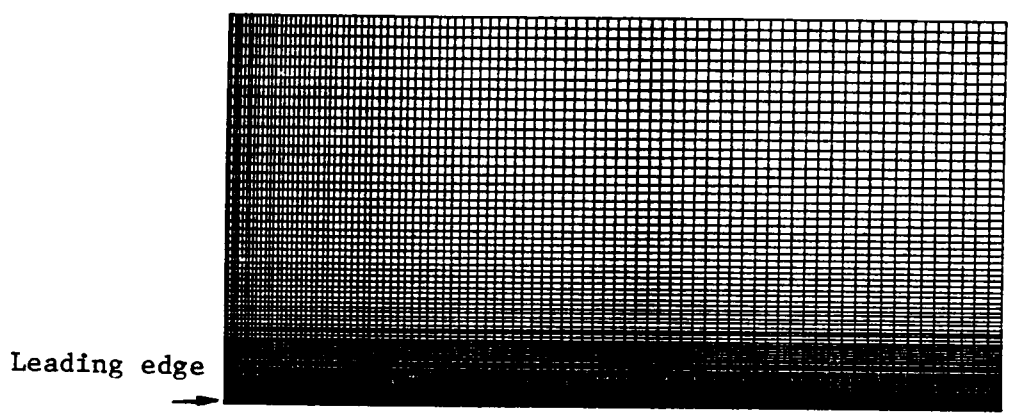

(b) (91x101)

Figure 2. (a) Typical computational grids used for slot injection flows and (b) typical computational grids used for turbulent boundary layer flows over a flat plate with a leading edge.

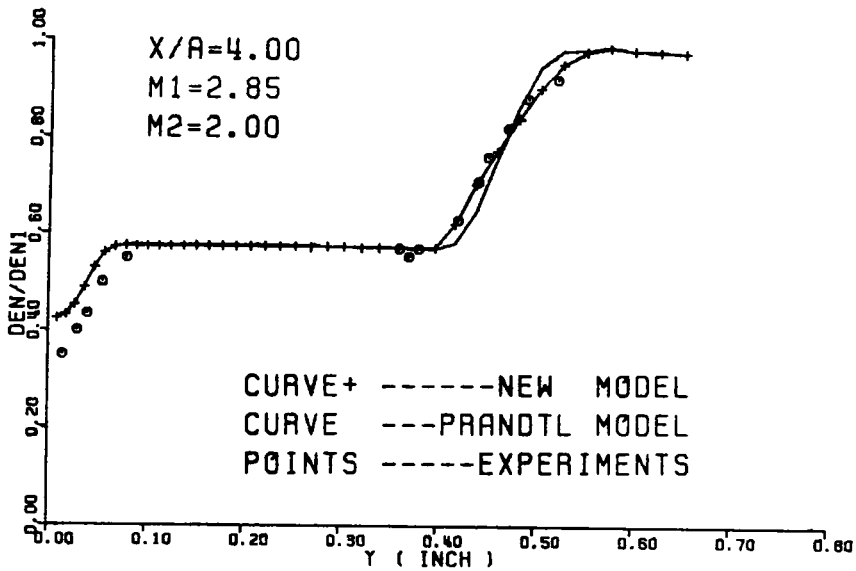

Figure 3. Density profile at x/a = 4.00, for the case of $M_1 = 2.85$, $M_2 = 2.0$ (measured data from Ref. [77])

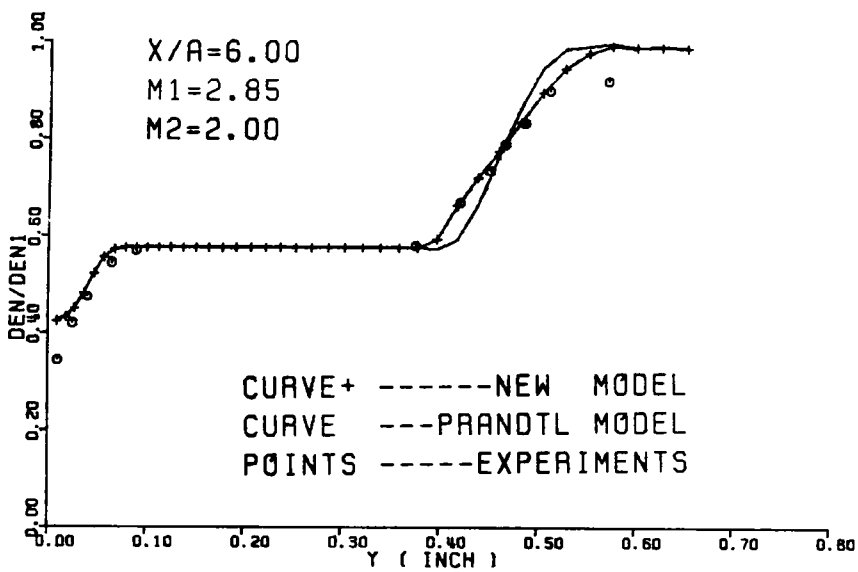

Figure 4. Density profile at x/a = 6.00, for the case of $M_1 = 2.85$, $M_2 = 2.0$ (measured data from Ref. [77])

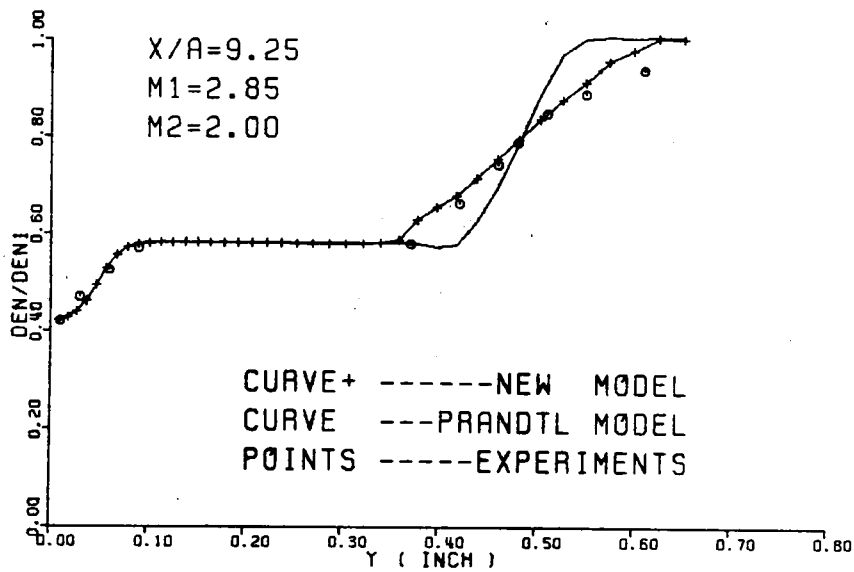

Figure 5. Density profile at x/a = 9.25, for the case of $M_1 = 2.85$, $M_2 = 2.0$ (measured data from Ref. [77])

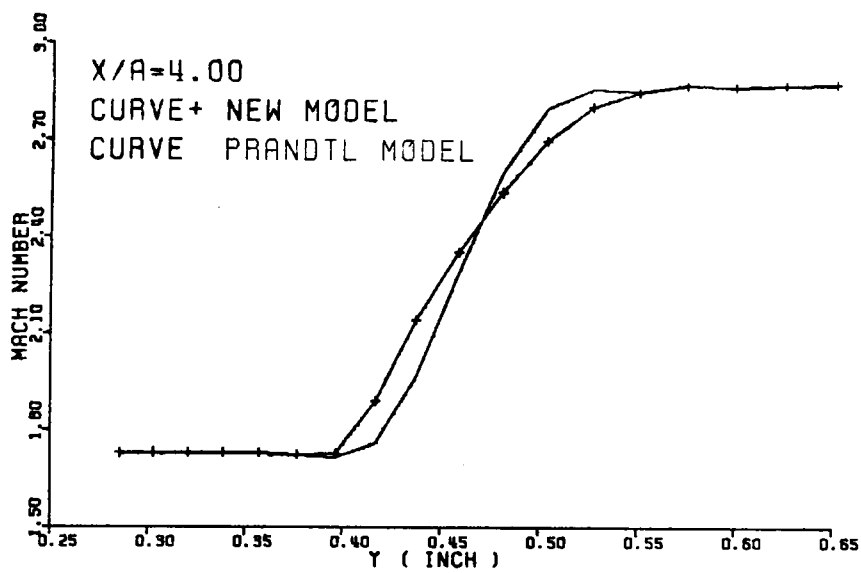

Figure 6. Mach number profile at x/a = 4.00, for $M_1 = 2.85$, $M_2 = 2.0$.

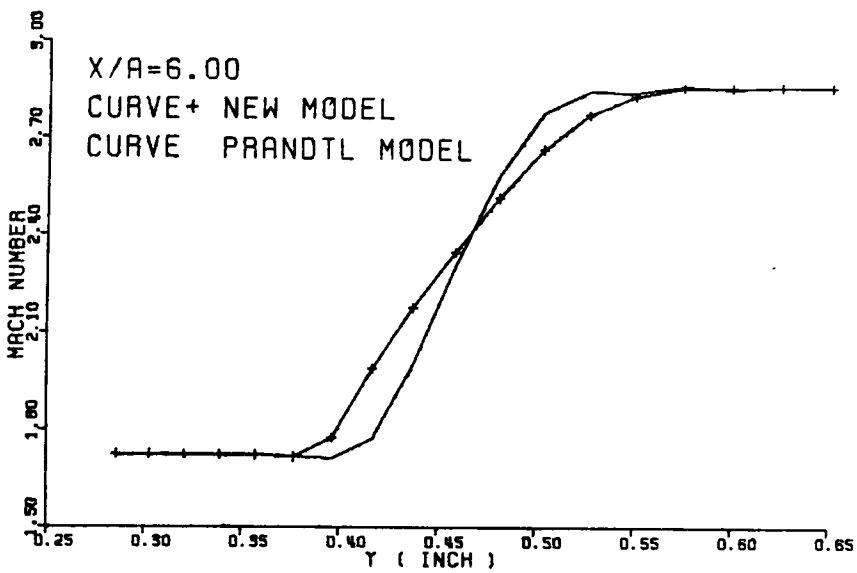

Figure 7. Mach number profile at x/a = 6.00, for $M_1 = 2.85$, $M_2 = 2.0$.

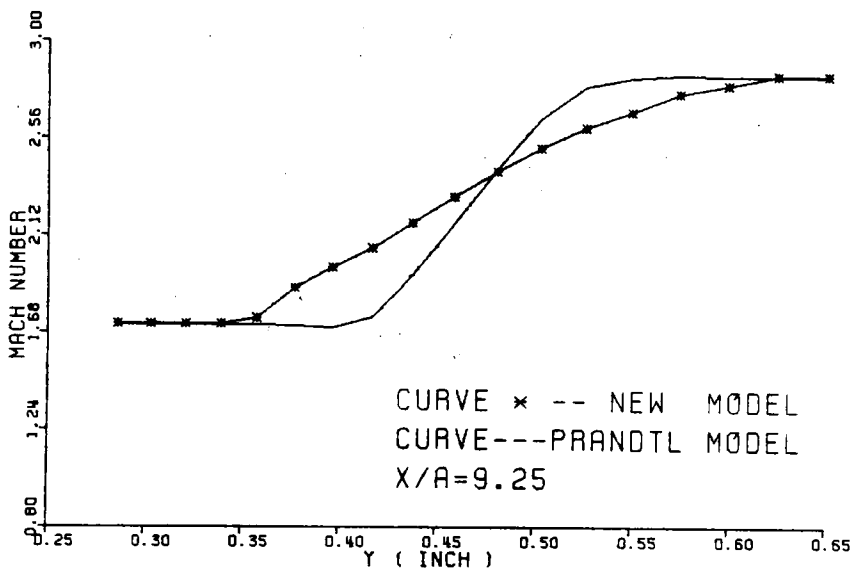

Figure 8. Mach number profile at x/a = 9.25, for $M_1 = 2.85$, $M_2 = 2.0$.

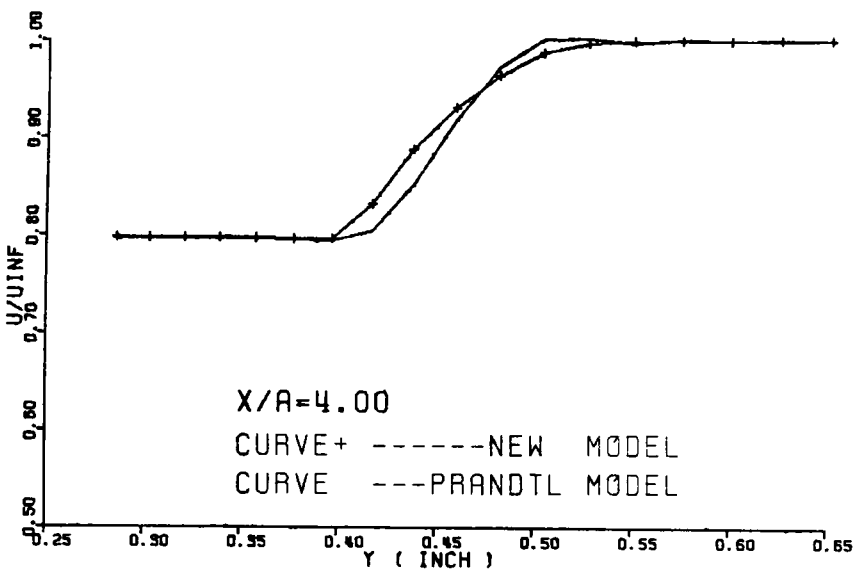

Figure 9. Velocity profile at x/a = 4.00, for $M_1 = 2.85$, $M_2 = 2.0$.

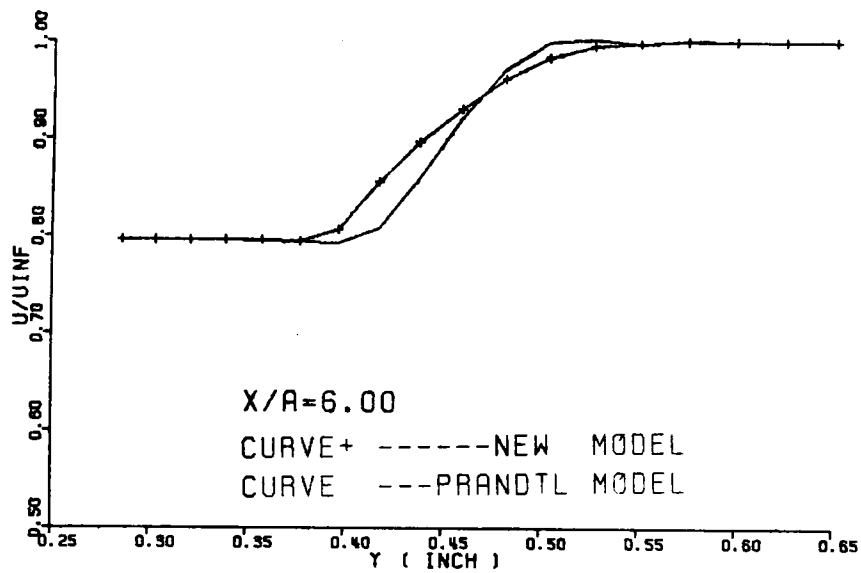

Figure 10. Velocity profile at x/a = 6.00, for $M_1 = 2.85$, $M_2 = 2.0$.

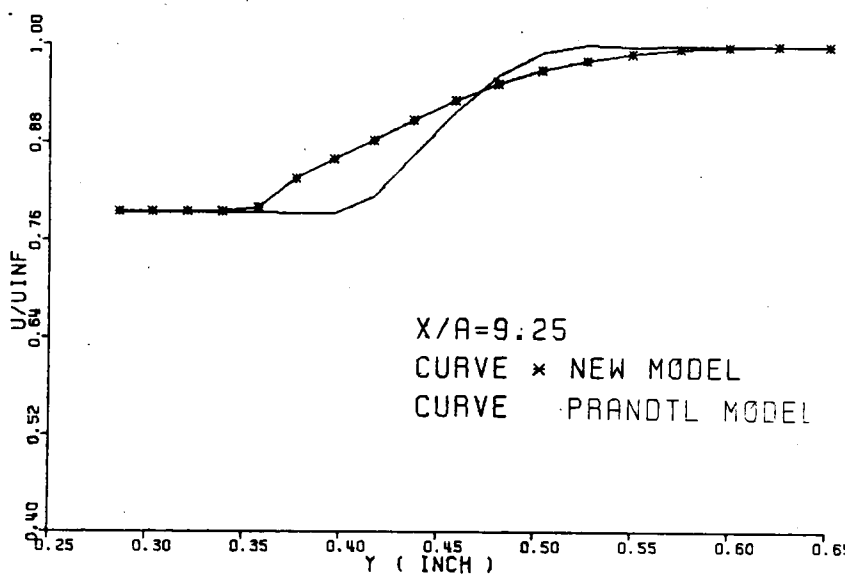

Figure 11. Velocity profile at x/a = 9.25, for $M_1 = 2.85$, $M_2 = 2.0$.

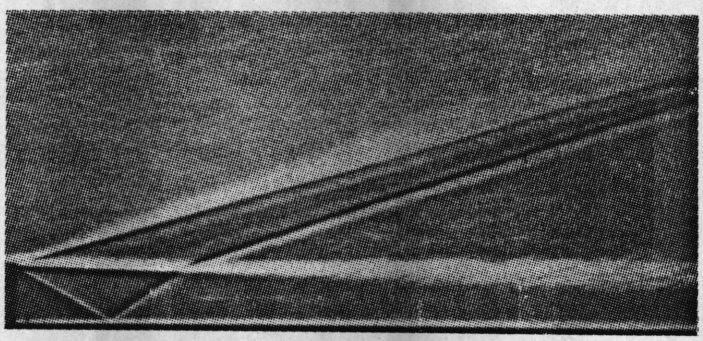

(a)

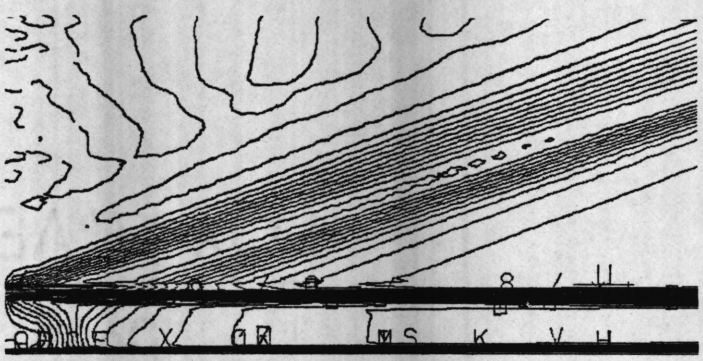

(b)

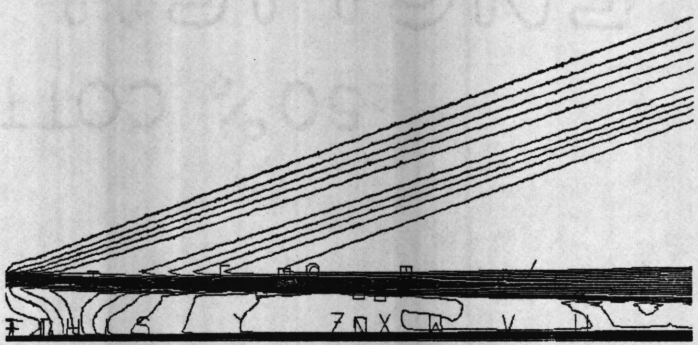

(c)

Figure 12. (a) Experimental Spark-Schlieren from Ref. [77] , (b) numerical density contour of Prandtl's model, and (c) numerical density contour of the new model for $M_1 = 2.85$, $M_2 = 2.0$.

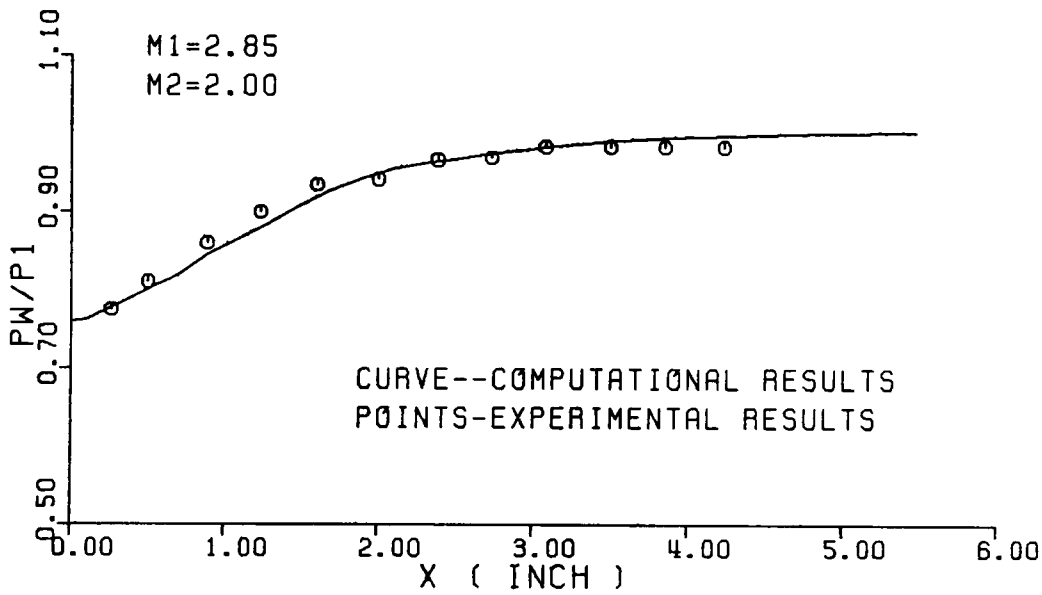

Figure 13. Wall presure distribution for slot injection, $M_1 = 2.85$, $M_2 = 2.0$ (measured data from Ref. [77])

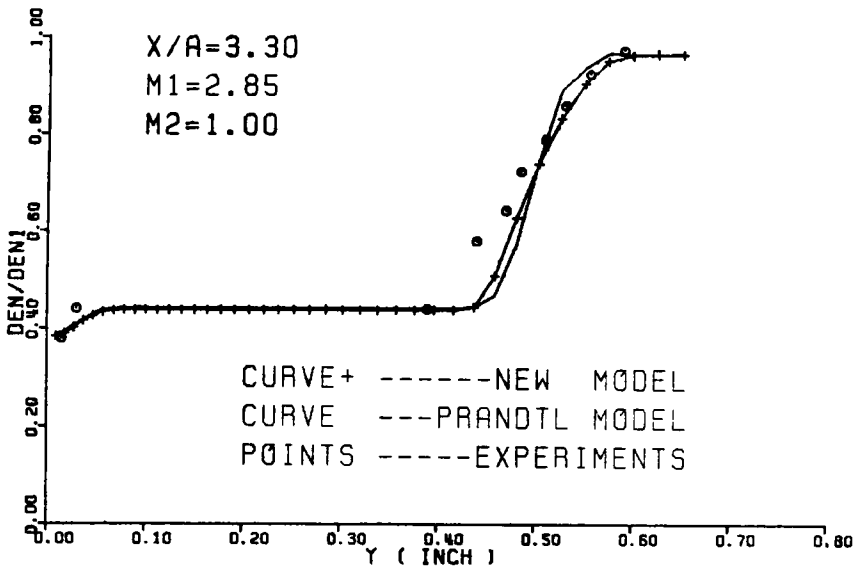

Figure 14. Density profile at x/a = 3.30, for the case of $M_1 = 2.85$, $M_2 = 1.0$ (measured data from Ref. [77])

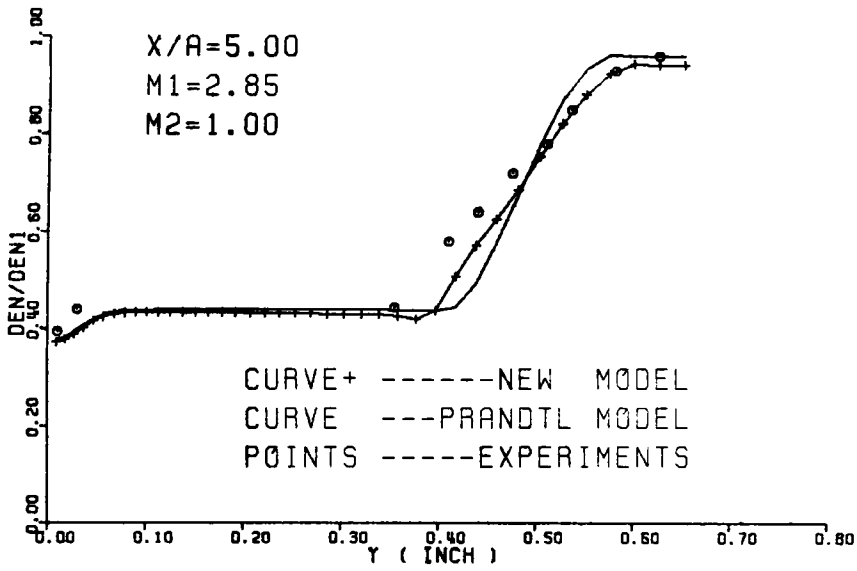

Figure 15. Density profile at x/a = 5.00, for the case of $M_1 = 2.85$, $M_2 = 1.0$ (measured data from Ref. [77])

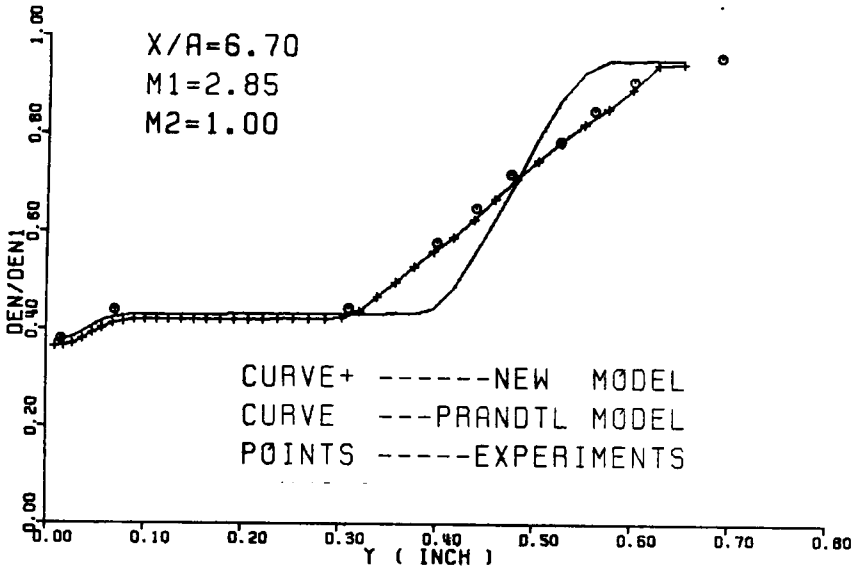

Figure 16. Density profile at x/a = 6.70, for the case of $M_1 = 2.85$, $M_2 = 1.0$ (measured data from Ref. [77])

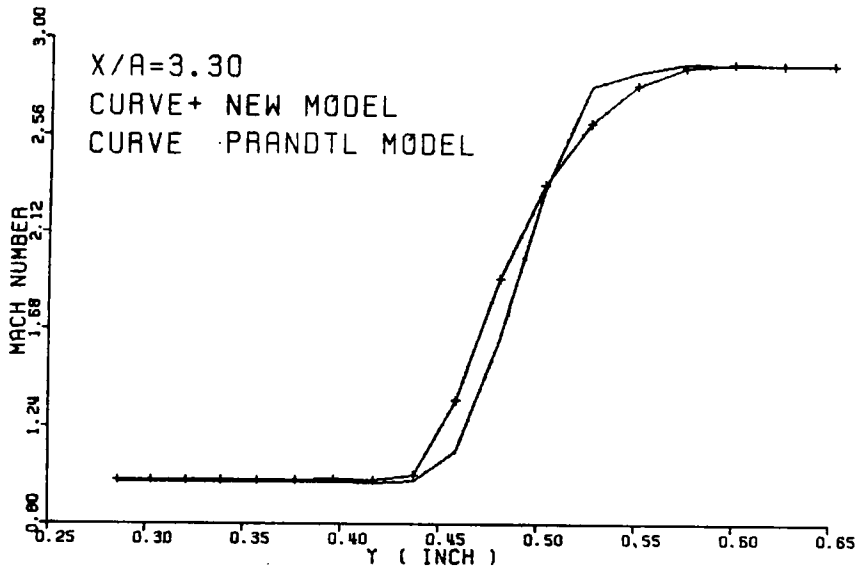

Figure 17. Mach number profile at x/a = 3.30, for $M_1 = 2.85$, $M_2 = 1.0$.

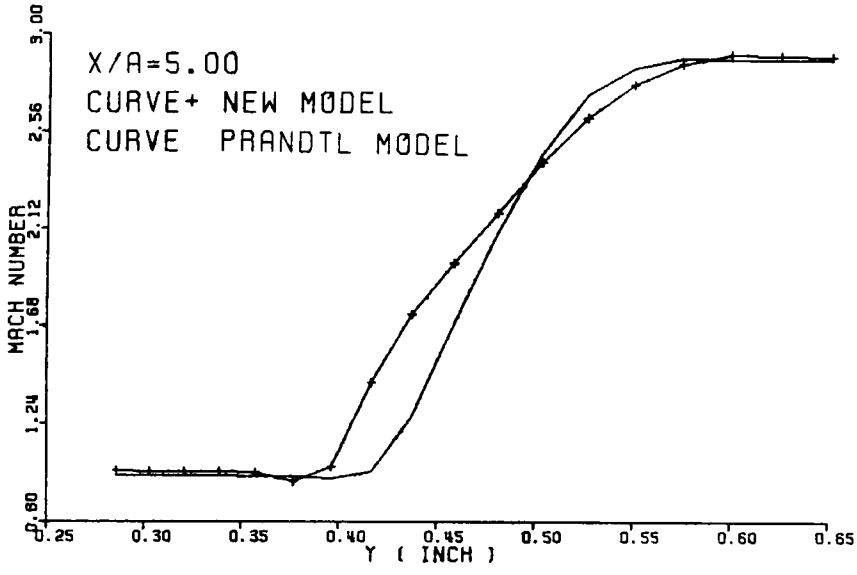

Figure 18. Mach number profile at x/a = 5.00, for $M_1 = 2.85$, $M_2 = 1.0$.

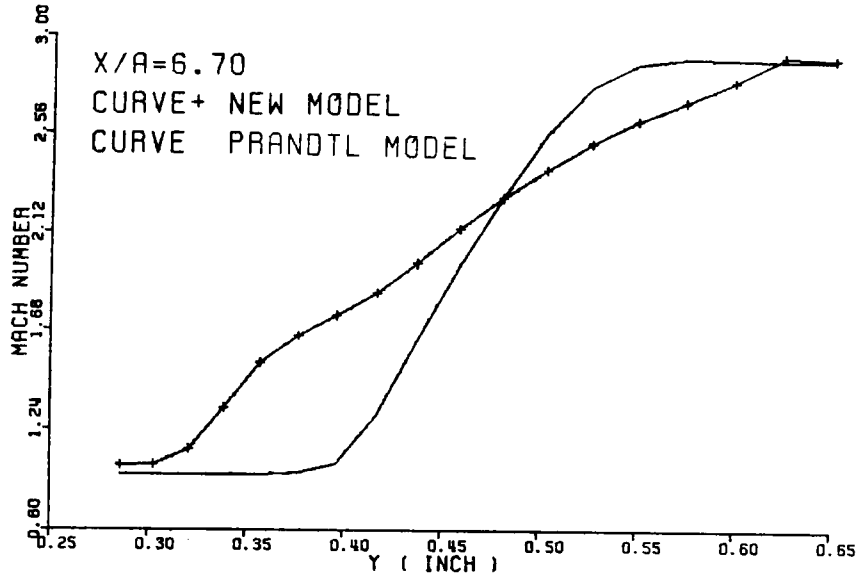

Figure 19. Mach number profile at x/a = 6.70, for $M_1 = 2.85$, $M_2 = 1.0$.

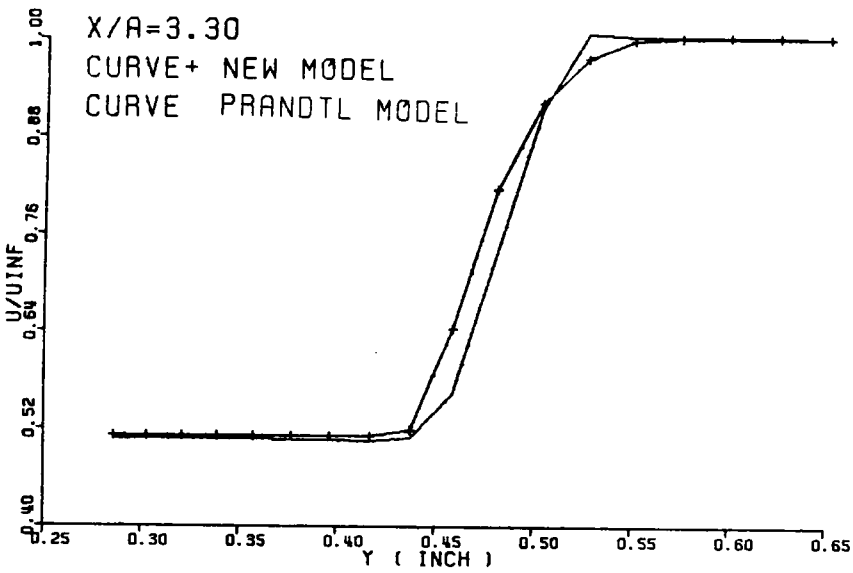

Figure 20. Velocity profile at x/a = 3.30, for $M_1 = 2.85$, $M_2 = 1.0$.

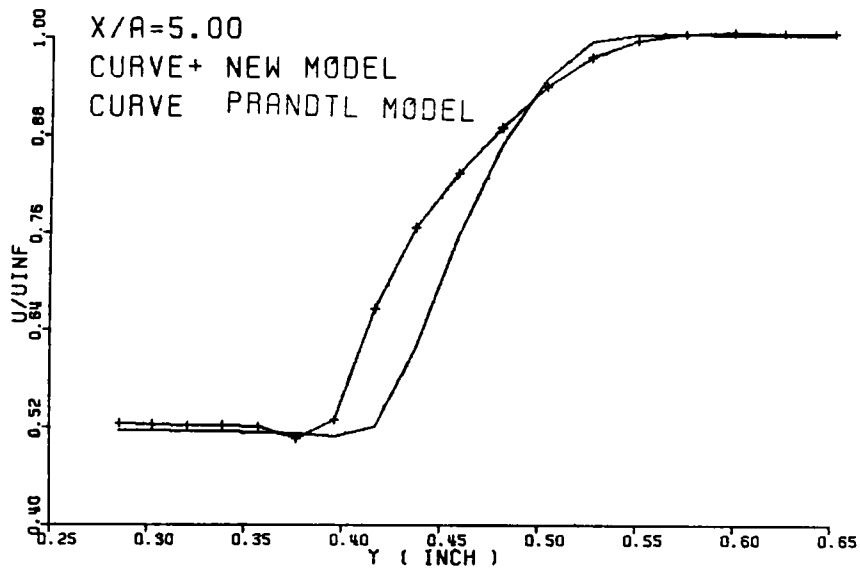

Figure 21. Velocity profile at x/a = 5.00, for $M_1 = 2.85$, $M_2 = 1.0$.

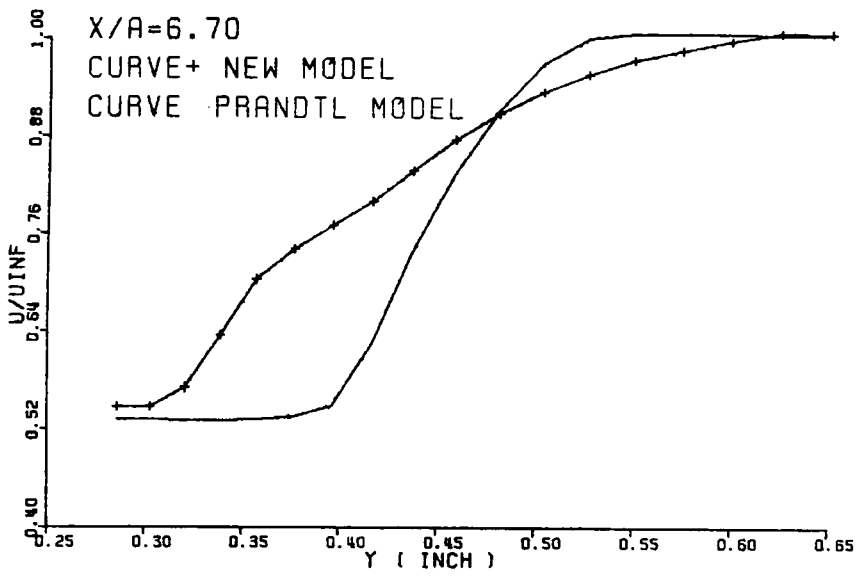

Figure 22. Velocity profile at x/a = 6.70, for $M_1 = 2.85$, $M_2 = 1.0$.

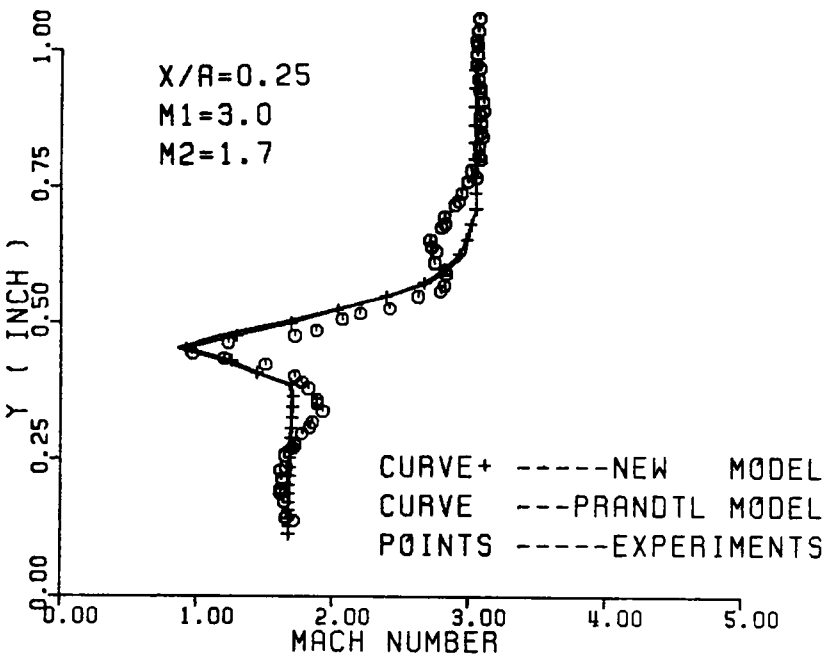

Figure 23. Mach number profile at x/a = 0.25, for $M_1 = 3.0$, $M_2 = 1.7$. (measured data from Ref. [10])

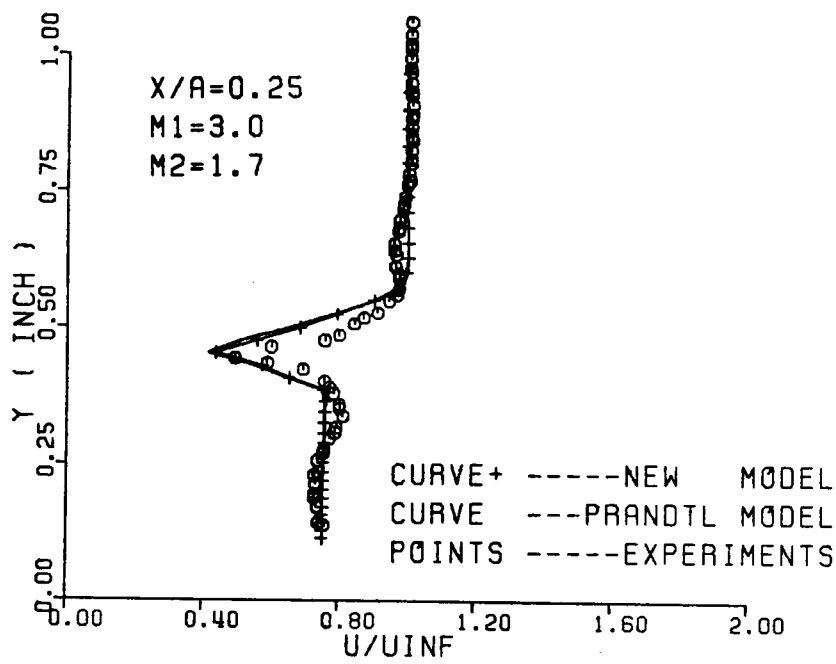

Figure 24. Velocity profile at x/a = 0.25, for the case of $M_1 = 3.0$, $M_2 = 1.7$ (measured data from Ref. [10])

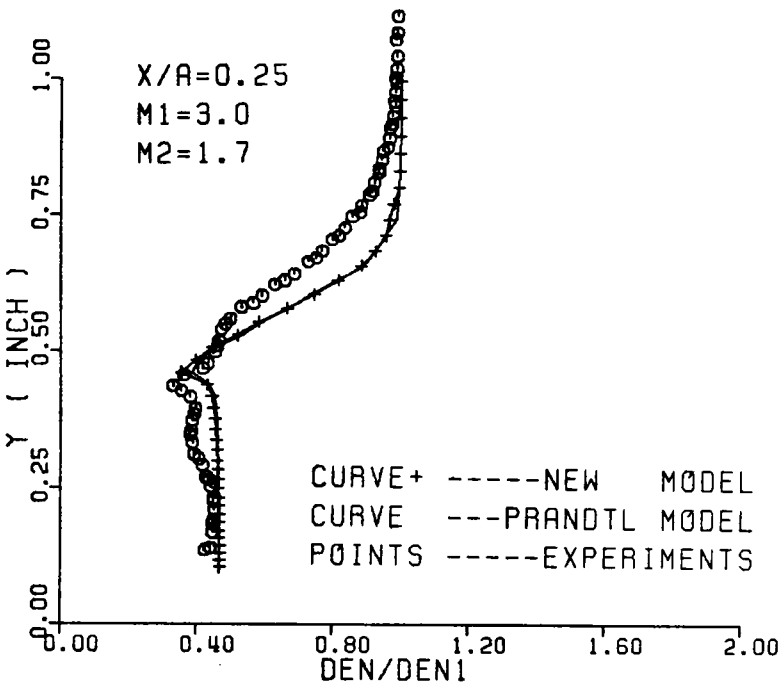

Figure 25. Density profile at x/a = 0.25, for the case of $M_1 = 3.0$, $M_2 = 1.7$ (measured data from Ref. [10])

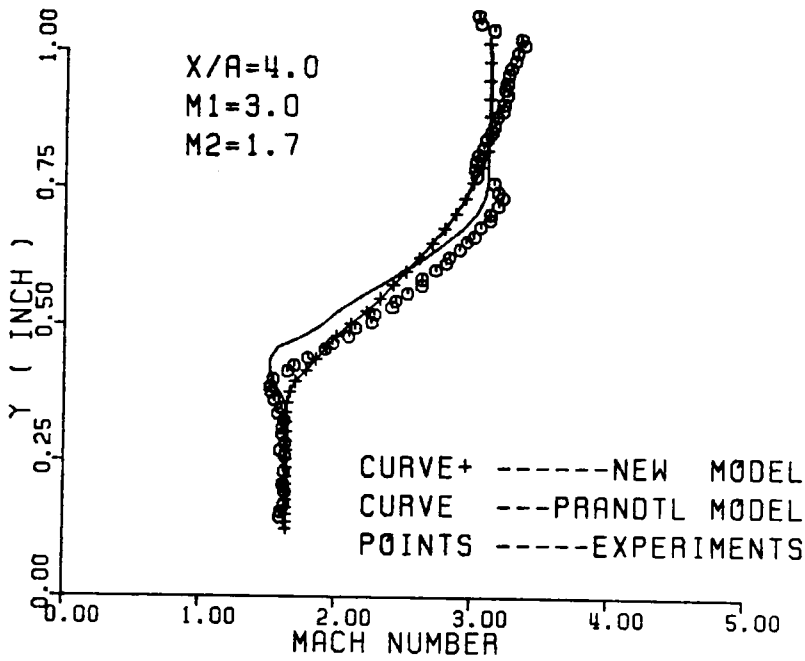

Figure 26. Mach number profile at x/a = 4.00, for $M_1 = 3.0$, $M_2 = 1.7$. (measured data from Ref. [10])

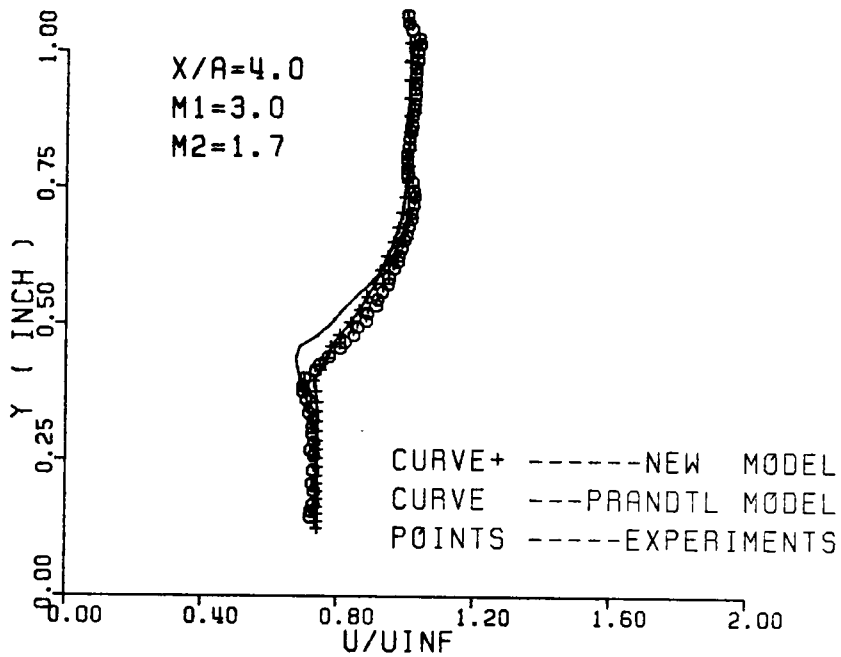

Figure 27. Velocity profile at x/a = 4.00, for the case of $M_1 = 3.0$, $M_2 = 1.7$ (measured data from Ref. [10])

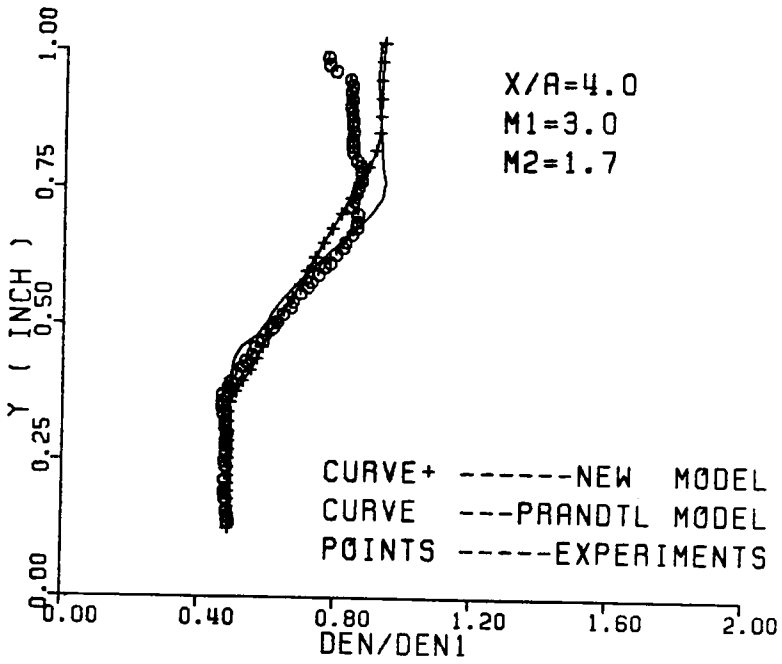

Figure 28. Density profile at x/a = 4.00, for the case of $M_1 = 3.0$, $M_2 = 1.7$ (measured data from Ref. [10])

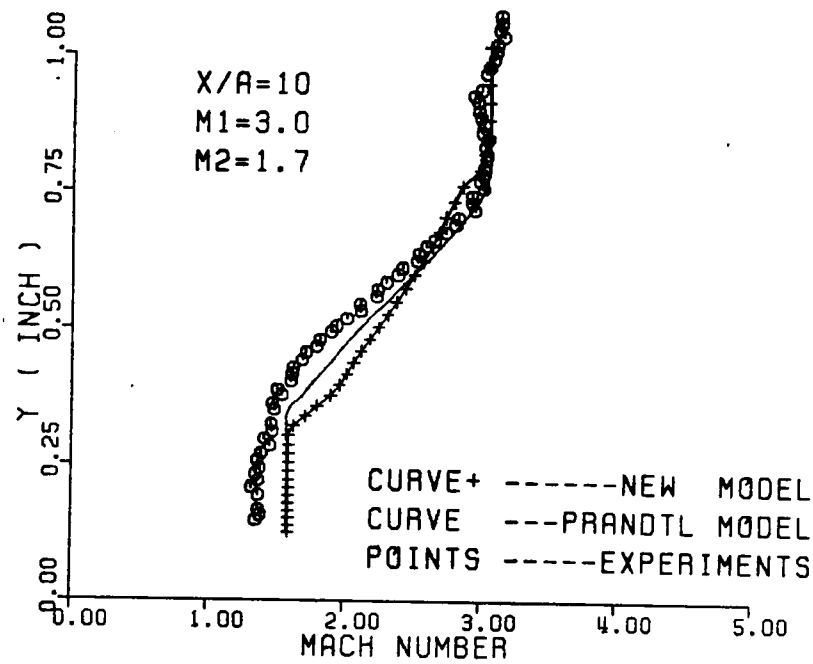

Figure 29. Mach number profile at x/a = 10.0, for $M_1 = 3.0$, $M_2 = 1.7$. (measured data from Ref. [10])

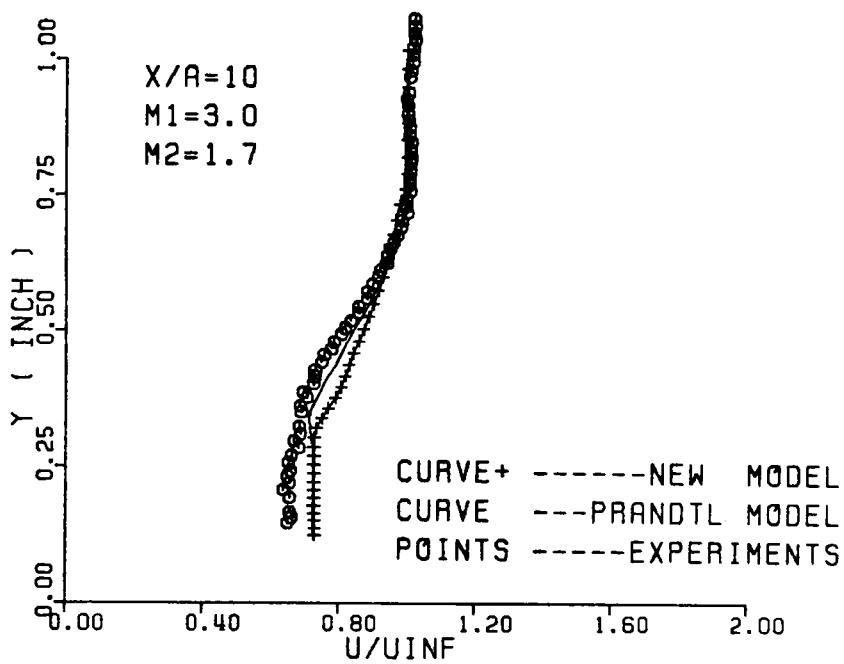

Figure 30. Velocity profile at x/a = 10.0, for the case of $M_1 = 3.0$, $M_2 = 1.7$ (measured data from Ref. [10])

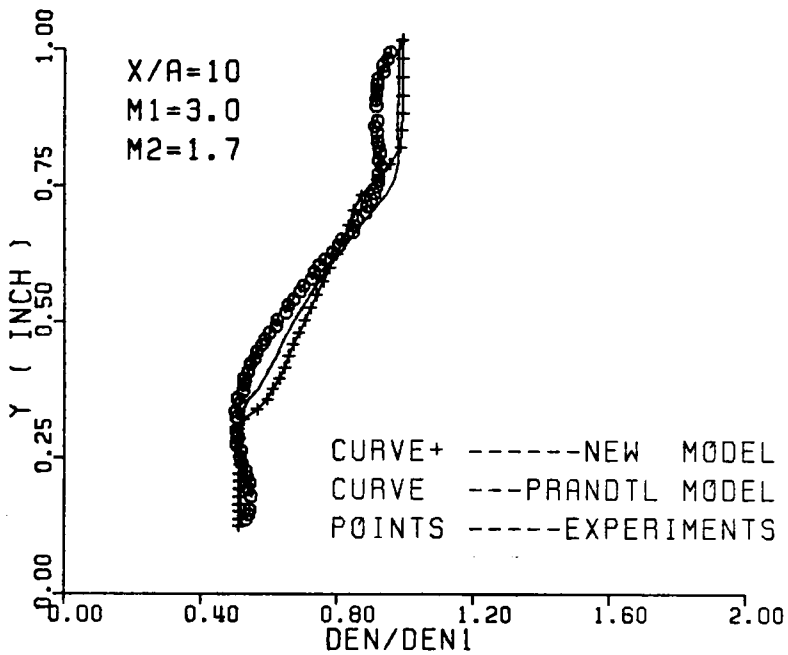

Figure 31. Density profile at x/a = 10.0, for the case of $M_1 = 3.0$, $M_2 = 1.7$ (measured data from Ref. [10])

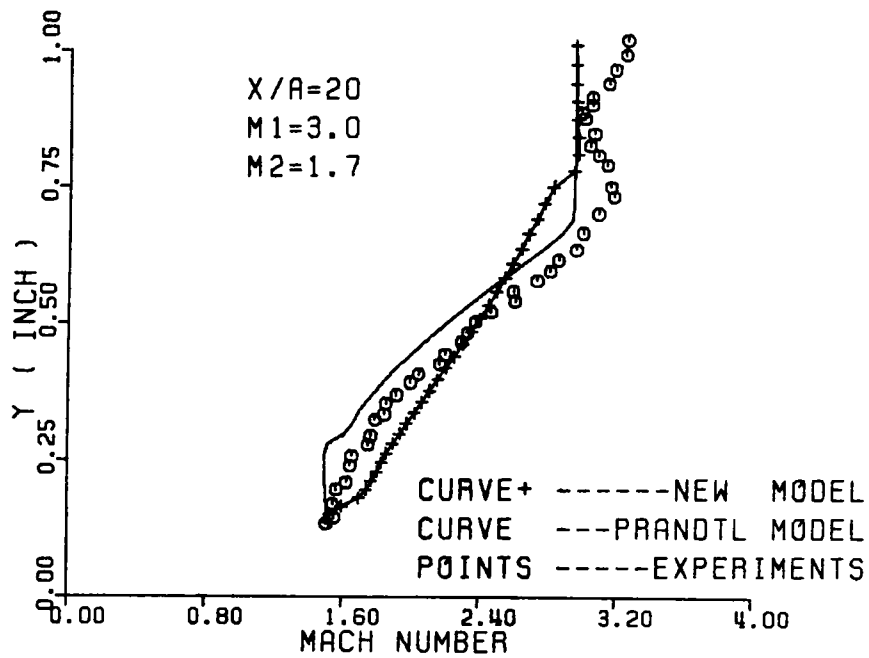

Figure 32. Mach number profile at x/a = 20.0, for $M_1 = 3.0$, $M_2 = 1.7$. (measured data from Ref. [10])

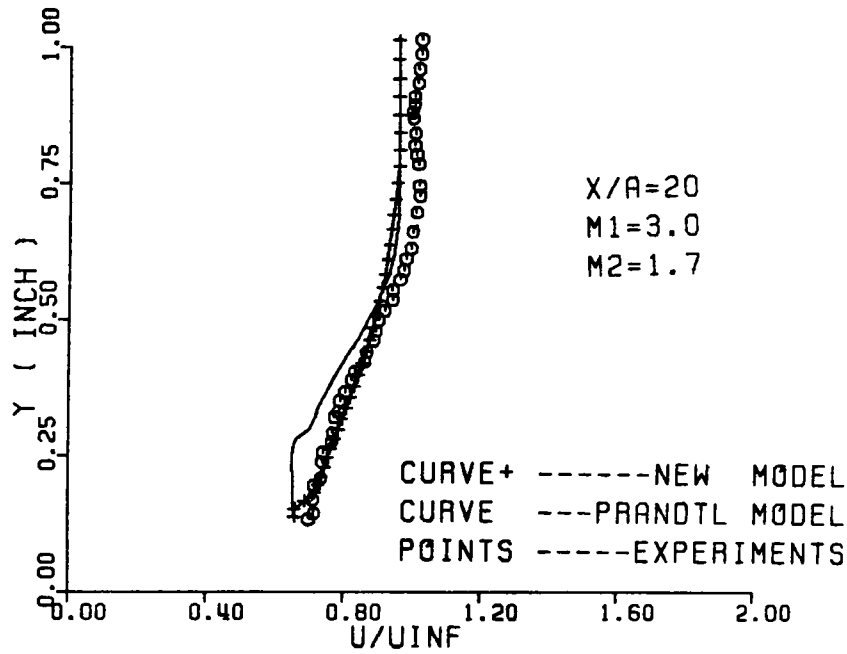

Figure 33. Velocity profile at x/a = 20.0, for the case of $M_1 = 3.0$, $M_2 = 1.7$ (measured data from Ref. [10])

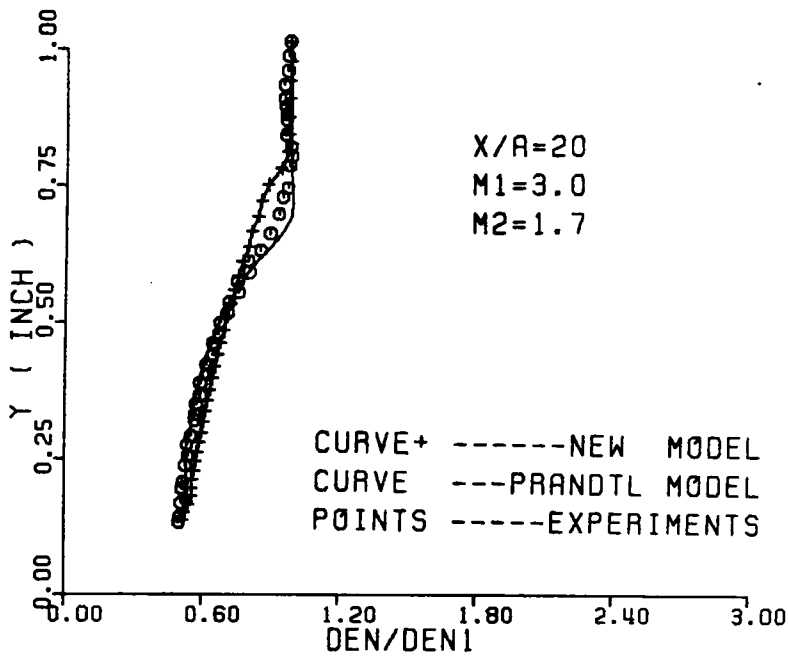

Figure 34. Density profile at x/a = 20.0, for the case of $M_1 = 3.0$, $M_2 = 1.7$ (measured data from Ref. [10])

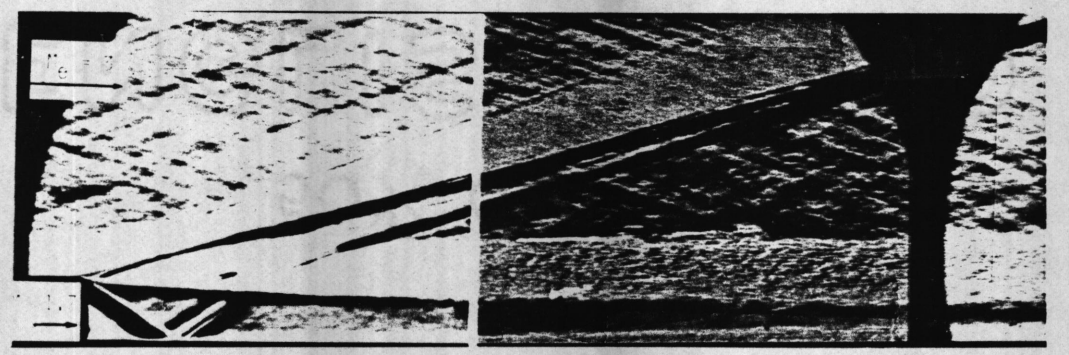

(a)

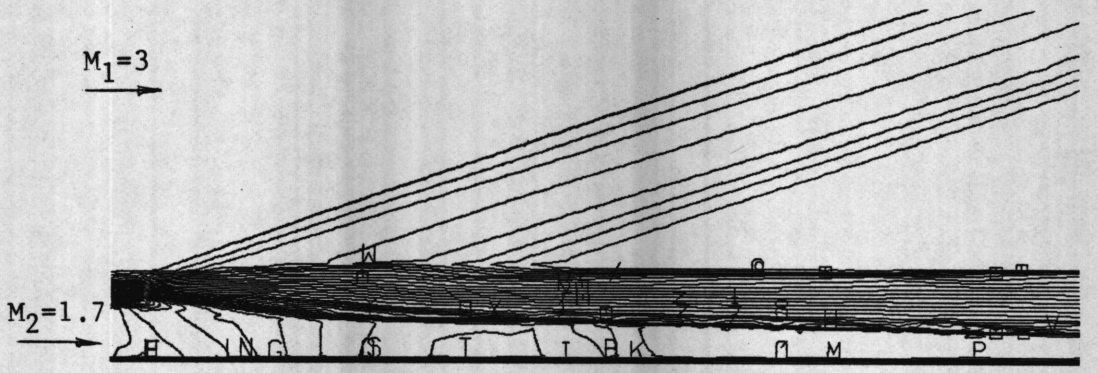

(b)

Figure 35. (a) Experimental Spark-Schlieren from Ref. [10] and (b) numerical density contour of the new model for $M_1 = 3.0$, $M_2 = 1.7$.

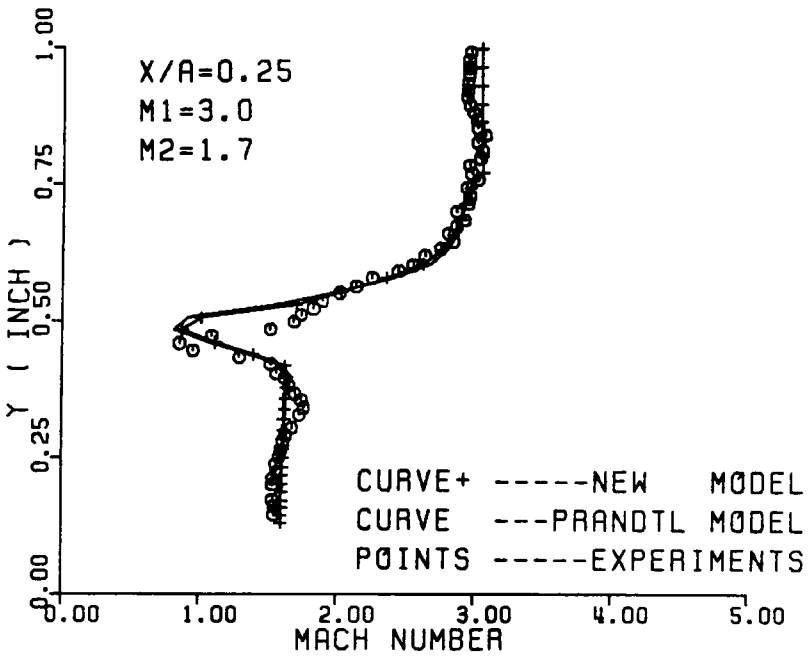

Figure 36. Mach number profile at x/a = 0.25 for heated injection flow. (measured data from Ref. [78])

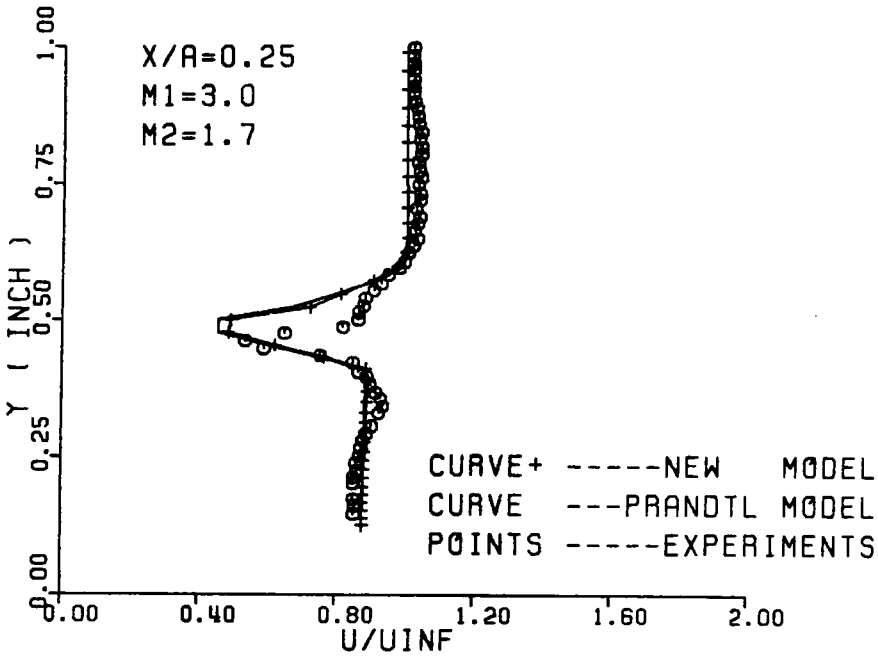

Figure 37. Velocity profile at x/a = 0.25 for heated injection flow. (measured data from Ref. [78])

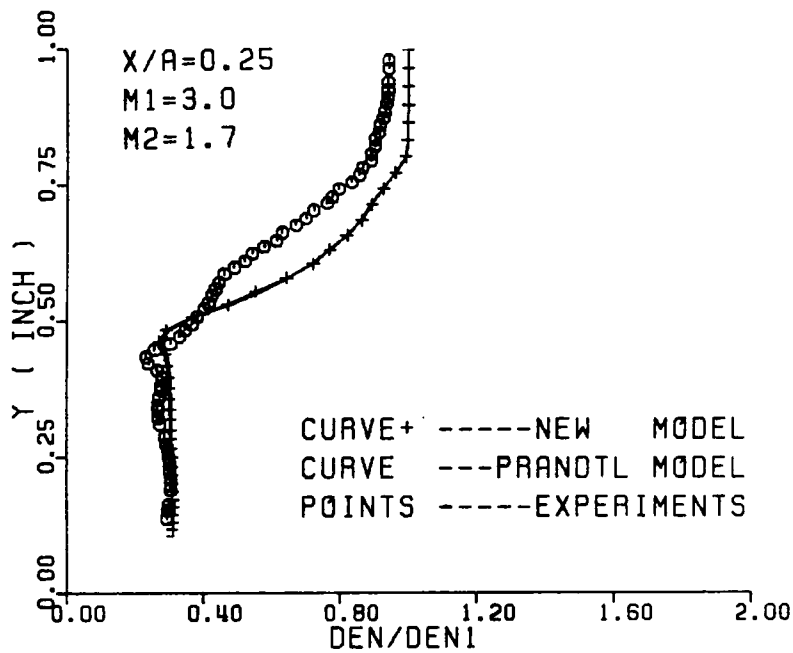

Figure 38. Density profile at x/a = 0.25 for heated injection flow. (measured data from Ref. [78])

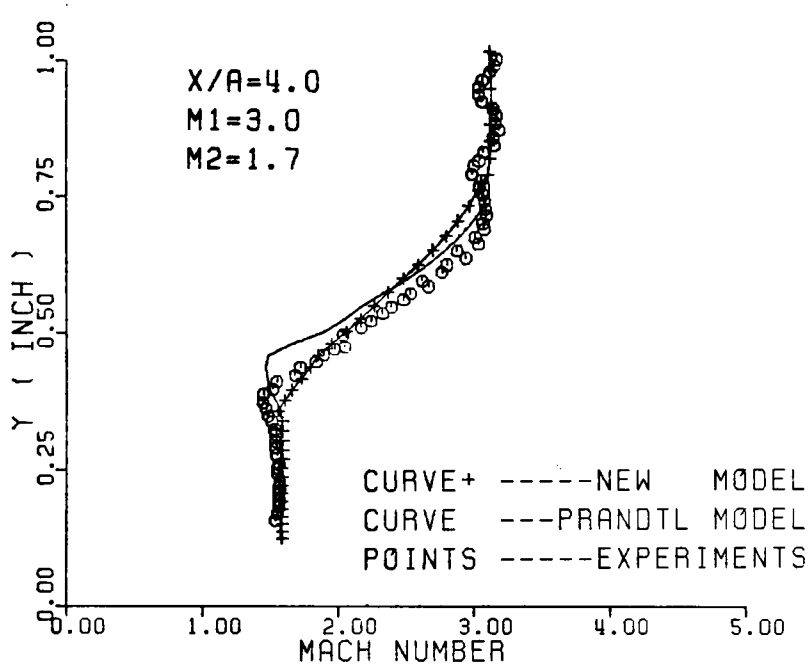

Figure 39. Mach number profile at x/a = 4.0 for heated injection flow. (measured data from Ref. [78])

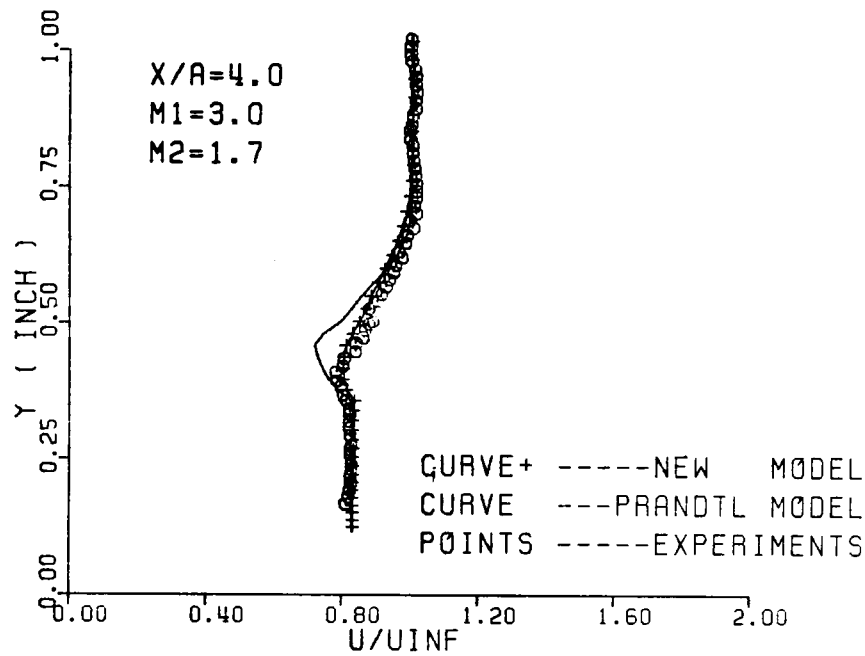

Figure 40. Velocity profile at x/a = 4.0 for heated injection flow. (measured data from Ref. [78])

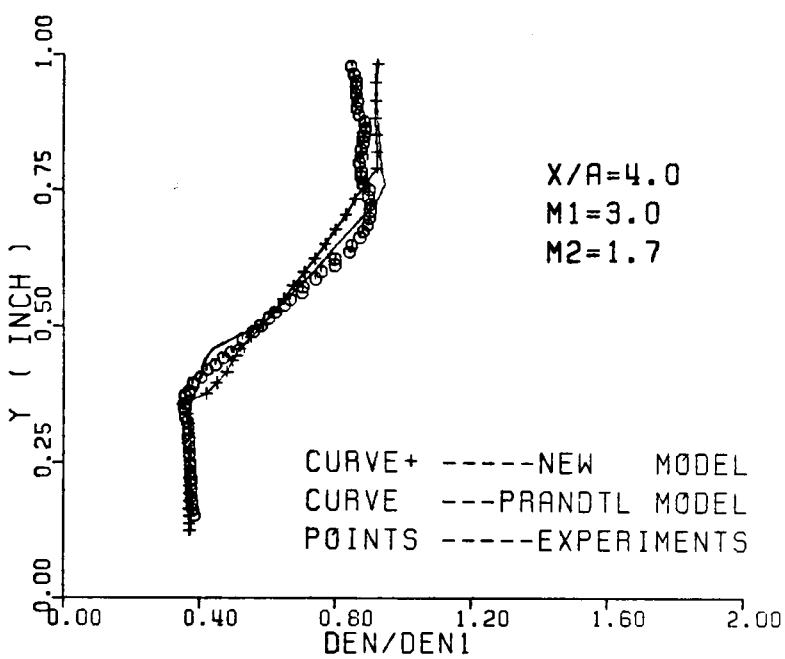

Figure 41. Density profile at x/a = 4.0 for heated injection flow. (measured data from Ref. [78])

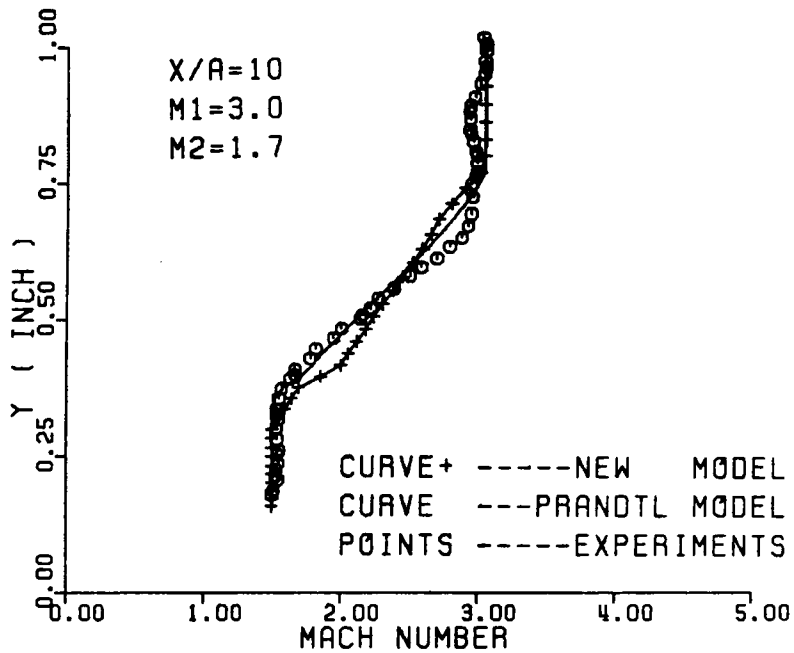

Figure 42. Mach number profile at x/a = 10 for heated injection flow. (measured data from Ref. [78])

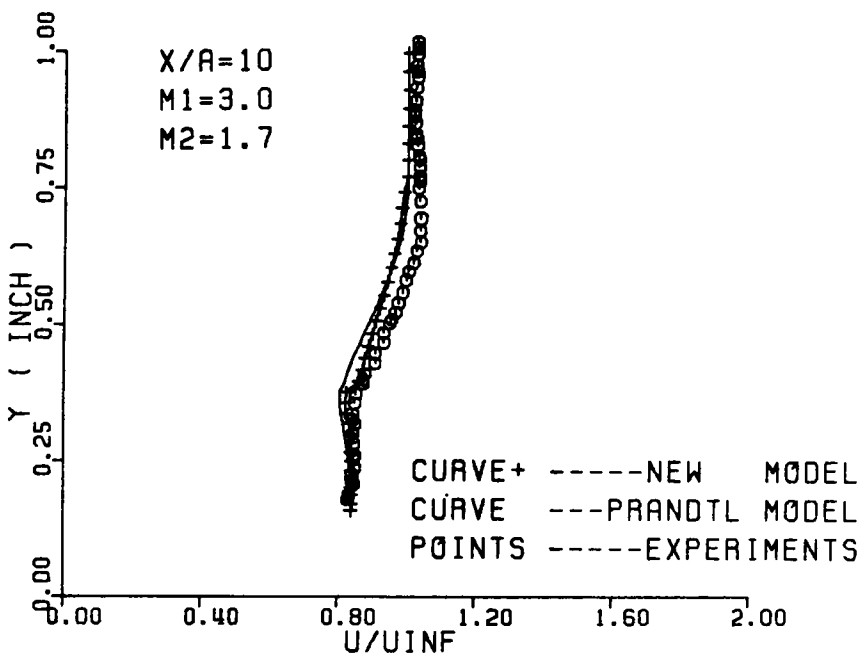

Figure 43. Velocity profile at x/a = 10 for heated injection flow. (measured data from Ref. [78])

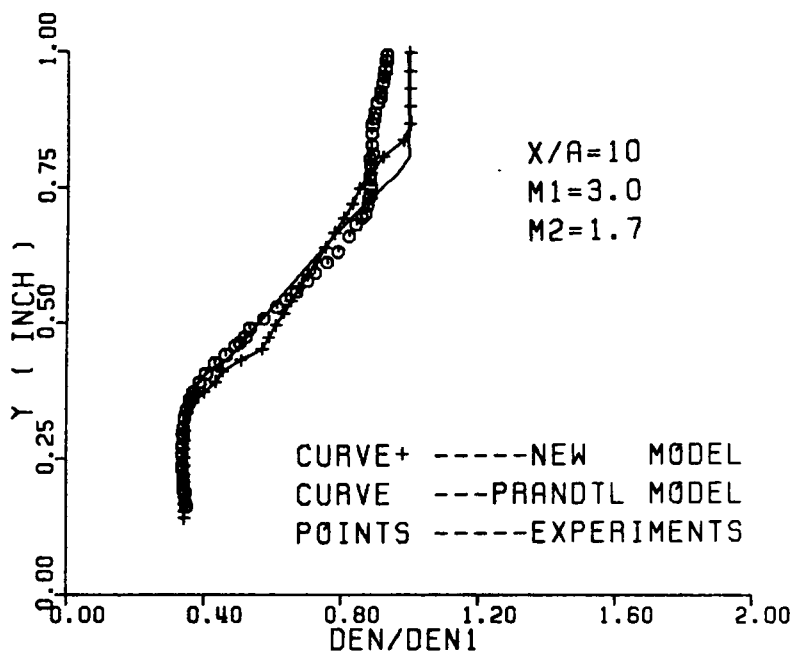

Figure 44. Density profile at x/a = 10 for heated injection flow. (measured data from Ref. [78])

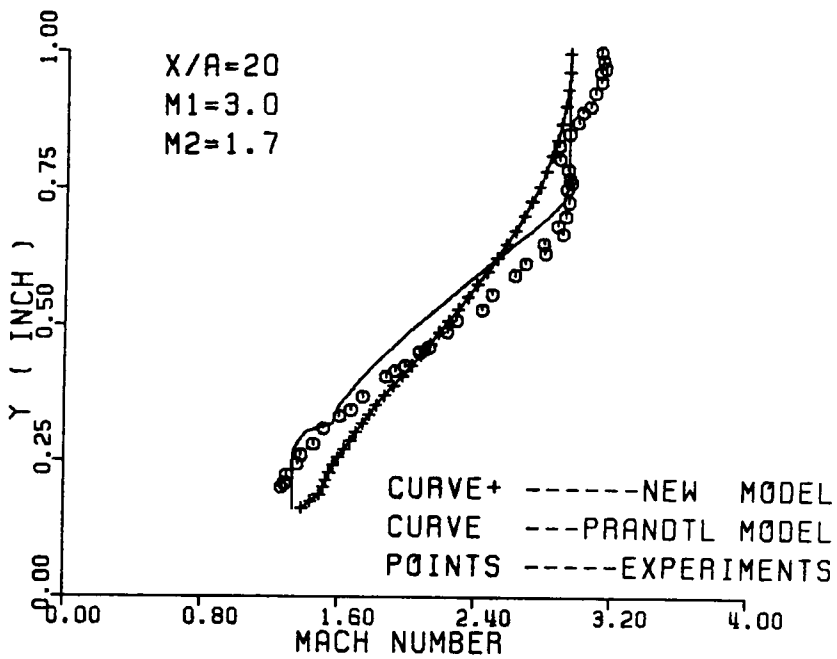

Figure 45. Mach number profile at x/a = 20 for heated injection flow. (measured data from Ref. [78])

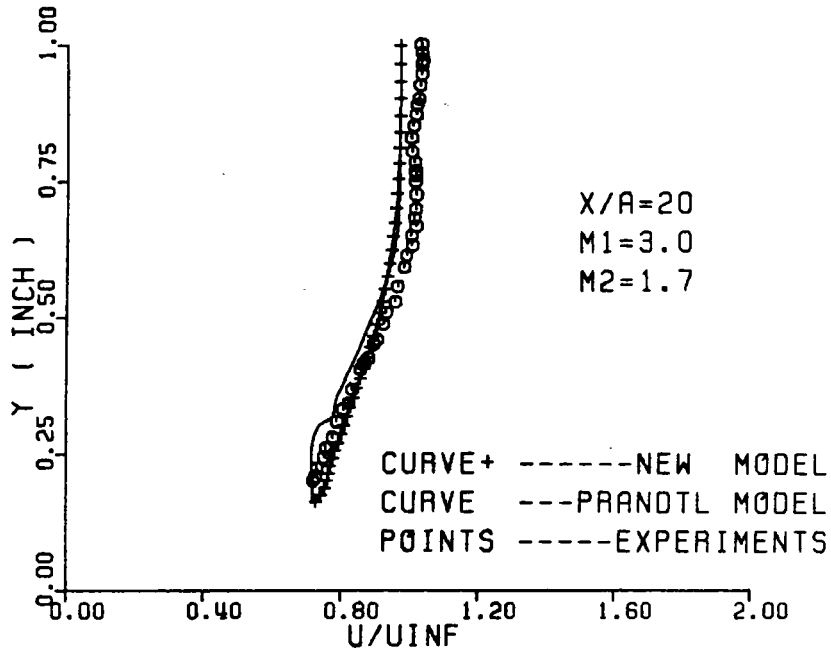

Figure 46. Velocity profile at x/a = 20 for heated injection flow. (measured data from Ref. [78])

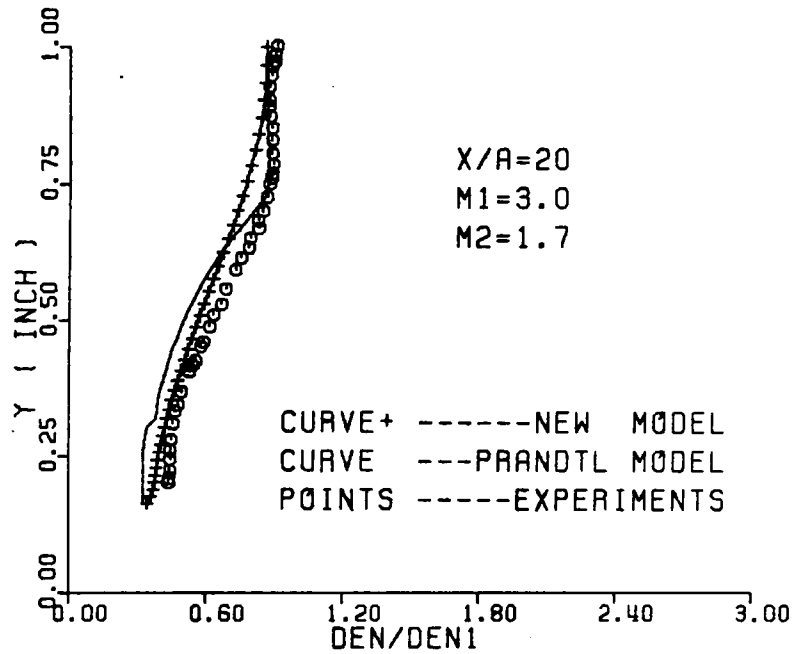

Figure 47. Density profile at x/a = 20 for heated injection flow. (measured data from Ref. [78])

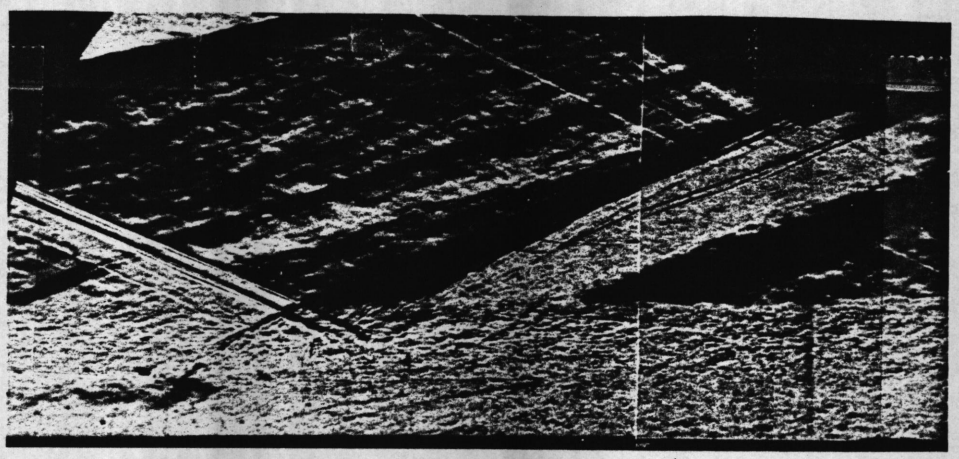

(a)

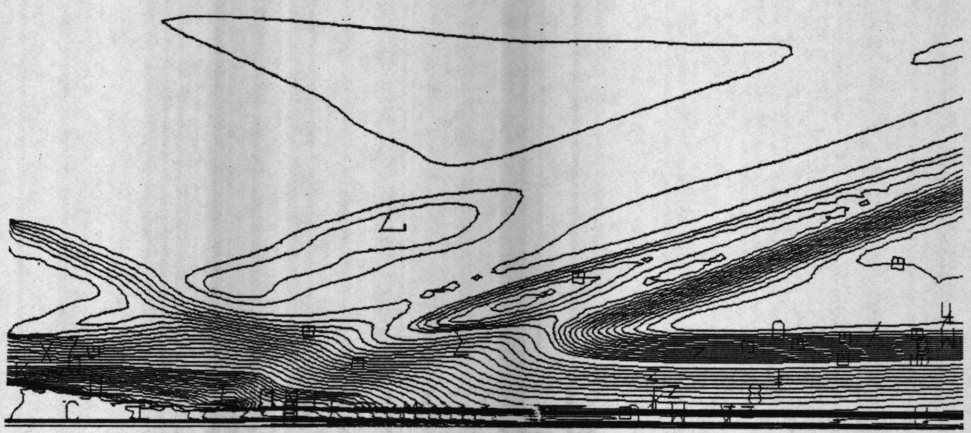

(b)

Figure 48. (a) Experimental Spark-Schlieren from Ref. [10] and (b) numerical density contour for shock-wave/turbulent shear layer and boundary layer interaction of the new model.

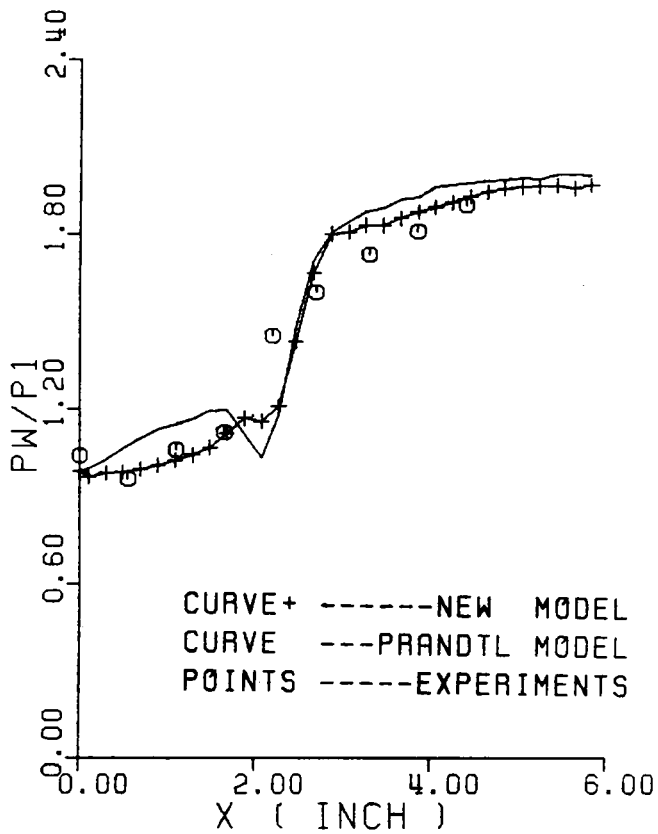

Figure 49. Wall presure distribution for shock-wave/turbulent shear layer and boundary layer interaction. (measured data from Ref. [10])

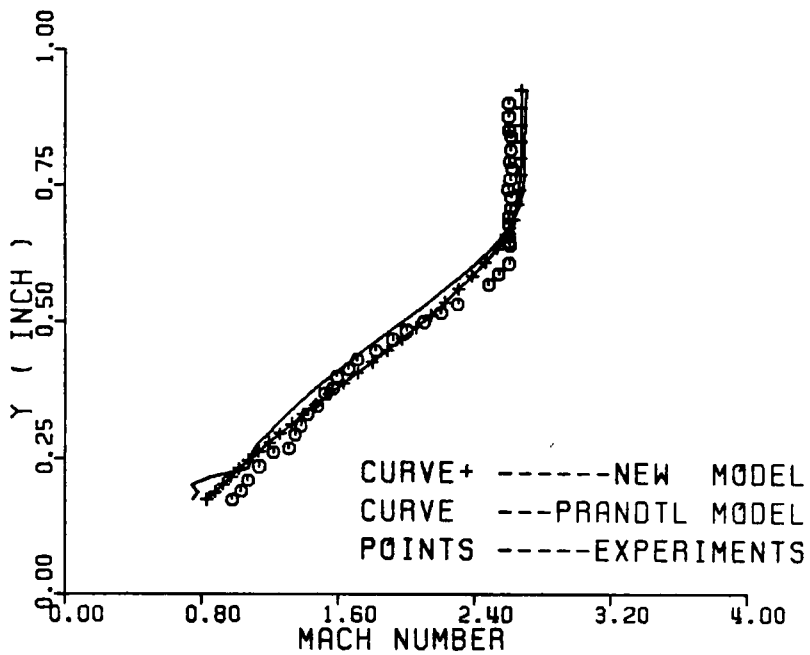

Figure 50. Mach number profile at x/a = 20 for shock-wave/turbulent shear layer and boundary layer interaction. (measured data from Ref. [10])

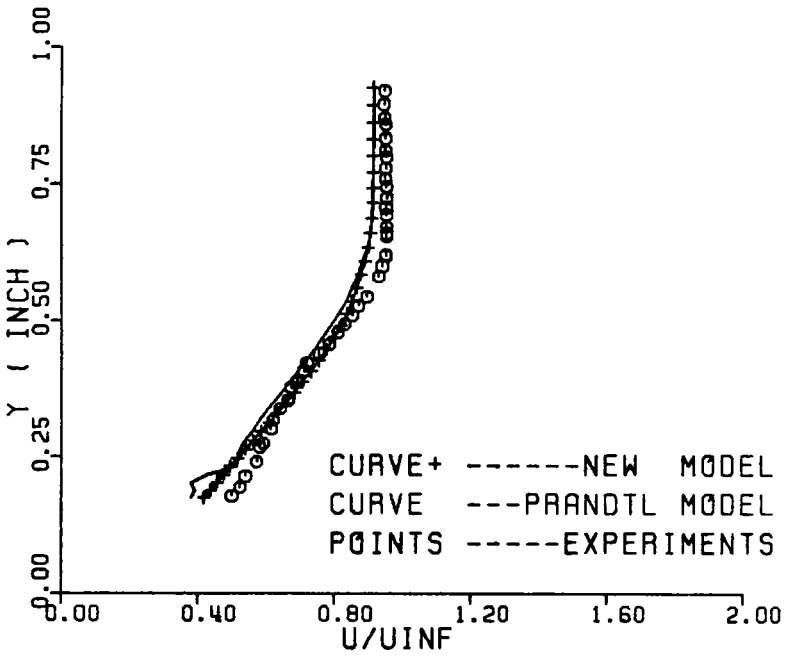

Figure 51. Velocity profile at x/a = 20 for shock-wave/turbulent shear layer and boundary layer interaction. (measured data from Ref.[10])

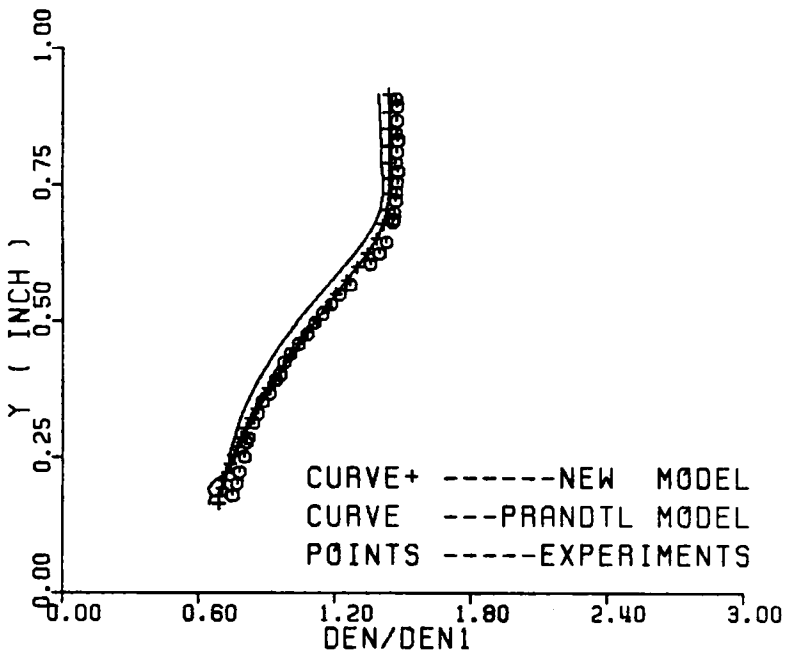

Figure 52. Density profile at x/a = 20 for shock-wave/turbulent shear layer and boundary layer interaction. (measured data from Ref.[10])

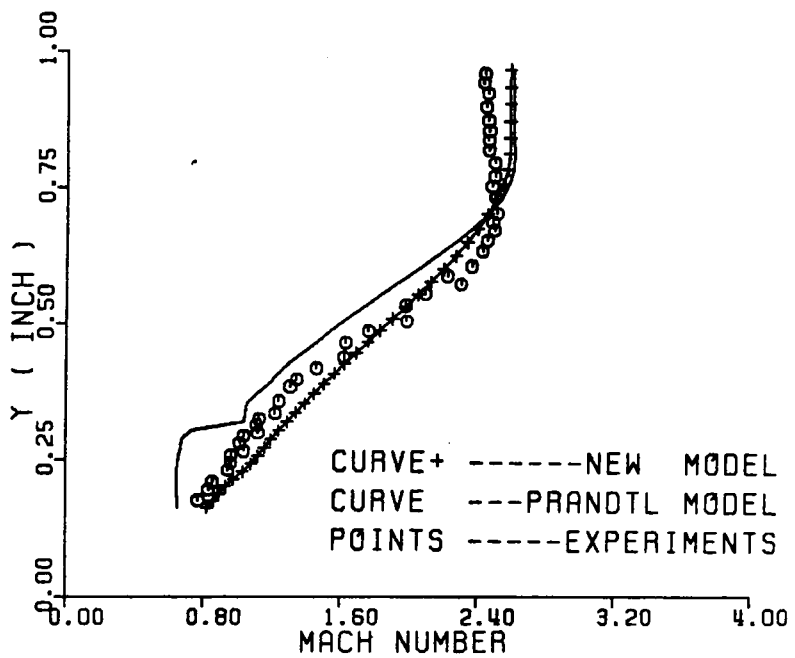

Figure 53. Mach number profile at x/a = 20 for shock-wave/heated turbulent shear layer and boundary layer interaction. (measured data from Ref. [78])

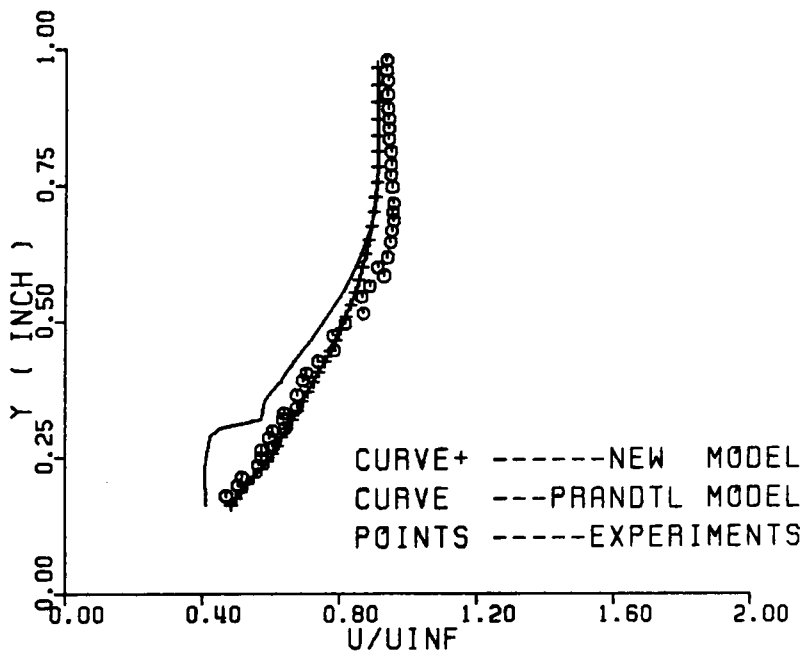

Figure 54. Velocity profile at x/a = 20 for shock-wave/heated turbulent shear layer and boundary layer interaction. (measured data from Ref. [78])

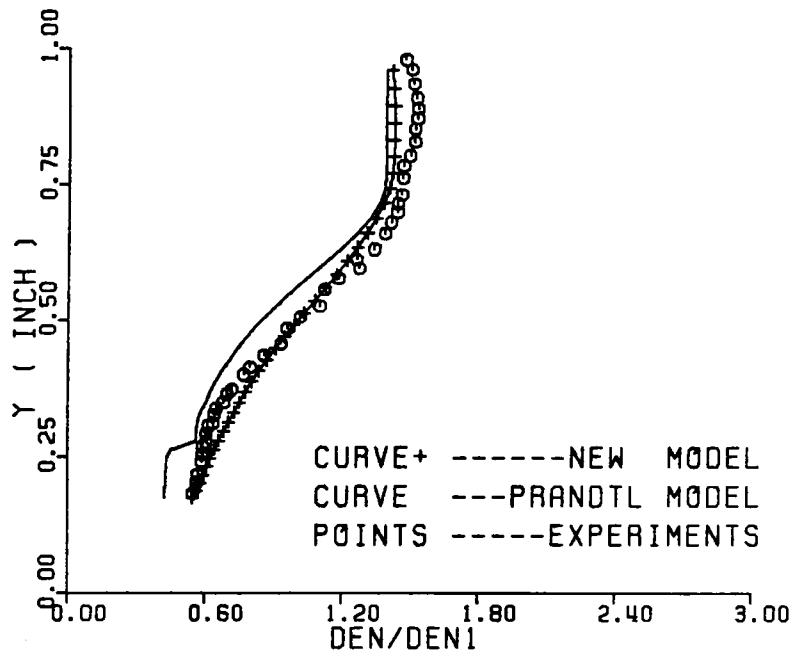

Figure 55. Density profile at x/a=20 for shock-wave/heated turbulent shear layer and boundary layer interaction. (measured data from Ref. [78])

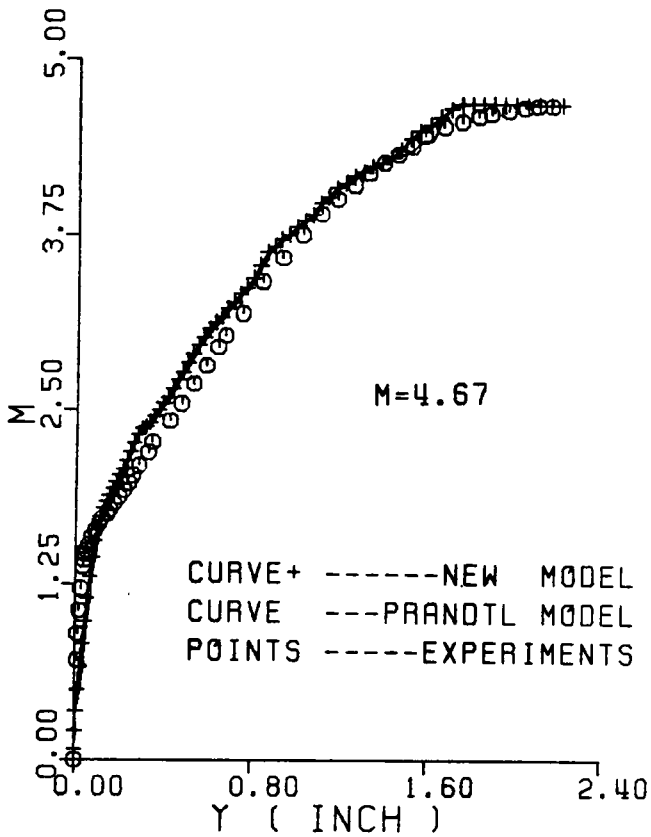

Figure 56. Mach number profile in the turbulent boundary layer flow over a flat plate at x = 69.25 inches from the throat, M = 4.67. (measured data from Ref. [79])

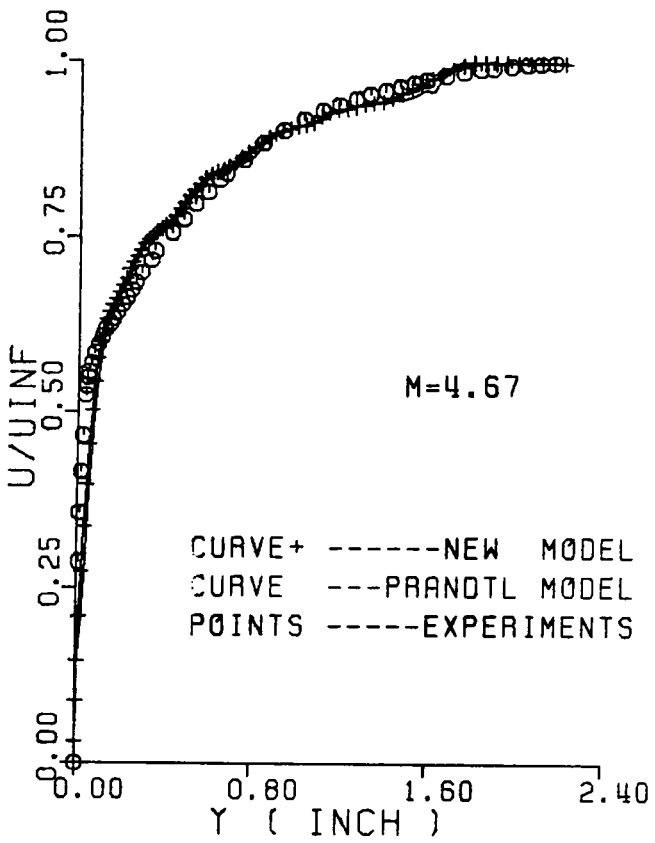

Figure 57. Velocity profile in the turbulent boundary layer flow over a flat plate at x = 69.25 inches from the throat, M = 4.67. (measured data from Ref. [79])

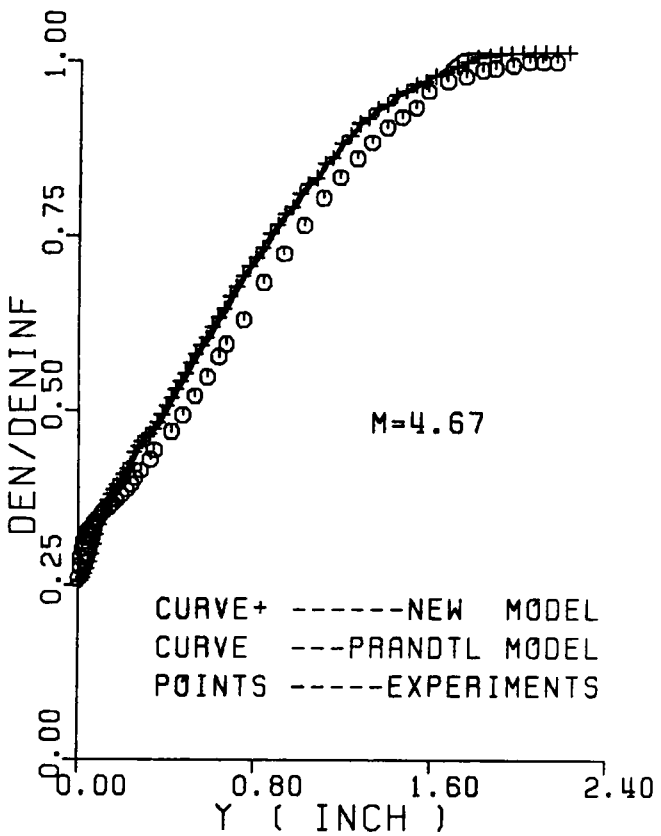

Figure 58. Density profile in the turbulent boundary layer flow over a flat plate at x = 69.25 inches from the throat, M = 4.67. (measured data from Ref. [79])

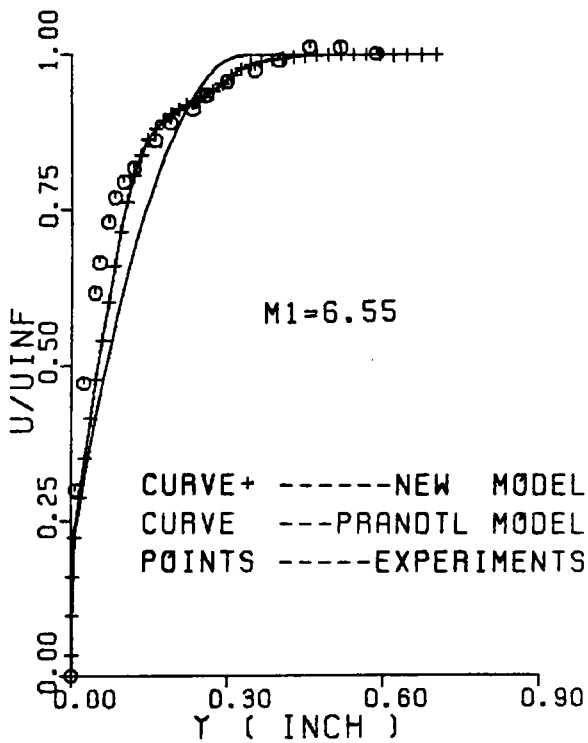

Figure 59. Velocity profile in the turbulent boundary layer flow over a flat plate at x=26 inches from the leading edge, $M_\infty = 6.55$. (measured data from Ref. [80,81])

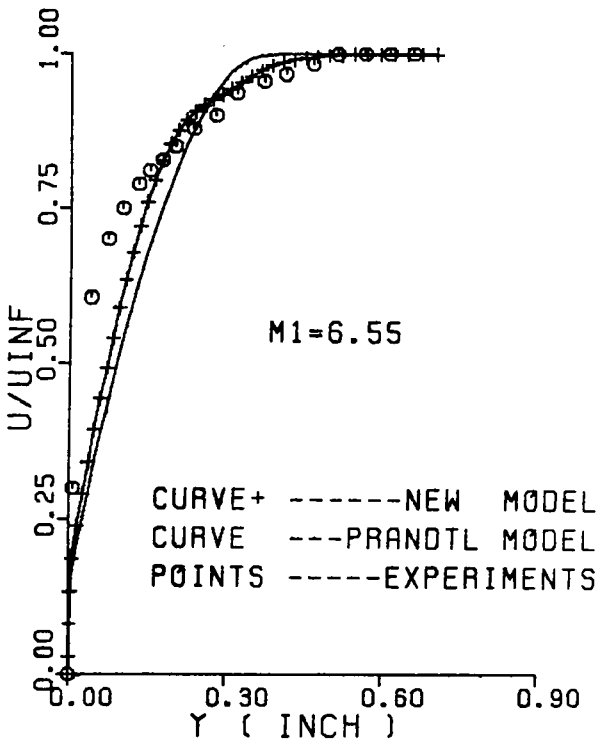

Figure 60. Velocity profile in the turbulent boundary layer flow over a flat plate at x=35 inches from the leading edge, $M_\infty = 6.55$. (measured data from Ref. [80,81])

The vita has been removed from the scanned document